EXPLORING THE SATURN SYSTEM IN THE THERMAL INFRARED: THE COMPOSITE INFRARED SPECTROMETER

F. M. FLASAR[1,*], V. G. KUNDE[2], M. M. ABBAS[3], R. K. ACHTERBERG[4], P. ADE[5], A. BARUCCI[6], B. BÉZARD[6], G. L. BJORAKER[1], J. C. BRASUNAS[1], S. CALCUTT[7], R. CARLSON[4], C. J. CÉSARSKY[8], B.J. CONRATH[9], A. CORADINI[10], R. COURTIN[6], A. COUSTENIS[6], S. EDBERG[11], S. EDGINGTON[11], C. FERRARI[12], T. FOUCHET[6], D. GAUTIER[6], P. J. GIERASCH[9], K. GROSSMAN[13], P. IRWIN[7], D. E. JENNINGS[1], E. LELLOUCH[6], A. A. MAMOUTKINE[4], A. MARTEN[6], J. P. MEYER[12], C. A. NIXON[2], G. S. ORTON[11], T. C. OWEN[14], J. C. PEARL[1], R. PRANGÉ[6], F. RAULIN[15], P. L. READ[7], P. N. ROMANI[1], R. E. SAMUELSON[2], M. E. SEGURA[16], M. R. SHOWALTER[17], A. A. SIMON-MILLER[1], M. D. SMITH[1], J. R. SPENCER[18], L. J. SPILKER[11] and F. W. TAYLOR[7]

[1]*Goddard Space Flight Center, Greenbelt, MD, 20771, U.S.A.*
[2]*University of Maryland, College Park, MD 20742, U.S.A.*
[3]*Marshall Space Flight Center, Huntsville, AL 35812, U.S.A.*
[4]*Science Systems and Applications Inc., Lanham, MD 20706, U.S.A.*
[5]*University of Cardiff, CF24 3YB, U.K.*
[6]*Observatoire de Paris-Meudon, F92195 Meudon Cedex, France*
[7]*Oxford University, OX1 3PU, U.K.*
[8]*European Southern Observatory, 85748 Garching bei Muenchen, Germany*
[9]*Cornell University, Ithaca, NY 14853, U.S.A.*
[10]*Istituto di Astrofisica Spaziale, Rome I-00133, Italy*
[11]*Jet Propulsion Laboratory, Pasadena, CA 91109, U.S.A.*
[12]*CEA/Service d'Astrophysique, 91191 Gif-sur-Yvette Cedex, France*
[13]*Gesamthochschule Wuppertal, 5600 Wuppertal 1, Germany*
[14]*University of Hawaii, Honolulu, HI 96822, U.S.A.*
[15]*Université de Paris 7 & 12, 94010 Creteil Cedex, France*
[16]*QSS Group, Inc, Lanham, MD 20706 U.S.A.*
[17]*Stanford University, Stanford, CA 94305 U.S.A.*
[18]*Southwest Research Institute, Boulder, CO 80302 U.S.A.*
([*]Author for correspondence: E-mail: f.m.flasar@nasa.gov)

(Received 9 October 2003; Accepted in final form 2 January 2004)

Abstract. The Composite Infrared Spectrometer (CIRS) is a remote-sensing Fourier Transform Spectrometer (FTS) on the Cassini orbiter that measures thermal radiation over two decades in wavenumber, from 10 to 1400 cm^{-1} (1 mm to 7μm), with a spectral resolution that can be set from 0.5 to 15.5 cm^{-1}. The far infrared portion of the spectrum (10–600 cm^{-1}) is measured with a polarizing interferometer having thermopile detectors with a common 4-mrad field of view (FOV). The middle infrared portion is measured with a traditional Michelson interferometer having two focal planes (600–1100 cm^{-1}, 1100–1400 cm^{-1}). Each focal plane is composed of a 1×10 array of HgCdTe detectors, each detector having a 0.3-mrad FOV. CIRS observations will provide three-dimensional maps of temperature, gas composition, and aerosols/condensates of the atmospheres of Titan and Saturn with good vertical and horizontal resolution, from deep in their tropospheres to high in their mesospheres. CIRS's ability to observe atmospheres in the limb-viewing mode (in addition to nadir) offers the opportunity to

Space Science Reviews **115:** 169–297, 2004.

provide accurate and highly resolved vertical profiles of these atmospheric variables. The ability to observe with high-spectral resolution should facilitate the identification of new constituents. CIRS will also map the thermal and compositional properties of the surfaces of Saturn's icy satellites. It will similarly map Saturn's rings, characterizing their dynamical and spatial structure and constraining theories of their formation and evolution. The combination of broad spectral range, programmable spectral resolution, the small detector fields of view, and an orbiting spacecraft platform will allow CIRS to observe the Saturnian system in the thermal infrared at a level of detail not previously achieved.

Keywords: Infrared spectroscopy, Saturn, Titan, Saturn's rings, Saturn's moons, atmospheric temperatures, atmospheric composition, atmospheric dynamics, Cassini

1. Introduction

The Saturn system offers a rich variety of objects for exploration and study at infrared wavelengths. The atmospheres of Saturn and Titan, the surfaces of Titan and the icy satellites, and the rings, each pose unique challenges for a single instrument. In the wake of the highly successful Galileo mission to Jupiter, an important goal is to acquire a set of data at Saturn that will allow detailed comparisons between these two giants, providing insights that will sharpen our general ideas about the formation of planetary systems.

What are the key differences between the atmospheres of Jupiter and Saturn, and what accounts for them? Why does Titan, unlike all other planetary satellites, have such a thick atmosphere? How is the chemistry that occurs on it today related to prebiological chemical evolution on the early Earth? What governs the weather on this slowly rotating satellite, and how does it compare to that driving the circulations of Earth's and Venus' atmospheres? What relations exist among the various icy satellites and the rings and why is this satellite system so very different from Jupiter's? These are a few of the questions we hope to answer.

The Saturn system is well suited for exploration in the infrared. Saturn, its rings, and its satellites radiate most of their energy at mid- and far-infrared wavelengths, because their radiating temperatures are relatively cold: in the range 55–200 K. Most molecules have lines or bands of lines in this spectral region, arising from rotational or vibrational-rotational transitions. A spectrometer covering these wavelengths serves as a remote-sensing thermometer and assayer, allowing one to map temperatures and composition spatially and temporally. How well it can exploit this spectral region depends on its configuration and sensitivity, but key figures of merit include: high spectral resolution, to permit identification of trace constituents, including isotopic variants; broad spectral coverage, to encompass a large variation in the opacity of the target, whether it be an atmosphere, surface, or ring material; detectors having a small field of view (FOV) projected onto the sky; and close proximity to the target, as afforded by an orbiting spacecraft to provide a variety of geometric observing opportunities, including a broad range of phase-angle coverage.

The Composite Infrared Spectrometer (CIRS) is an infrared Fourier Transform Spectrometer (FTS) on the Cassini orbiter which measures thermal radiation over more than two decades in wavenumber (ν) from 10 to 1400 cm^{-1} (1 mm to 7 μm). CIRS will measure thermal emission from the Saturn system with a spectral resolution that can be selected over the range from 0.5 to 15.5 cm^{-1}. It will map the atmospheres of Saturn and its largest moon Titan temporally and spatially in three dimensions, including limb sounding, which will achieve a vertical resolution of one scale height or better. In addition, CIRS will map the thermal characteristics and composition of the other icy satellites and Saturn's rings.

The plan of this paper is as follows: Section 2 provides a brief overview of the instrument capabilities and its modes of operation. Section 3 discusses the science objectives of the CIR'S investigation, in context of the current knowledge of Saturn, Titan, the other satellites, and the rings. We discuss how CIRS's unique capabilities can help address many of the important questions concerning these bodies. Section 4 describes in more detail the observations CIRS will make during the Saturn tour. The instrument itself is described in Section 5. Appendices describe the retrieval of atmospheric variables from infrared spectra, the spatial response across the far-infrared FOV of CIRS, and the equations used in calibrating the infrared spectra.

CIRS acquired data during the Jupiter swingby from October, 2000, to March, 2001, which resulted in approximately 600,000 calibrated spectra. Jupiter results are not discussed here, except in the context of Saturn system science. Instead, we refer the reader to the Jupiter results reported elsewhere by Flasar *et al.* (2004), Kunde *et al.* (2004), Wong *et al.* (2004), Abbas *et al.* (2004), Fouchet *et al.* (2004a,b) and Irwin *et al.* (2004).

2. Instrument Overview

The CIRS instrument consists of two interferometers, sharing a common telescope and scan mechanism. They operate in the far-infrared (10–600 cm^{-1}) and mid-infrared (600–1400 cm^{-1}) with a commandable apodized[1] spectral resolution as high as 0.5 cm^{-1}. Table I summarizes the instrument properties. The far-IR interferometer is a polarization interferometer, with a focal plane consisting of two thermopile detectors with a 3.9-mrad FOV, labeled FP1. The mid-IR interferometer is a conventional Michelson interferometer with two focal plane arrays (FP3, FP4), each having 10 HgCdTe detectors, with 0.273-mrad FOV per pixel.

[1]Interferograms extend only over a finite distance, with maximum mirror displacement $\delta_{\max}$. The reconstructed spectrum, obtained via Fourier transforms, will consist of the true spectrum convolved with $\sin(2\pi\nu\delta_{\max})/2\pi\nu\delta_{\max}$, which produces a "ringing" in the vicinity of strong narrow features. To avoid this, the interferogram is "tapered" by multiplying it by a quasi-triangular apodization function, so that displacement amplitudes are attenuated away from the $\delta = 0$ central fringe. See, e.g., Hanel *et al.* (2003) for more discussion. A well-chosen apodization reduces the ringing considerably, but degrades the spectral resolution. In searching for weak features away from strong lines, it is often desirable to use unapodized spectra to maximize the contrast of the weak features. The search for HD rotational lines (see Section 3.1.1 and Figure 6) is one example of this.

TABLE I
CIRS instrument characteristics.

Telescope diameter (cm)	50.8		
Interferometers	Far-IR	Mid-IR	
Type	Polarizing	Michelson	
Spectral range (cm^{-1})	10—600	600–1400	
Spectral range (μm)	17—1000	7–17	
Spectral resolution (cm^{-1})	0.5–15.5	0.5–15.5	
Integration time (s)	2–50	2–50	
Focal planes	FP1	FP3	FP4
Spectral range (cm^{-1})	10—600	600–1100	1100–1400
Detectors	Thermopile	PC HgCdTe	PV HgCdTe
Pixels	2[a]	1×10	1×10
Pixel FOV (mrad)	3.9	0.273	0.273
Peak D* (cm $Hz^{1/2}$ W^{-1})	4×10^9	2×10^{10}	5×10^{11}
Data telemetry rate (kbs)		2 and 4	
Instrument temperature (K)		170	
Focal planes 3 and 4 Temperature (K)		75—90	

[a]Single FOV, two polarizations.

Figure 1 depicts the CIRS FOVs as projected onto the sky. The instrument is described in more detail in Section 5.

CIRS derives much of its heritage from the Voyager Infrared Interferometer Spectrometer (IRIS: see Hanel *et al.*, 1980), but it has several important improvements:

(I) *Extended far-infrared coverage*: The CIRS coverage between 10 and 180 cm^{-1} was not accessible to IRIS. This will extend the vertical range of temperature sounding to include the upper troposphere of Titan and lower stratospheres of Saturn and Titan. It will also increase the chances of detecting previously undiscovered organic molecules. The enhanced spectral coverage will provide the ability to probe Saturn's ring particles in the poorly studied submillimeter region, where opacity decreases rapidly with increasing wavelength, and it will permit the thermal sounding of the first centimeter of the regoliths of the icy satellites.

(II) *Higher spectral resolution:* The maximum CIRS resolution of 0.5 cm^{-1} (apodized) is an order of magnitude higher than that of IRIS (4.3 cm^{-1}). This will increase the opportunity to detect new trace constituents including their isotopic variants, and will permit the improved retrieval of temperature and gas profiles by virtue of both the narrower contribution functions and of the higher altitudes probed.

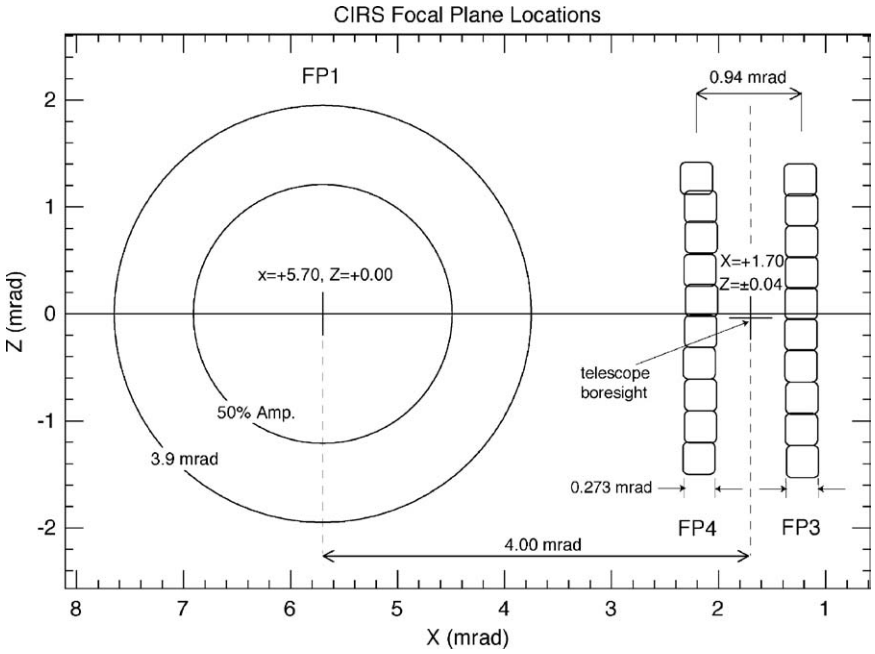

Figure 1. CIRS fields of view projected on the sky. FP1 is the far-IR focal plane. FP3 and FP4 are the mid-IR focal planes. The relative positions of the CIRS focal planes on the spacecraft have been determined by scans across a distant Jupiter and infrared stars (Section 5.2.2). The spacecraft –Y axis is at (X, Z) = (0, 0). The boresight of the Cassini imaging science (ISS) Narrow Angle Camera (NAC) is approximately at X = 0.58 mrad, Z = −0.17 mrad. The mid-IR arrays are linear. The slight "wobble" is just the best fit to the scan data for each pixel. The full length of each array is 2.876 mrad.

(III) *Improved sensitivity:* The CIRS sensitivity is much better than Voyager IRIS in the 600–1400 cm^{-1} region, through the use of passively cooled HgCdTe detectors, instead of a thermopile. This allows the smaller 0.27 × 0.27 mrad FOV's to be used, giving higher spatial resolution.

(IV) *Limb-viewing capability:* The arrays and smaller detectors in the 600–1400 cm^{-1} region permit limb sounding of both Saturn's and Titan's stratosphere and mesosphere with an altitude resolution better than one scale height, an improvement of 2–3 over the Voyager IRIS nadir soundings. In addition, the long absorber paths viewed against a cold space background greatly enhance sensitivity to minor constituents. Close passages of Titan will repeatedly allow limb sounding of that body at far infrared wavelengths with the larger 3.9-mrad FP1 FOV.

(V) *Orbiting platform:* The Cassini spacecraft has an inherent advantage, in that it will orbit within the Saturn system for several years, while each of the Voyager spacecraft flew through only once. Hence CIRS will have the opportunity for global and seasonal mapping with spatial detail that was

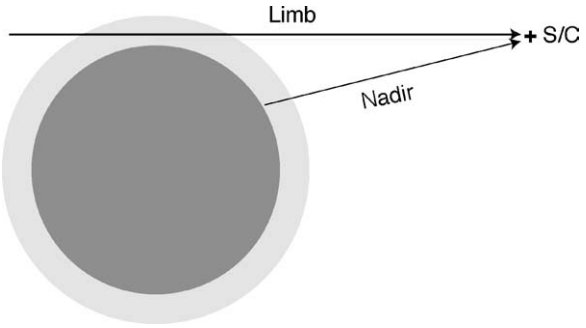

Figure 2. Schematic illustrating limb and nadir modes of observation.

simply not possible with IRIS. In addition, CIRS will be able to make refined investigations of newly discovered phenomena.

Figure 2 illustrates the nadir and limb-viewing modes CIRS will employ. The viewing mode and spectral resolution are dictated by the scientific objectives. The principal modes of observation of Saturn and Titan are:

(1) *Nadir viewing, complete spectral range, full spectral resolution (0.5 cm^{-1}).* Objectives: gas composition, isotopic ratios, general exploration.
(2) *Nadir viewing, complete spectral range, reduced spectral resolution (3, 15.5 cm^{-1}).* Objectives: maps of temperature, more abundant gas species, and aerosols.
(3) *Limb viewing, complete spectral range, full spectral resolution (0.5 cm^{-1}).* Objectives: Vertical profiles of trace constituents, identifications of new species, distinguishing vapor from condensed phases.
(4) *Limb viewing, complete spectral range, reduced spectral resolution (3, 15.5 cm^{-1}).* Objectives: Vertical profiles of temperature, aerosols, and more abundant gases to high altitudes (0.01 mbar).

For the satellites and rings, the primary observational modes are:

(5) *Nadir viewing, complete spectral range, reduced spectral resolution (3.0 cm^{-1}), stare.* Objectives: composition.
(6) *Nadir viewing, FP1, low spectral resolution (15.5 cm^{-1}), full disk, stare.* Objectives: disk temperatures for phase ("diurnal") coverage; eclipse measurements to determine thermal inertia.
(7) *Mapping of icy satellites at low spectral resolution (15.5 cm^{-1}).* Objectives: composition; thermal probing of regolith to search for solid state greenhouse effects (FP1); thermal anomalies; high spatial resolution surface-temperature mapping and eclipse heating and cooling to determine the thermal inertia (FP3, FP4).

(8) *Ring radial scans, complete spectral range, reduced spectral resolution* (*3 cm^{-1} and 15.5 cm^{-1}*). Objectives: Radial profiles of composition, temperature and opacity.
(9) *Ring circumferential scans, complete spectral range, reduced spectral resolution* (*15.5 cm^{-1}*). Objectives: Eclipse heating and cooling curves to obtain ring particle thermal inertia and rotation rate.
(10) *Long integrations on rings, full and reduced spectral resolution* (*0.5 cm^{-1} and 3.0 cm^{-1}*). Objectives: composition of non-icy component of ring material, IR phase function, interior structure.

3. Scientific Background and Objectives

3.1. SATURN

Saturn is like the Sun, in that it is composed primarily of hydrogen and helium. However, its mass – like Jupiter's – is too small for its gravitational field to produce the high pressures and temperatures required for nuclear burning in its interior. Instead, it radiates thermal energy from its degenerate fluid interior, which was created during an earlier Kelvin contraction phase, and by gravitational separation of partially immiscible helium-rich and hydrogen-rich phases (see, e.g., Hubbard, 1980). Not long ago, the common perception was that the giant planets were formed directly from the gaseous material of the primitive solar nebula. The planets were massive enough to prevent the escape of any element, and hence the atmospheres should reflect solar composition. After hydrogen and helium, compounds of carbon, nitrogen, and oxygen should be the most abundant. Although, in a general sense, this model is correct, it does not hold up at the detailed level, reflecting a more complex scenario of planetary formation and evolution than originally envisioned (see, e.g., Gautier and Owen, 1989, for a review). The atmosphere of Saturn may be depleted in helium, because of the immiscibility and differentiation mentioned above that is occurring in its interior during the current epoch (see, e.g., Fortney and Hubbard, 2003). The relative abundances of carbon and nitrogen are above solar values by factors of two to four, suggesting that Saturn formed heterogeneously from the surrounding nebula (see, e.g., Pollack *et al.*, 1996). In the final phase of formation the hydrogen and planetesimals contained in the feeding zone of the planet (within the Hill radius) collapsed simultaneously, so that the resulting gaseous envelope was enriched in heavy elements (Magni and Coradini, 2003). Sulfur may also be enriched on Saturn by a factor of $\sim 10\times$ solar (Briggs and Sacket, 1989), if the apparent depletion of NH_3 in the upper troposphere is caused by the formation of dense NH_4SH clouds. These enrichments in heavy elements constrain the theories of the formation of Saturn, as well as the composition of grains embedded in the solar nebula.

Figure 3 depicts synthetic spectra of Saturn at low latitudes over the full CIRS spectral range at several resolutions; major spectral features are indicated. Observed

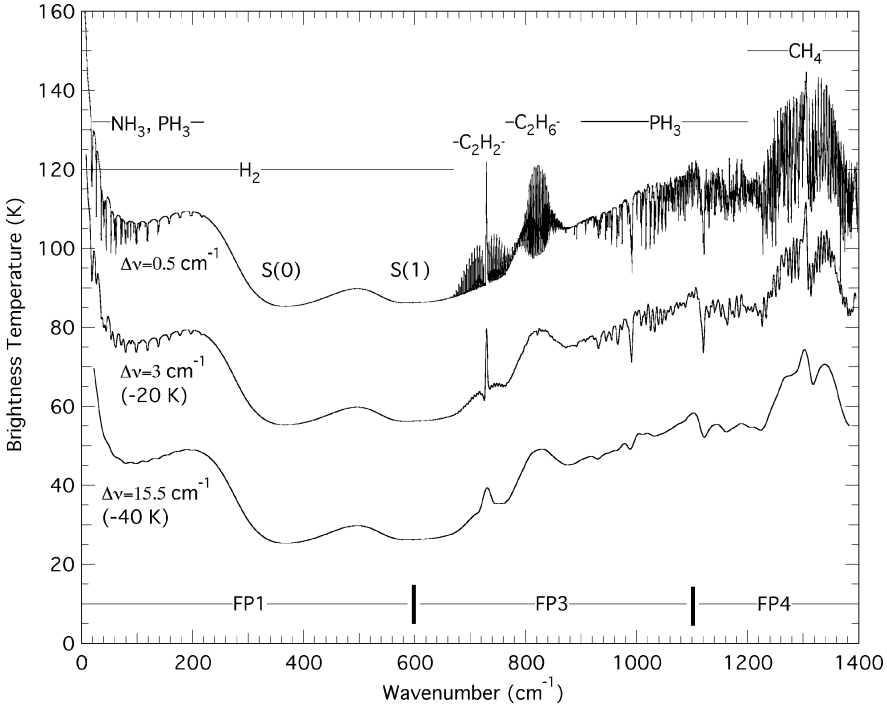

Figure 3. Synthetic spectrum of Saturn's equatorial atmosphere at three (apodized) resolutions. For ease of viewing the entire CIRS spectral range, brightness temperatures are depicted. The brightness temperatures of the lower-resolution spectra are offset vertically as indicated. The boundaries of the three focal planes (FP1, FP3, FP4) are shown at the bottom. At wavenumbers less than 670 cm^{-1} the spectrum is dominated by tropospheric absorption. The broad spectral features are from pressure-induced absorption from the S(0) and S(1) lines of H_2, labeled in the figure, and from the translational continuum of H_2 at lower wavenumbers. Superposed on this at wavenumbers less than 220 cm^{-1} is absorption primarily from NH_3 and PH_3. PH_3 also appears in absorption between 900 and 1200 cm^{-1}. Spectral features attributable to C_2H_2, C_2H_6, and CH_4 appear in emission, relative to the background continuum, because their line-formation regions are in the stratosphere. The spectral regions associated with pressure-induced H_2 absorption and CH_4 emission serve as the thermometers used to retrieve vertical profiles of atmospheric temperature.

spectra such as these will form the basis for addressing several of the scientific issues just raised.

Table II summarizes the scientific objectives of the CIRS investigation of Saturn. The first column lists major scientific objectives for Saturn, and the second column lists the physical variables that CIRS can retrieve to address those objectives. The last column lists the relevant measurement sequences, which are treated more fully in Section 4.2.

3.1.1. *Formation, Evolution, and Internal Structure*

CIRS spectra will contribute to this area in several ways. The first is through a better determination of the abundances of He, C, N, and S in Saturn's atmosphere.

TABLE II

Saturn science and measurement objectives and observations.

Science objective	CIRS categories: Retrieved physical parameters	Observations
Formation, evolution, and internal structure		
Elemental abundances	He	Nadir occultation point, far-IR maps
	CH_4, NH_3, H_2S	Comp integrations, far- and mid-IR nadir maps, regional nadir maps, limb integrations, limb maps
Isotopic abundances	HD, CH_3D, $^{15}NH_3$, $^{13}CH_4$	” ”
Internal heat	Temperatures	Far- and mid-IR nadir maps, regional nadir maps, feature tracks
Atmospheric gas composition		
Disequilibrium species	PH_3, HCP, halides, stratospheric hydrocarbons, new molecules	Comp integrations, limb integrations, limb maps, feature tracks
	Ortho/para ratio	Far-IR nadir maps, regional nadir maps
Condensible gases	NH_3, H_2S	Comp integrations, far-IR and mid-IR nadir maps, feature tracks
External sources (e.g., rings)	Oxygen species: stratospheric H_2O, CO_2, CO	Comp integrations, far-IR nadir maps, regional nadir maps
Clouds/aerosols		
Composition	NH_3, NH_4SH,...	Far- and mid-IR nadir maps, regional nadir maps, limb maps
Microphysical properties	Aerosol/cloud properties	” ”
Auroral hot spots		
Spatial and temporal distribution	Temperature and composition gradients	Feature tracks, limb maps, limb integrations, far- and mid-IR nadir maps, regional nadir maps, comp integrations
Spectral properties	New species	Feature tracks, limb integrations, comp integrations
Atmospheric structure		
Temperature, pressure, density	Temperature field	Far- and mid-IR nadir maps, regional nadir maps, limb maps
Circulation		
Zonal jets	Thermal winds	Far- and mid-IR nadir maps, regional nadir maps, limb maps
Meridional motion	Constituent tracers	Comp integrations, far- and mid-IR nadir maps, limb integrations
	Aerosols/diabatic heating and cooling	Far- and mid-IR nadir maps, limb maps
	Potential vorticity (temperature field)	Far- and mid-IR nadir maps, regional nadir maps, limb maps, feature tracks
Waves and vortices	Temperature and comp fields	Far- and mid-IR nadir maps, regional nadir maps, limb maps
Convection	Temperature variance	” ”

Helium. Voyager spacecraft measurements have been used to determine the He abundance on all four giant planets, but recent Galileo probe measurements have raised some questions concerning these results. The primary technique employed with the Voyager measurements uses data from both IRIS and the radio occultation (RSS) experiments. If a particular atmospheric composition is assumed, then the atmospheric mean molecular mass and mean microwave refractivity coefficient can be specified, and a profile of temperature versus pressure can be obtained from the RSS measurements. A theoretical thermal emission spectrum, calculated from a radiative transfer code using this profile, is then compared with spectra measured by IRIS near the occultation point on the planet. The atmospheric composition is adjusted until the theoretical and measured spectra are brought into agreement. This technique yielded a He mass fraction of 0.18 ± 0.04 for Jupiter and the remarkably low value of 0.06 ± 0.05 for Saturn (Gautier *et al.*, 1981; Conrath *et al.*, 1984). Recently, the helium abundance detector (HAD) on the Galileo probe into Jupiter obtained results equivalent to a He mass fraction of 0.238 ± 0.007 (von Zahn and Hunten, 1996), and the probe mass spectrometer measurements were identical to this value (Niemann *et al.*, 1996). Although the 1-σ error bars associated with the Voyager and Galileo results are relatively near one another, close examination of the results suggests the possibility of systematic errors in the Voyager determination. When the Galileo value of the Jovian He abundance is used to calculate a temperature profile from the Voyager RSS results, the theoretical thermal emission spectrum calculated from that profile is about 2 K warmer in brightness temperature than the measured IRIS spectra throughout the entire spectral region 300–800 cm^{-1} (Conrath and Gautier, 2000). The source of possible systematic errors has yet to be identified.

The possibility of systematic errors in the Voyager He abundance determination for Jupiter leads one to ask whether similar problems exist for the Voyager results for the other giant planets, including Saturn. For this reason, the re-determination of the Saturn He abundance has become a major scientific objective for *Cassini*. The same technique that was used in the *Voyager* analyses can be applied to combinations of *Cassini* CIRS spectra and radio occultation measurements (see Kliore *et al.*, 2003). However, in this case, many radio occultation profiles will be available, acquired under differing viewing geometries and at different locations on the planet. Such multiple determinations should be useful in identifying and eliminating possible systematic errors.

A second constraint on the He abundance is provided by the detailed shape of the measured thermal emission spectrum in the far infrared ($\nu < 600$ cm^{-1}). The differential spectral dependence of the collision-induced H_2 absorption in the S(0) and S(1) lines and the translational portion of the spectrum is a function of the relative contributions from H_2–H_2 and H_2–He interactions. Ideally, this effect should permit simultaneous retrieval of both the temperature profile and the He abundance (Gautier and Grossman, 1972). This was done with the *Voyager* Jupiter thermal

emission spectra by Gautier *et al.* (1981). The shape of this portion of the spectrum is also sensitive to the molecular hydrogen *ortho/para* ratio (the ratio of molecular hydrogen in the odd rotational-quantum-number, or *ortho-hydrogen*, state to that in the even rotational-quantum-number, or *para-hydrogen*, state). Gautier *et al.* assumed this ratio to be the thermodynamic equilibrium value at the local temperature. However, it is now realized that the H_2 *ortho/para* ratio is not in equilibrium at many locations on Jupiter (Conrath and Gierasch, 1984; Carlson *et al.*, 1992). Within the portion of the hydrogen absorption spectrum on Jupiter that is free from cloud opacity and ammonia absorption, the effects of He and the hydrogen *ortho/para* ratio are similar, and it is not possible to constrain both parameters simultaneously. Saturn's troposphere, however, is colder than Jupiter's, and more ammonia precipitates out. The reduced cloud and gaseous ammonia absorption in the upper troposphere allows access to a larger portion of the H_2 translational continuum at lower wavenumbers. Measurements in this portion of the spectrum, combined with measurements in the S(0) and S(1) lines, do permit the simultaneous retrieval of temperature, the hydrogen *ortho/para* ratio, and the He abundance. Conrath and Gautier (2000) have reanalyzed Saturn IRIS spectra over its lowest wavenumber range, 200–600 cm^{-1}, and derived a helium mass fraction of 0.18–0.25, considerably higher than the earlier IRIS-RSS result. This technique will be more sensitive using CIRS spectra, because of the additional spectral coverage of the translational continuum below 200 cm^{-1}. Spectra from various locations on the planet can be analyzed, while imposing the additional constraint that, even though the temperature and *ortho/para* ratio vary with location, the He abundance should be the same everywhere. This approach will provide an independent determination. While the formal errors from these results will be larger than from those derived using both CIRS and RSS data, they should serve as a useful constraint in detecting any large systematic errors in the latter approach.

Methane. CH_4 is the primary repository of carbon on Saturn. Previous determinations of the atmospheric CH_4 abundance have relied on near-infrared reflection spectra obtained with ground-based telescopes. Most recent measurements (Karkoschka and Tomasko, 1992) indicate a methane mixing ratio of $(3.0 \pm 0.6) \times 10^{-3}$, yielding $[C]/[H] = (1.3\text{–}2.0) \times 10^{-3}$. This range represents a considerable enhancement relative to the solar value (4.7×10^{-4}), which, as noted earlier, would suggest a heterogeneous origin of Saturn. Scattering from clouds and aerosols complicates the interpretation of the near-infrared data, and this issue has been somewhat controversial (see Prinn *et al.*, 1984).

Retrievals of the CH_4 abundance from spectra obtained in the ν_4 band in the thermal infrared near 1300 cm^{-1}, such as those obtained by Voyager IRIS ($4.3^{+2.3}_{-1.8} \times 10^{-3}$, Courtin *et al.*, 1984) and by the ISO/Short Wavelength Spectrometer ($4.5^{+1.1}_{-2.1} \times 10^{-3}$, Lellouch *et al.*, 2001) have been problematic, because of the difficulty in separating the effects of CH_4 abundance from those of temperature. This general problem is discussed in more detail in Appendix A. With only

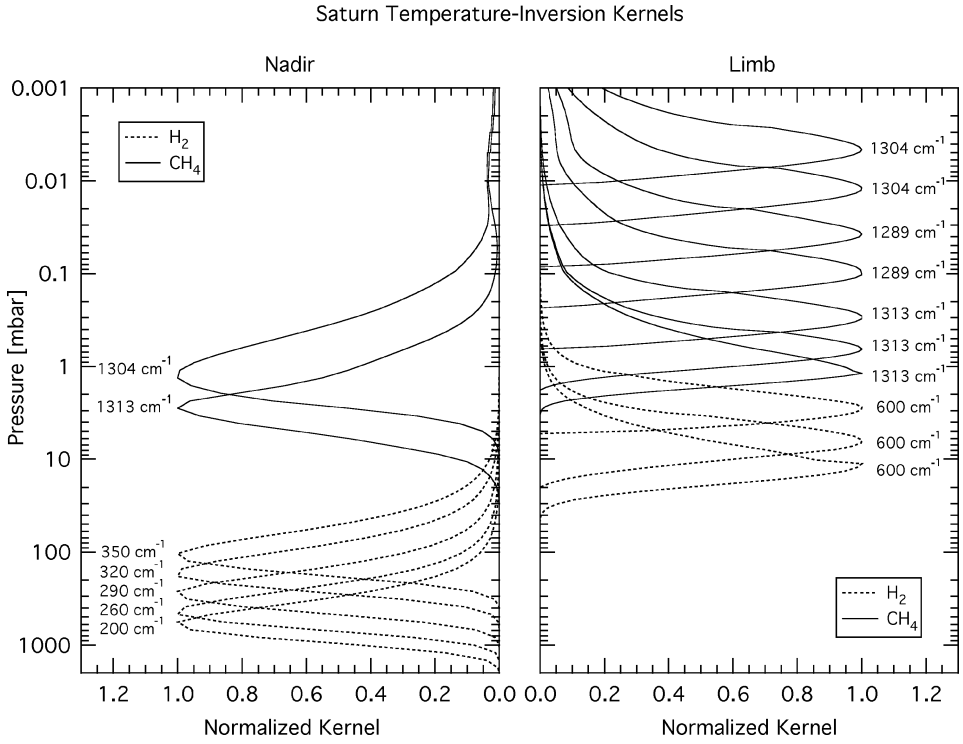

Figure 4. Inversion kernels for temperature sounding of Saturn. The kernels for limb viewing have been convolved with a finite FOV approximated as a Gaussian, whose full width at the 1/e points, projected onto the horizon, equals one scale height.

nadir-viewing observations, as IRIS usually obtained, there is not sufficient redundancy in the spectra to determine [CH_4] uniquely. The capability of limb sounding changes all this. Figure 4 depicts the inversion kernels for temperature retrieval in Saturn's atmosphere from CIRS spectra for both nadir- and limb-viewing geometries. The requisite redundancy in the spectra is evidenced by the slight overlap in the stratosphere of the inversion kernels at 600 cm^{-1} – attributable to absorption in the S(1) line of H_2 – for the limb mode and those in the ν_4-band of CH_4 near 1300 cm^{-1} for nadir viewing. Hence, the combination of CIRS spectra at the two viewing geometries should determine the stratospheric CH_4 abundance. Additionally, the rotational lines of CH_4, in the far-infrared at 60–120 cm^{-1}, illustrated in Figure 5, contain information on tropospheric methane. As methane does not condense in Saturn's atmosphere, the tropospheric and stratospheric abundances should be identical. The line-formation region of the centers of rotational lines, which are seen in absorption, is ∼250 mbar, in the upper troposphere. The requisite redundancy here is afforded by the independent determination of temperature from the simultaneous nadir observations in the spectral region 150–600 cm^{-1}, where pressure-induced absorption by H_2 in the translational continuum and the

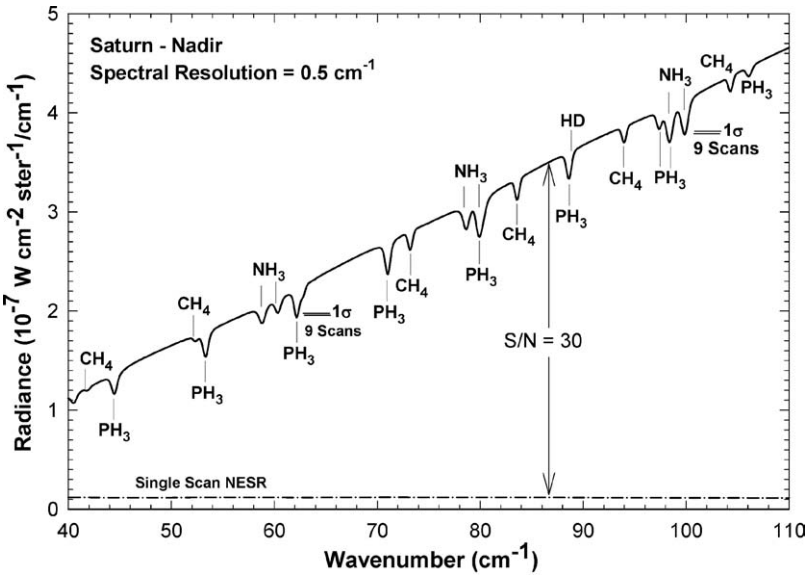

Figure 5. Synthetic far-infrared nadir spectrum of Saturn at high resolution (0.5 cm^{-1}) showing NH_3, PH_3, CH_4, and HD absorption lines, along with the NESR (Section 5.6.1) for a single spectrum and the 1-σ errors for 9 averaged spectra. NH_3 and PH_3 variations across the disk of Saturn will be inferred from these spectral lines

S(0) and S(1) lines dominates the opacity (see Appendix A). Hence, determination of stratospheric and tropospheric methane from two different spectral regions should provide an accurate determination of the atmospheric abundance of this compound.

Ammonia. NH_3 is the principal reservoir of nitrogen on Saturn. Its abundance in Saturn's upper troposphere and higher is severely limited by condensation. NH_3 is usually thought to be the main component of Saturn's visible clouds, although no definite evidence exists. It is photolyzed at pressures $\leq$0.5 bar and, coupled with PH_3 and hydrocarbons, may be involved in complex chemical processes (Kaye and Strobel, 1984). NH_3 varies laterally as well as vertically. Ground-based radio observations of Saturn at 6 cm, which probe the atmosphere between 1.3 and 5 bar, have shown enhanced emission within a broad latitude band extending from 20° N to 50° N (Grossman *et al.*, 1989). The band is thought to be depleted in gaseous NH_3, which permits emission from warmer and deeper regions of the troposphere to be observed. The 700-mbar temperatures retrieved from Voyager IRIS radiances near 225 cm^{-1} also indicated an apparent increase in the same region (Conrath and Pirraglia, 1983). However, the retrievals were based on the assumption that the collision-induced transitions of H_2 provided all the infrared opacity, and they did not include the contributions of clouds. If the cloud opacity was not negligible, then it is likely that the enhanced temperatures at mid northern latitudes result from a minimum in the cloud opacity there, which would be consistent with the radio

observations. The spatial distribution of gaseous NH_3 and clouds must result from atmospheric transport, coupled with condensation and photochemical processes. This cycle is still poorly understood.

CIRS spectra provide a sensitive means to determine the distribution of tropospheric NH_3 on Saturn. Both the ν_2 vibrational band in the mid infrared near 1000 cm^{-1} and the rotational lines visible in the far infrared from 60 to 225 cm^{-1} can be used. Figure 5 depicts a synthetic nadir spectrum at high spectral resolution of the rotational NH_3 lines at Saturn's equator. The high spectral resolution (0.5 cm^{-1}) is needed to separate the multiplets of PH_3 from those of NH_3, and give good discrimination of the weak NH_3 lines against the underlying H_2 continuum. The Noise Equivalent Spectral Radiance (NESR, see Section 5.6.1) is shown for a single high resolution scan (52 s). The H_2 continuum to NESR ratio establishes the accuracy with which the temperature and cloud structure can be retrieved. Over most of the spectral range, the signal-to-noise ratio (SNR) is $\sim$30. The 1-σ error bar shown corresponds to the average of 9 scans, which decreases the NESR by a factor of three, and it indicates the accuracy with which the NH_3 abundance can be retrieved. The SNR is quite adequate for retrieving the NH_3 vertical profile from the observed Saturn radiances. NH_3 abundances will be retrieved in a layer centered at 500 mbar with a vertical resolution comparable to the NH_3 saturation vapor pressure scale height.

Hydrogen sulfide. The Galileo probe mass spectrometer detected H_2S at pressure levels between 8 and 20 bars in Jupiter's deep atmosphere (Niemann *et al.*, 1998). The only remote observation of H_2S on Jupiter was a tentative detection in the stratosphere immediately after the collision of comet Shoemaker-Levy 9 (Yelle and McGrath, 1996; Atreya *et al.*, 1995, claimed only an upper limit from the same ultraviolet data set.) H_2S has not been observed at all on Saturn. The difficulty arises from the depletion of H_2S from the chemical reaction with NH_3 to form the NH_4SH cloud that is thought to exist at a pressure of several bars. Only at 5 μm and beyond 10 cm at radio wavelengths can one probe deeper than this cloud to levels where H_2S is expected to be abundant. However, there are no H_2S bands at 5 μm, and beyond 10 cm, there is a smeared out continuum that makes it nearly impossible to separate NH_3, PH_3, and H_2S. There are strong rotational lines of H_2S between 20 and 80 cm^{-1} within CIRS's FP1 bandpass – not shown in Figure 5 – that sound the $\sim$1-bar level, which is well above the nominal NH_4SH cloud. Weisstein and Serabyn (1996) acquired whole-disk spectra of Saturn using the Caltech Submillimeter Observatory. They reported a stringent upper limit to H_2S on Saturn of 16 ppb using an absorption feature at 687.3 GHz (22.93 cm^{-1}). This is 3 orders of magnitude less than the solar abundance of sulfur, thus supporting the idea that sulfur is locked up in the NH_4SH cloud. Images of Saturn at 5.2 μm reveal interesting spatial structure in the deepest cloud layers (Yanamandra-Fisher *et al.*, 2001), and it is possible for H_2S to be enhanced locally above the very low global average. Hence a search for H_2S, using the CIRS capability of high spectral and spatial resolution, is an important objective.

Isotopic abundances also bear on Saturn's formation and evolution:

Deuterium. It is widely recognized that an accurate determination of [D]/[H] can provide useful constraints on models for the origin and evolution of planetary atmospheres. As H_2 dominates all other hydrogen-bearing constituents by a large margin on both Jupiter and Saturn, one expects the value of [D]/[H] in the H_2 in these atmospheres to be identical to the value in the hydrogen that dominated the interstellar cloud from which the solar system formed. Neither of these giant planets is sufficiently massive to produce internal temperatures and pressures that would permit D-consuming nuclear reactions. The only disturbance of the original ratio would therefore come from other hydrogen compounds that were brought to the forming planet as solids (primarily in ices) in sufficient amounts.

Gautier and Owen (1989) adopted $[D]/[H] = (1.7 + {}^{1.9}_{-1.0}) \times 10^{-5}$ on Saturn, based on various analyses of observations of CH_4 and CH_3D bands (with a correction for the fractionation from hydrogen) by several different observers. More recently, ISO has also observed the rotational lines of HD in absorption in the far infrared (Griffin *et al.*, 1996; Lellouch *et al.*, 2001). Averaging the [D]/[H] retrieved from ISO observations of the R(2) and R(3) HD lines at 265 cm^{-1} and 351 cm^{-1}, respectively, with that retrieved from the observed emission in the CH_3D band near 1150 cm^{-1}, Lellouch *et al.*, derived $[D]/[H] = (1.70 + {}^{0.75}_{-0.45}) \times 10^{-5}$ on Saturn and $(2.25 \pm 0.35) \times 10^{-5}$ on Jupiter. The latter ratio is in good agreement with that derived from direct measurements of HD and H_2 in Jupiter's atmosphere with the mass spectrometer on the Galileo Probe (Mahaffy *et al.*, 1998): [D]/[H] = $(2.6 \pm 0.7) \times 10^{-5}$. The Jupiter ratios are significantly higher than the value of $(1.5 \pm 0.1) \times 10^{-5}$ in local interstellar hydrogen today (Linsky, 1998), as expected from models for galactic evolution that predict the destruction of deuterium with time as a result of nuclear "burning" in stars.

The lower value of [D]/[H] on Saturn is surprising, although the relative errors are large. Interior models (Guillot, 1999) predict that $([D]/[H])_{Saturn}/([D]/[H])_{Jupiter} \sim$ 1.25–1.35, because of mixing of solar nebular gas with D-rich ices at Saturn's orbit. It is important to increase the precision of the [D]/[H] measurement on Saturn in order to decide whether this has occurred. CIRS can accomplish this through improved measurements of HD and deuterated methane.

CIRS can observe the R(0), R(1), and R(2) rotational lines of HD in the far-infrared, illustrated in Figure 6. These have been tentatively identified in CIRS observations of Jupiter obtained during the recent Cassini swingby (Kunde *et al.*, 2004). Even with CIRS's high resolution, the higher spectral resolution ($\sim$0.27 cm^{-1}) afforded by unapodized spectra is needed to resolve these weak features. The R(0) feature appears as a notch in the wing of the stronger PH_3 absorption. The R(1) absorption at 178 cm^{-1} is small, $\sim 2 \times 10^{-8}$ W $cm^{-2} sr^{-1}/cm^{-1}$, and it is imbedded within a NH_3 multiplet. However, a two-hour integration would yield a SNR of 10 for this feature. In addition to HD and NH_3 gas, this part of the spectrum is sensitive to temperature, the para H_2 fraction, He, and NH_3 ice. All but HD and He vary with location. As with He (see above), the constancy of

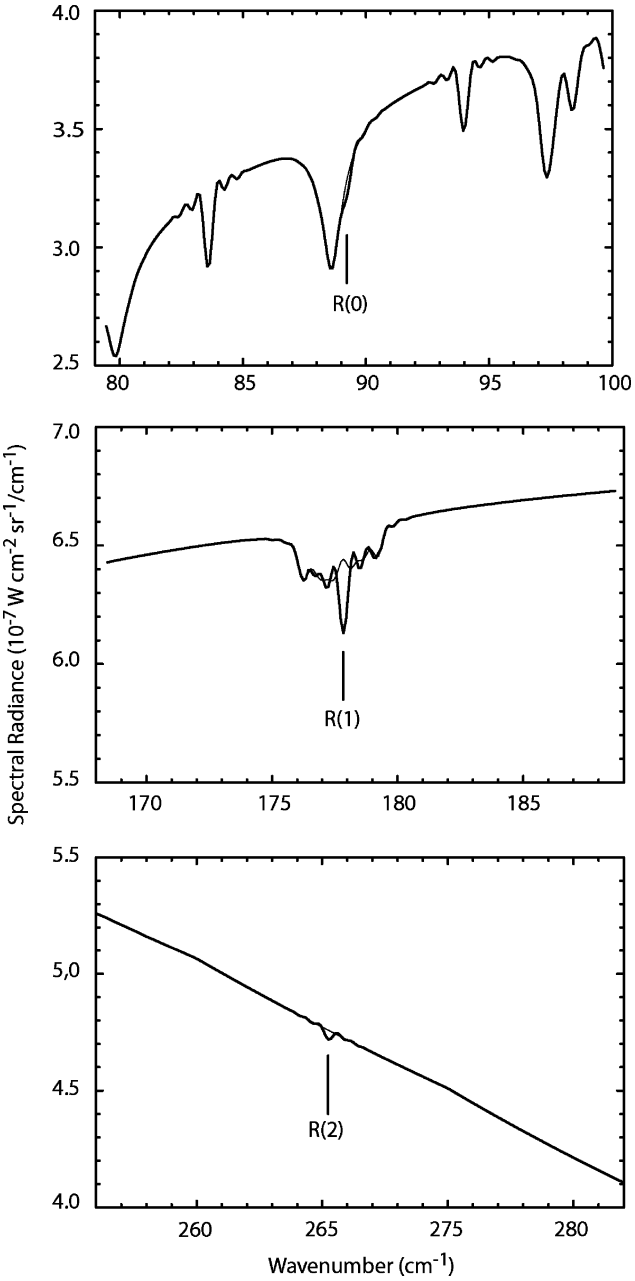

Figure 6. Unapodized 0.27 cm^{-1} synthetic spectra in the far infrared, illustrating the R(0), R(1), and R(2) rotational lines of HD on Saturn. Spectra with and without the HD features are indicated. The R(0) line lies on the high-wavenumber side of a PH_3 absorption, and the R(1) line is embedded within a NH_3 absorption manifold.

HD can be leveraged to separate it from the other sources of opacity. Information on NH_3 in both the gaseous and solid phases, temperature, and the para fraction can be obtained from other parts of the spectrum and also from different viewing geometries. CIRS should be able to surpass the accuracy of the ISO determination.

In addition, [D]/[H] in methane can be inferred from the determination of the$[CH_3D]/[CH_4]$ ratio (e.g.,Lellouch *et al.*, 2001); this comes from spectral regions near 1150 cm^{-1} and 1300 cm^{-1}, where the Q-branches of CH_3D and CH_4 are located, respectively. The spectral resolution accessible to CIRS and the high sensitivity of its detectors in this region (Figure 37) will permit an improved determination of this ratio. In particular, CIRS should improve the ISO determination ($2.0^{+1.4}_{-0.7} \times 10^{-5}$), which was hampered by the existence of temperature variations over Saturn's unresolved disk. Comparing this with [D]/[H] in H_2 should allow one to evaluate the isotopic enrichment factor in methane in the upper troposphere of Saturn. This factor reflects the competition between chemical equilibration at deeper, hotter levels of Jupiter's and Saturn's atmospheres and rapid upward transport to colder levels where the equilibration is quenched (Lecluse *et al.*, 1996; Smith *et al.*, 1996a). A precise determination of this factor would better define the quenching level and the nature of the dynamics of the deep atmosphere, which presently are only poorly constrained. ISO observed both HD and CH_3D on Jupiter and Saturn, but the errors in the [D/H] ratios derived were large enough to preclude a meaningful determination of the enrichment factor (Lellouch *et al.*, 2001).

Carbon isotopes. The ratio $[^{13}C]/[^{12}C]$ is of interest because it is indicative of conditions in the outer solar system (Gautier and Owen, 1983). Galileo probe measurements found $[^{13}C]/[^{12}C] = 0.010820 \pm 0005$ on Jupiter (Niemann *et al.*, 1996, 1998; Atreya *et al.*, 1999, 2003), which is consistent with the solar value. Ground-based measurements in the near infrared (Combes *et al.*, 1997) indicate that the ratio for Saturn is also close to solar. CIRS can observe $^{13}CH_4$ emission at several features between 1290 and 1300 cm^{-1}. Courtin *et al.* (1983) used IRIS data in this spectral region to retrieve $[^{13}C]/[^{12}C]$ on Jupiter, but their value was higher than the solar value. In part this bias stemmed from IRIS's limited spectral resolution of 4.3 cm^{-1}, causing some blending of the $^{13}CH_4$ and $^{12}CH_4$ emission. With its higher spectral resolution, CIRS should be able to separate the emission from these isotopes better. CIRS spectra should also show emission from $^{13}C^{12}CH_6$, near 820 cm^{-1}. As methane and ethane are parent and daughter molecules, respectively, any differences in $[^{13}C]/[^{12}C]$ inferred from their emission may be indicative of fractionation processes.

Internal heat. Saturn radiates more energy in the thermal infrared than it absorbs from sunlight. From Voyager IRIS observations, Hanel *et al.* (1983) have made the most definitive determination of the ratio of emitted radiation to absorbed sunlight, $= 1.78 \pm 0.09$. The excess energy is thought to be from Saturn's interior, attributable to primordial heat loss associated with Saturn's cooling and slow contraction, and possibly the energy release associated with gravitational separation of hydrogen and

helium. The CIRS spectra can determine Saturn's thermal emission more accurately for two reasons. The first is that the far infrared spectrum measured by IRIS only extended down to 200 cm^{-1}. At lower wavenumbers, Hanel *et al.*, used a synthetic spectrum, calculated from the temperatures retrieved from the radiances at higher wavenumbers. CIRS will measure the far-infrared spectra directly down to 10 cm^{-1}. Secondly, the Voyager IRIS coverage for the heat balance study was obtained at a time when the entire disk of Saturn nearly filled the instrument FOV, and a fairly involved correction was required to remove the effects of its rings. The Cassini orbital tour offers an improvement, in that it allows viewing of the entire planet at high spatial resolution at different emission angles.

At the emission-to-space level (400 mbar), Saturn's (and Jupiter's) zonal-mean temperatures (averaged over longitude) are remarkably uniform with latitude. This has been attributed to the efficiency of convective transport of heat within the interior (see, e.g., Ingersoll and Porco, 1978). However, small meridional temperature variations on the scale of the zonal-wind structure are observed (see below). The local variations in the heat balance on these scales are diagnostic of local dynamics, as Pirraglia (1983) has shown for Jupiter, using Voyager IRIS spectra. Detailed thermal mapping by CIRS will elucidate the local variations in thermal emission on Saturn. Unlike IRIS, which had a single-channel visible radiometer, CIRS does not have any sensitivity at solar wavelengths. However, there are other orbiter instruments that measure ultraviolet (Esposito *et al.*, 2003), visible (Porco *et al.*, 2003), and near-infrared (Brown *et al.*, 2003) radiation with photometric precision, and these will provide an improved determination of Saturn's reflected solar radiation. Combining these with CIRS observations in the thermal infrared will more accurately determine Saturn's heat balance on global and smaller scales.

3.1.2. *Atmospheric Gas Composition*

Disequilibrium compounds – troposphere. The molecules phosphine (PH_3), carbon monoxide (CO), germane (GeH_4), and arsine (AsH_3) have been identified in Saturn (Bregman *et al.*, 1975; Noll *et al.*, 1986; Noll and Larson, 1990; Bézard *et al.*, 1989). These compounds are not in thermochemical equilibrium at the pressures ($\leq$several bars) and temperatures ($<$300 K) at which they are observed, and their existence in this part of the atmosphere must result from rapid upward transport from the hotter interior. They therefore serve as valuable tracers of the strength of the deep convective transport and of the chemical state of the interior. In tandem with thermochemical-kinetic models, the observed abundances can constrain the composition of heavy elements in Saturn's interior, a key parameter for theories of its formation and evolution. However, the interpretation of the observed disequilibrium molecules is complicated by the interplay of photochemistry and dynamics at atmospheric levels accessible to short-wave solar radiation. Phosphine, which leads to the formation of more complex molecules and possibly chromophores, provides an illustrative example. The abundance of PH_3 in the atmosphere at pressures $<$1 bar is depleted compared to that measured in the 4–5 bar range (see, e.g., de

Graauw *et al.*, 1997). This depletion has been attributed to UV photolysis or more complex photochemical processes (Kaye and Strobel, 1984). The vertical profile of phosphine results from a balance between vertical mixing and photochemical destruction. Additionally there are probably horizontal variations from the competition between photochemistry and meridional and vertical transports. On Jupiter, phosphine was found to decrease slowly in the 600-mbar region from 10° S to 35° S, which suggests a decrease in the strength of vertical mixing there (Lara *et al.*, 1998). In addition, an enhancement of the deep mixing ratio, at pressures >1 bar was found at high northern latitudes (∼50° N) on Jupiter (Drossart *et al.*, 1990). Recently, Irwin *et al.* (2004) have analyzed CIRS Jupiter data at 1000–1200 cm^{-1} obtained during the Cassini swingby. Although a rapid decrease of PH_3 with altitude above the 1-bar level was consistent with the spectra, they concluded that the 1-bar abundance and fractional scale height retrieved from the nadir-viewing spectra were highly correlated. At low latitudes they observed an enhancement in the 1-bar abundance in the equatorial zone – presumably a region of upwelling – and a depletion over the north and south equatorial belts. Because of the distance (140 R_J) of the Jupiter flyby, Irwin *et al.* were restricted to the middle infrared portion of the spectrum, for which the CIRS detector arrays could spatially resolve the planet for detailed mapping. During the Cassini tour, Saturn can also be mapped in the far infrared, permitting deeper levels of the atmosphere to be probed. Figure 5 illustrates that the far-infrared spectrum is as promising a region to retrieve the spatial distribution of PH_3 as it is for NH_3. The magnitude of the PH_3 rotational lines are comparable to those of NH_3, so the earlier SNR estimates for the latter molecule apply to PH_3 as well.

Mapping the distribution of several non-equilibrium molecules on Saturn will help separate the effects of chemistry and dynamics in the deep atmosphere from those of photochemistry and dynamics in the upper troposphere and middle atmosphere. In addition to the aforementioned molecules, H_2Se, H_2S, and halides (HF, HCl, HBr, HI) are promising candidates (Bézard *et al.*, 1986). None of these, however, have been seen by ISO. Thermochemical models predict that halogens in the observable atmosphere should be trapped in the condensed phase as ammonium salts. Showman (2001) modeled the rapid transport of halides from the deep atmosphere, and he concluded that nucleation and condensation are too rapid to lead to observable supersaturation of these species. Using the strongest lines below 205 cm^{-1}, Fouchet *et al.* (2004a) have analyzed CIRS Jupiter spectra to place upper limits on the mole fractions of the hydrogen halides: $[HF] < 2.7 \times 10^{-11}$, $[HCl] < 2.3 \times 10^{-9}$, $[HBr] < 1.4 \times 10^{-9}$, $[HI] < 1.0 \times 10^{-8}$. The upper limits on [HF] and [HCl] are well below the solar values, supporting the condensation hypothesis. A similar analysis using CIRS spectra of Saturn would be useful for comparative studies of these two planets.

Disequilibrium compounds – Ortho-para H_2 conversion. The ortho-para ratio of molecular hydrogen is a parameter of keen interest in the study of the dynamics and

energetics of the upper tropospheres of the giant planets. At deeper levels where the temperature exceeds 300 K, the value of the ortho-para ratio should be near the 3:1 high temperature limit (called the "normal" value). Since ortho-para transitions are highly forbidden, a parcel of gas initially at a deeper level will tend to retain its initial para fraction when moved upward toward cooler levels, rather than immediately assuming the thermodynamic equilibrium value of the lower temperature (the para fraction at equilibrium increases with decreasing temperature). The extent of disequilibrium will depend on the ratio of the thermal equilibration time to the dynamical transport time, which is not well known in the outer planets. In the upper troposphere of Saturn, the equilibration time for pure molecular hydrogen is approximately 3×10^8 s, but this time can be significantly shortened by catalytic processes, involving, for instance, ortho-para conversion at paramagnetic sites produced by solar photons on cloud particles (Massie and Hunten, 1982; Conrath and Gierasch, 1984). Slow para hydrogen conversion can be a significant factor in the thermodynamics of convective processes, acting essentially as a latent heat (Conrath and Gierasch, 1984; Gierasch and Conrath, 1987; Smith and Gierasch, 1995). Para hydrogen can also serve as a tracer of atmospheric motion; measurements of its spatial distribution can be used to study the upper tropospheric circulation diagnostically.

Previous efforts to determine the hydrogen para fraction in the observable layers of the atmospheres of the giant planets include analyses of measurements of reflected solar radiation in the near-infrared hydrogen lines (Baines and Bergstralh, 1986; Smith and Baines, 1990; Baines *et al.*, 1995) and analyses of emission measurements in the thermal infrared. Retrievals from *Voyager* IRIS thermal emission spectra mapped the para fraction in the upper troposphere at ~100–300 mbar. The para hydrogen was found to be in disequilibrium at low latitudes (Conrath and Gierasch, 1983, 1984; Carlson *et al.*, 1992). From these results, Gierasch *et al.* (1986) inferred the presence of a hemispheric zonal-mean Lagrangian circulation in the upper troposphere and lower stratosphere, with slow upwelling (vertical velocities $\leq 10^{-1}$ mm s^{-1}) at low latitudes and subsidence in the polar regions. Recently, Conrath *et al.* (1998) have extended the analysis of *Voyager* IRIS data to include all four giant planets. Disequilibrum para hydrogen was found on Saturn, with the large scale spatial distribution showing possible seasonal asymmetries. However, the *Voyager* analysis was limited by both the signal to noise ratio of the measurements and incomplete spatial coverage, especially in the southern hemisphere, because of the fly-by geometry. The global average ortho-to-para ratio has also been derived in the stratospheres of the four giant planets, from emission in the H_2 S(0) and S(1) quadrupolar lines measured by ISO/SWS (Fouchet *et al.*, 2003). The measurements were full-disk, except for Jupiter, for which the SWS FOV subtended 30°N to 30°S. The stratospheric para fractions on Jupiter and Saturn were close to the average tropopause values, thus representing a departure from thermodynamical equilibrium.

CIRS measurements will bring several new facets to bear on the study of ortho-para processes on Saturn. The ortho-para distribution derived from Voyager IRIS was retrieved from the far-infrared portion of the spectrum ($<600\ cm^{-1}$), where the effects of temperature, helium abundance, and, at longer wavelengths, NH_3 and PH_3 contribute simultaneously (Conrath *et al.*, 1998; Conrath and Gautier, 2000). The extension of the spectrum below the 200-cm^{-1} limit of Voyager IRIS will provide additional redundancy in the spectrum, allowing a better separation of each of these components (Figure 3). Moreover, it will extend the retrievals deeper, down to the 500-mbar level. The Cassini orbital tour will allow a more complete mapping of the distribution of the para-fraction, and this will be one of the key probes of Saturn's sluggish meridional circulation in the upper troposphere (Section 3.1.4).

Disequilibrium compounds – stratospheric hydrocarbons. The irradiation of CH_4 by solar ultraviolet photons leads to the irreversible production of more complex hydrocarbons. Figure 7 depicts the chemical pathways following the initial breakup of CH_4. The first "tier" of stable products includes acetylene (C_2H_2), ethylene (C_2H_4), and ethane (C_2H_6). C_2H_2 and C_2H_6 were observed in Voyager IRIS

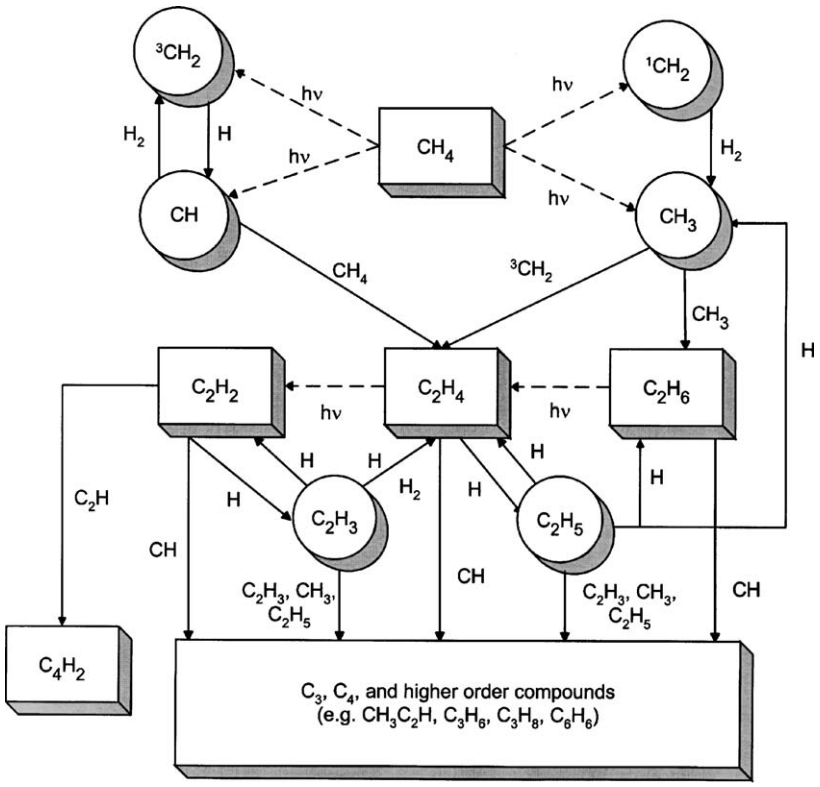

Figure 7. Photolytic reaction scheme for hydrocarbons in Saturn's stratosphere. The rectangular boxes represent stable compounds, the circles denote free radicals, the solid lines indicate chemical reactions, and the dashed lines represent photolysis pathways.

spectra (see, e.g., Courtin *et al.*, 1984), but C_2H_4 has only recently been detected (Bézard *et al.*, 2001a). C_2H_2 is a key component, because it plays a role in the photosensitized destruction of CH_4 to create C_6H_6, and it also leads to higher-order hydrocarbons, such as C_4H_2 and C_6H_2, which are a potential source of the aerosol hazes in Saturn's stratosphere. C_2H_4 is closely linked to C_2H_2, and current models (Moses *et al.*, 2000a) predict a column abundance of C_2H_4 that is five times greater than that inferred from the observations. Uncertainties in some key reaction rates and in branching ratios associated with Ly-α photolysis may account for part of the discrepancy. Disk-average observations of Saturn by the ISO/SWS have also detected diacetylene (C_4H_2), methylacetylene (CH_3C_2H) (de Graauw *et al.*, 1997), and benzene (Bézard *et al.*, 2001b). Current photochemical modeling suggests that the creation and destruction of CH_3C_2H involves its allotrope, allene (CH_2CCH_2), which has not been detected.

All these molecules are infrared active and contribute to the radiative balance of the stratosphere, thereby providing thermal feedback to the photochemistry. Because the Cassini observations will occur at a different season and level of solar activity than those by Voyager, they should provide constraints on the time constants of photochemical and dynamical transport processes. The best disk-resolved observations of Saturn in the thermal infrared are still those by Voyager IRIS. However, Saturn's stratosphere is sufficiently cold, $<$150 K, that it was not possible to retrieve a meridional distribution of any hydrocarbon from the IRIS spectra. Figure 8 illustrates the mid-infrared spectrum of Saturn observed by CIRS at moderate spectral resolution in both the nadir- and limb-viewing geometries. The strong emission features seen from the hydrocarbons C_2H_2, C_2H_6, and C_3H_8 will be used to determine the spatial distributions for these gases. The nadir mode can quickly provide horizontal maps of column densities, but it will usually be necessary to make assumptions concerning the relative vertical profiles. Limb viewing affords much better vertical resolution. Figure 9 illustrates this and demonstrates that vertical profiles can be retrieved at pressure levels spanning 0.01 mbar to several tens of mbar. Figure 8 also shows the NESR for a single FP3 pixel for both viewing geometries (one scan, 10-s integration time). The limb-viewing panel (b) illustrates the 1-σ noise error for an average of nine scans, and it shows that the SNR obtained is adequate to map these stronger species in 90 s. The use of individual pixels for the best vertical resolution is usually critical for limb observations, but nadir observations may be more amenable to pixel averaging, thereby degrading horizontal resolution to optimize the SNR. Figure 8a illustrates one possible strategy, namely averaging 5 pixels. The 1-σ noise error is indicated for this spatial averaging and also for an average of 25 scans. The expected SNR is again very good.

The methyl radical (CH_3) represents a key intermediate stage in the CH_4 photochemistry. Formed by dissociation of CH_4, it ultimately recombines with itself in a three-body reaction to form C_2H_6. Its abundance is sensitive to the poorly known CH_3 recombination rates and to the strength of vertical mixing near the CH_4

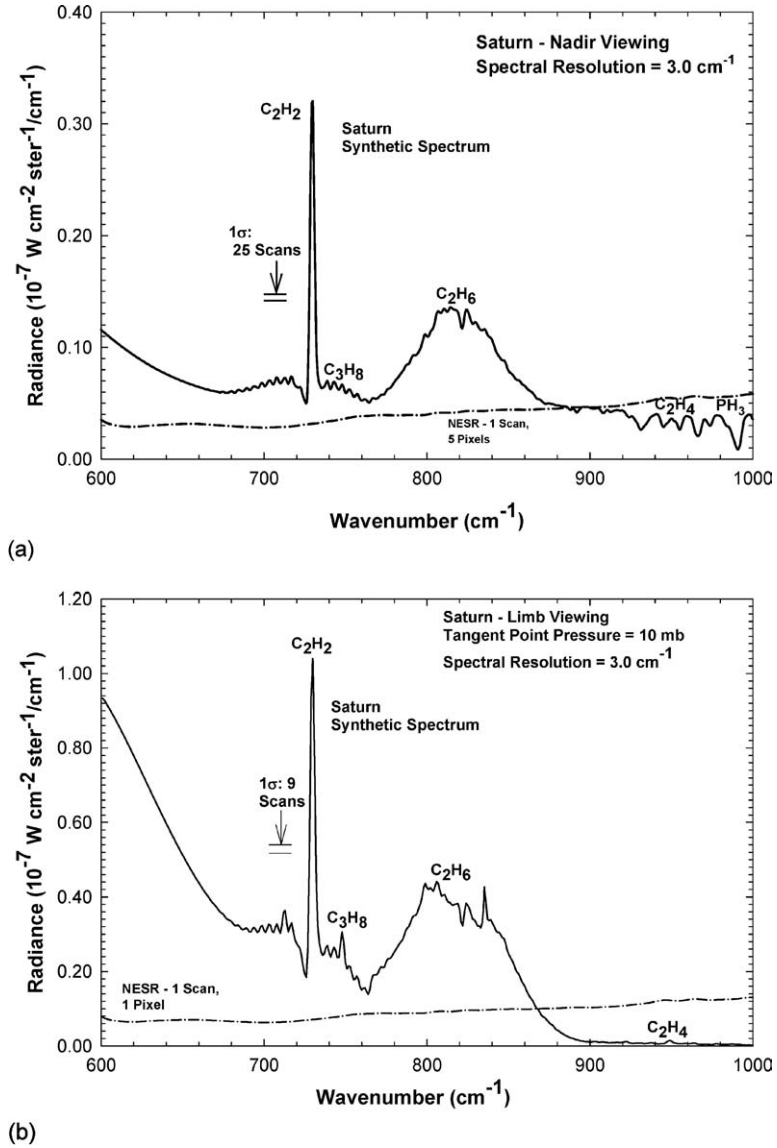

Figure 8. Synthetic mid-infrared spectrum in FP3 at an apodized resolution of 3.0 cm^{-1} for (a) nadir and (b) limb viewing of Saturn. Note the different vertical scales. The single-scan NESR for one pixel is indicated. The 1-σ noise error is also shown for (a) an average of 5 pixels and 25 scans, and (b) a single pixel averaged over 9 scans.

homopause. ISO/SWS spectra of Saturn, with approximately disk-average resolution, led to the first detection of CH_3 and a derived column abundance of 1.5–7.5 $\times$ 10^{13} molec. cm^{-2} (Bézard *et al.*, 1998). The large uncertainty was primarily attributable to the 20% uncertainty in the flux calibration of the SWS spectra, not

only near the CH_3 emission feature at 16.5 μm, but also in the fluxes in the ν_4 band of CH_4 at 7 μm, which were used to constrain the temperature profile at the 0.15–5 mbar altitudes. Still, the ISO observations were enough to indicate that the CH_3 recombination rates were either larger than those currently used in photochemical models, or else the vertical mixing near the homopause was much smaller than previously inferred from Voyager ultraviolet measurements (Bézard *et al.*, 1998). CIRS can improve on the ISO determination in three ways. First, because the optics and detectors are thermostatically controlled, the calibration accuracy is much higher (Section 5). Second, because of its closer proximity to Saturn,

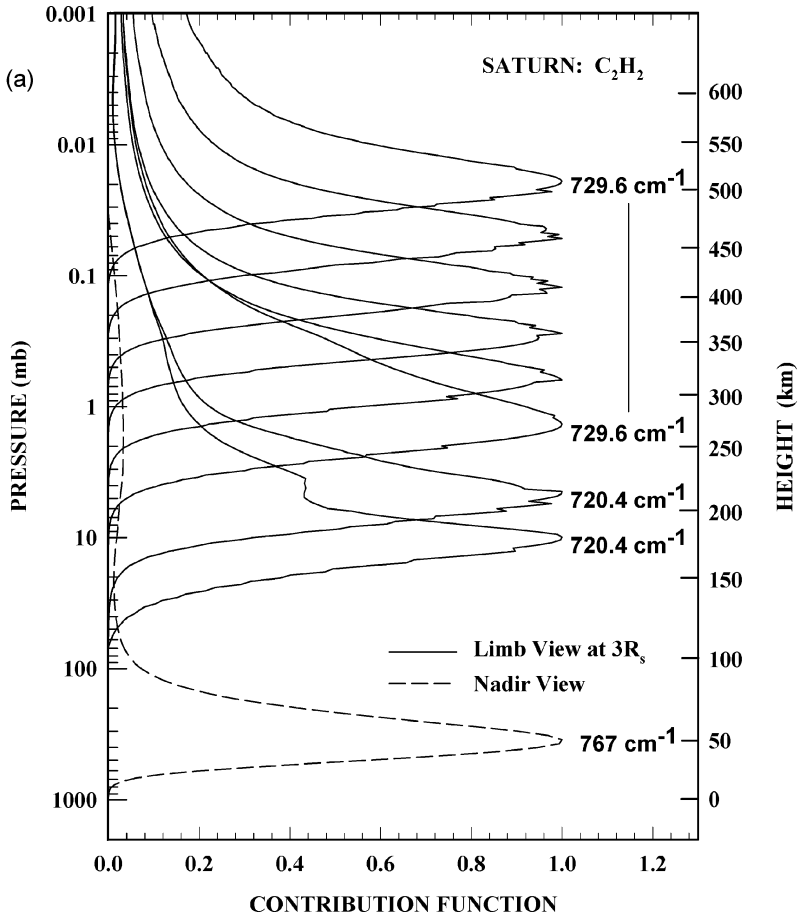

Figure 9. Hydrocarbon contribution functions for C_2H_2 and C_2H_6 for limb and nadir viewing of Saturn. The limb contribution functions have been convolved with a finite FOV whose full width projected onto the horizon equals one scale height. The opacity of tropospheric H_2 accounts for the large peak in the normalized nadir contribution functions at several hundred millibars, but the smaller broad peaks above the 10-mbar level are attributable to the hydrocarbons.

(*Continued on next page*)

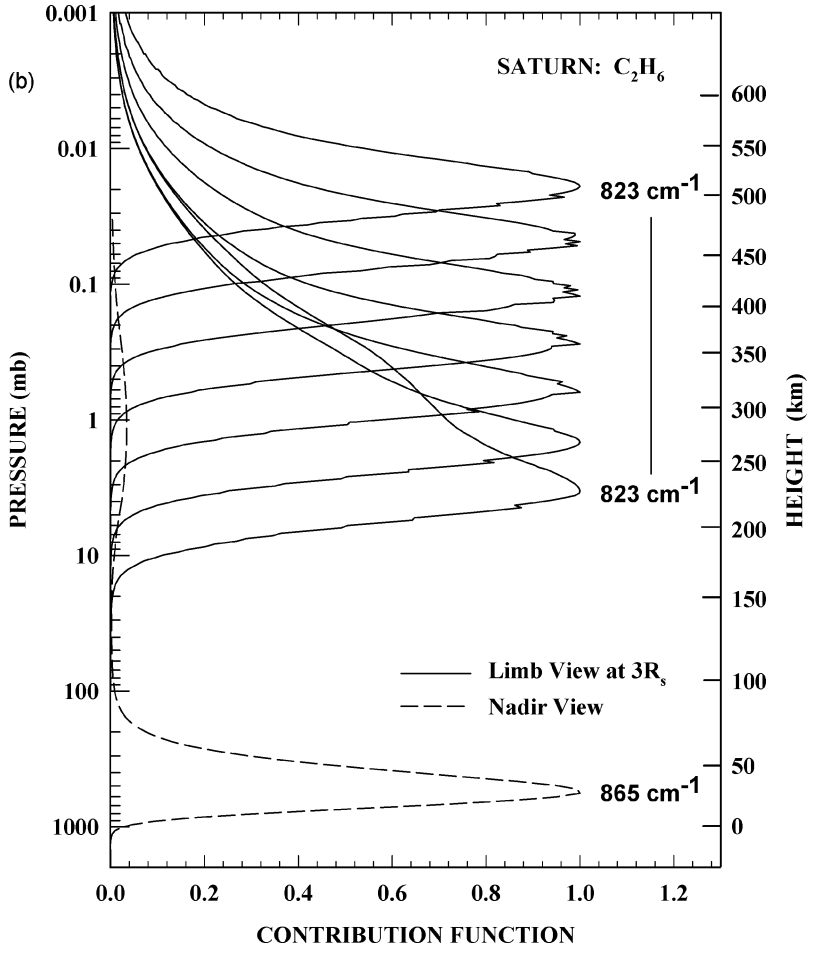

Figure 9. (*Continued*)

the horizontal spatial resolution is much higher, and heterogeneities in emission (e.g., isolating warmer regions) can be used to advantage for detection. This enabled CIRS to detect CH_3 on Jupiter for the first time, within its auroral hot spots (Kunde *et al.*, 2004). Finally, near periapses, CIRS can actually observe Saturn in the limb mode, measuring radiances as high as the 10-μbar level. This will be important in better constraining the temperature profile at high altitudes. Photochemical models suggest that the CH_3 mole fraction is maximum near the CH_4 homopause.

Coupling between CH_4 and PH_3 photochemistry could produce additional organics, mainly alkylphosphines and HCP, as suggested by laboratory experiments (Bossard *et al.*, 1986). These compounds have strong signatures in the mid-IR and could be detected by CIRS.

External sources – oxygen compounds. Although carbon monoxide in Saturn's atmosphere was discovered more than a decade ago (Noll *et al.*, 1986), its vertical distribution and origin are still unknown. Recently, the ISO/SWS detected H_2O and CO_2 on Saturn (Feuchtgruber *et al.*, 1997). The H_2O and CO_2 lines were seen in emission, indicating that the source of the emission was the stratosphere, where temperature increases with altitude. The inferred mixing ratio of H_2O (Table III) is well above the saturation values near the tropopause, and this strongly suggests an external supply of oxygen in the form of H_2O and perhaps O. The external source has not been unambiguously identified, as both interplanetary dust and material originating from the rings or satellites are plausible water-carriers. Determining the spatial distribution of H_2O could discriminate among these possibilities. For example, while "interplanetary" water is expected to be horizontally uniform on the planetary disks, water from the rings should be locally enhanced at latitudes magnetically connected to the rings (Connerney and Waite, 1984). Indeed, FUV spectra recorded by HST at several latitudes suggest that H_2O may not uniform over Saturn's disk, but be significantly enhanced at mid-southern latitudes (Fouchet *et al.*, 1996; Prangé *et al.*, 1999).

The CO_2 observed in Saturn's stratosphere could result from the infall of CO_2 ice contained in micrometeorite/ring/satellite material (Feuchtgruber *et al.*, 1997). Alternatively, secondary production from the reaction of CO and OH can serve as a source of CO_2, where OH is produced from the photolysis of infalling H_2O, and CO is at least partly deposited from external debris. Such a scheme has been proposed for Titan (see below). A recent detailed photochemical model (Moses *et al.*, 2000b) indicates that all these mechanisms could be at work. The derived mixing ratio of CO_2 is so small (Table III), that no condensation should occur at the tropopause and an interior source is theoretically possible. This would require rapid upward transport from the 1200 K level (Feuchtgruber *et al.*, 1997). In this case, the mixing ratio in the troposphere, as yet unmeasured, should be comparable to the stratospheric value. However, Lellouch *et al.* (2002) have estimated that an internal source accounts for only $\sim 10^{-2} - 10^{-1}$ of the CO_2 observed on Jupiter.

Given the small fields of view and the viewing proximity afforded by the orbital tour, CIRS observations should determine the lateral variation of H_2O and the vertical variation of CO_2. The strongest H_2O feature is the rotational line at 150.5 cm^{-1}, in FP1 (see Figure 19, which illustrates this for Titan). Scaling disk-averaged ISO observations of H_2O at 254 cm^{-1}, it follows that 10 h of integration time should provide a SNR of 5. Several locations could be observed during the orbital tour. The vertical variation of CO_2 is best determined from limb observations at 667 cm^{-1} with the FP3 arrays. Nadir observations would provide a column abundance. Again scaling the disk-average radiance observed by ISO, at this wavenumber, indicates that achieving a SNR = 5 requires 100 h of integration. This is fairly long, but it could be broken into shorter segments over a 4-year tour, and the spectra later averaged for analysis.

TABLE III
Atmospheric composition of Saturn (mole fractions).

Gas	Chemical formula	Composition (mole fractions)
Helium	He	0.10–0.13[a]
Methane	CH_4	$4.3(+2.3/-1.8) \times 10^{-3}$[b]
		$(3.0 \pm 0.6) \times 10^{-3}$[c]
		$4.5(+1.1/-2.1) \times 10^{-3}$[d]
Ammonia	NH_3	$\sim 1 \times 10^{-4}$ (3 bar)[e]
Hydrogen sulfide	H_2S	Undetected
Phosphine	PH_3	$7(+3/-2) \times 10^{-6}$ (p > 400 mbar)[f]
		$\sim 4.2 \times 10^{-6}$ (global, 3 bar); $\sim 2.5 \times 10^{-6}$ (global, 300 mbar)[e]
		$\sim 7.4 \times 10^{-6}$ (p > 630 mbar); $\sim 4.3 \times 10^{-7}$ (150 mbar)[g]
Arsine	AsH_3	$2.4(+1.4/-1.2) \times 10^{-9}$ (3 bar)[h]
		$(3 \pm 1) \times 10^{-9}$ (3 bar)[f]
Germane	GeH_4	$(4 \pm 4) \times 10^{-10}$ (3 bar)[f]
Methyl radical	CH_3	$4\ (+2/-1.5) \times 10^{13}$ molec cm^{-2} (global, p $\leq$ 10 mbar)[i]
Ethane	C_2H_6	$(3.0 \pm 1.1) \times 10^{-6}$ (N. hemisphere, p $\leq$ 20 mbar)[b]
		$(9 \pm 2.5) \times 10^{-6}$ (global, 0.5 mbar)[f]
Acetylene	C_2H_2	$(2.1 \pm 1.4) \times 10^{-7}$ (N. hemisphere, p $\leq$ 20 mbar)[b]
		$1.2(+0.9/-0.6) \times 10^{-6}$ (global, 0.3 mbar)[i]
		$(2.7 \pm 0.8) \times 10^{-7}$ (global, 1.4 mbar)[i]
Ethylene	C_2H_4	$\sim 3 \times 10^{15}$ molec cm^{-2} (non-auroral, p $\leq$ 10 mbar)[j]
Methylacetylene	CH_3C_2H	$(1.1 \pm 0.3) \times 10^{15}$ molec cm^{-2} (global, p $\leq$ 10 mbar)[i]
Propane	C_3H_8	detected[k]
Diacetylene	C_4H_2	$(1.2 \pm 0.3) \times 10^{14}$ molec cm^{-2} (global, p $\leq$ 10 mbar)[i]
Benzene	C_6H_6	$4.7(+2.1/-1.1) \times 10^{13}$ molec cm^{-2} (global, p $\leq$ 10 mbar)[l]
Water	H_2O	$(1.4 \pm 0.4) \times 10^{15}$ molec cm^{-2} (global, p $\leq$ 10 mbar)[l]; $\sim 2 \times 10^{-7}$ (3–5 bar)[e]; subsaturated at $p < 3$ bar[e]
Carbon monoxide	CO	$(1 \pm 0.3) \times 10^{-9}$ (3 bar)[f]
Carbon dioxide	CO_2	$(6.3 \pm 1) \times 10^{14}$ molec cm^{-2} (global, p $\leq$ 10 mbar)[m]

[a]Conrath and Gautier (2000).
[b]Courtin *et al.* (1984).
[c]Karkoschka and Tomasko (1992).
[d]Lellouch *et al.* (2001).
[e]de Graauw *et al.* (1997).
[f]Noll and Larson (1990).
[g]Orton *et al.* (2001).
[h]Bézard *et al.* (1989).
[i]Moses *et al.* (2000a).
[j]Bézard *et al.* (2001a).
[k]Greathouse *et al.* (2003).
[l]Bézard *et al.* (2001b).
[m]Moses *et al.* (2000b).

3.1.3. *Clouds and Aerosols*

Clouds on Saturn are expected to result from condensation of volatiles transported upward from deeper, warmer levels of the troposphere. Thus, a solid NH_3 condensate cloud should form near or just above the 1-bar level (Tomasko *et al.*, 1984). Photochemical products, such as C_2H_2, form high in the atmosphere and can condense near the cold tropopause after being transported downward (Carlson *et al.*, 1988). Photochemistry and condensation may also produce solid C_4H_2 or P_2H_4 (West *et al.*, 1986). The characterization of the spatial distribution of cloud and haze material and their properties is an important task of the CIRS investigation for several reasons. First, clouds and aerosols affect the observed radiances within several spectral regions; accounting for their opacities accurately is often required for the retrieval of temperatures and gaseous abundances from CIRS and other remote sensing data. They also play an important role in the radiative heating and cooling of the atmosphere. An interesting goal will be to determine whether any intermediate-term (between seasonal and diurnal) changes in cloud properties take place in regions which are in or have recently undergone ring shadowing. Finally, the spatial distribution of clouds and aerosols is diagnostic of chemistry and dynamical transport.

CIRS spectra are most sensitive to particles greater than 1 μm in radius. The influence of tropospheric clouds will be detected in regions of weakest gaseous absorption. For the far infrared, a comparison of Voyager IRIS and radio occultation results (Conrath *et al.*, 1984, see Section 3.1.1), for example, suggested that the influence of tropospheric clouds was evident at frequencies less than about 250 cm^{-1}, ordinarily a spectral region sensitive to temperatures near 800 mbar. Since this is probably within the region of the atmosphere dominated by small-scale thermally driven convection, variations of brightness below 250 cm^{-1} are probably indicative of cloud variability, rather than major changes in the temperature lapse rate (Section 3.1.4). The size of particles can be determined in this spectral range by inspecting the spectral extent of the cloud influence. Consider, for example, two clouds with equal opacity at 200 cm^{-1}, one cloud composed of 1-μm particles, and a second cloud with 100-μm particles. While the first cloud may not influence the spectrum at wavenumbers less than 130 cm^{-1}, the 100-μm cloud affects the spectrum out to 80 cm^{-1}. The distribution of these particles with altitude can be determined using observations at different emission angles. For instance, at a distance of 4 Saturn radii, spectra obtained with the emission angle as large as 78° at the center of the 4-mrad FP1 FOV will allow us to probe 1.6 pressure scale heights above emission detected from nadir observations. For such spectra, the airmass does not vary by more than 40% over the FOV, which is acceptable. Determination of the height dependence is particularly important to regions, such as the equator, where evidence for high cloud tops (Tomasko *et al.*, 1984) requires attention to distinguishing carefully between temperature and cloud variability above the 600-mbar level, where temperature sounding is generally considered "safe" from cloud influences.

Observations with 15.5-cm^{-1} resolution are acceptable for wavenumbers at or greater than 120 cm^{-1} and 3-cm^{-1} resolution for wavenumbers less than 120 cm^{-1} in order to avoid confusion by significant absorption features of NH_3 or PH_3. Figure 5 shows that there is easily sufficient signal to accommodate these observations in rather short time intervals.

CIRS spectra can also be used to probe particulate opacity in the mid-infrared, for instance, near 897 cm^{-1} (between C_2H_6 emission and PH_3 absorption, cf. Figure 3), near 1100 or 1180 cm^{-1} (a region of PH_3 and CH_4/CH_3D absorption), and near 1392 cm^{-1} (where CH_4 and H_2 are the only gaseous absorbers). Information from these regions would provide an additional discriminator of particle size, allowing broader size distributions or multiple size distributions to be diagnosed. By virtue of the smaller FP3 and FP4 pixel sizes, it would facilitate cloud mapping at high spatial resolution, during nadir stratospheric temperature sounding maps, for example. It would permit cloud parameters to be determined with sufficient independence to separate the influences of clouds from temperature structure in the far infrared, allowing temperature sounding deeper than the 600-mbar level.

Limb spectra taken for stratospheric temperature sounding can be examined for evidence of emission from condensates and aerosols, which often have slowly varying absorption spectra. We would ordinarily expect stratospheric particles to be sub-micron in size and have little influence on the spectrum, but the exponential dependence of the Planck function for the warm stratosphere in FP3 and FP4 provides an increased sensitivity to slowly varying "continuum" absorption at low optical thickness. Difficultly in reconciling simultaneous Voyager IRIS and radio occultation results for latitude 30°S (Conrath *et al.*, 1984) could be explained by an emitting aerosol in the warm stratosphere (Section 3.1.1). Because the background is deep space, limb spectra would unambiguously probe the presence of such an aerosol.

3.1.4. *Atmospheric Structure and Circulation*

Temperatures and zonal winds. Meteorological studies of Saturn have been limited, because winds and temperatures have for the most part only been measured at and above the visible cloud tops. Wind velocities have been retrieved from tracking discrete cloud features wherever they appeared. The most detailed results have been from Voyager (Smith *et al.*, 1981, 1982) and Hubble Space Telescope imaging observations (Barnet *et al.*, 1992; Sánchez-Lavega *et al.*, 2003). These indicate a pattern of zonal (i.e., east-west) currents roughly symmetric about the equator. In addition, there are several vortices and wave-like features.

Remote-sensing thermal-infrared and radio-occultation data have provided the means to retrieve temperatures in the upper troposphere and stratosphere of Saturn, mostly above the clouds. The flyby of Pioneer 11 in 1979 provided the first radio occultation that allowed retrieval of a temperature profile in the tropopause region and stratosphere, from ∼200 mbar to 2 mbar (Kliore *et al.*, 1980). The two Voyager flybys in 1980 and 1981 yielded two additional radio occultations (each with a

recorded ingress and egress), which obtained temperatures from 1 mbar to as deep as the 1.3-bar level, where the signal was extinguished by NH_3 absorption (Lindal *et al.*, 1984). Infrared sounding has provided more extended spatial coverage, albeit with less vertical resolution, typically no better than 1 scale height. Ingersoll *et al.* (1984) summarize the earliest ground-based infrared studies, which had low spatial resolution. The Pioneer 11 infrared radiometer had two broad spectral bands at 20 and 45 μm, which provided information on upper-tropospheric temperatures at low latitudes (Orton and Ingersoll, 1980; Ingersoll *et al.*, 1980). More extensive mapping of Saturn's atmospheric temperatures was provided by infrared spectra measured by IRIS on the Voyager spacecraft. IRIS usually observed in the nadir-viewing mode (Figure 2), and it had a spectral range from 200 to 2500 cm^{-1} (50 to 4 μm) and a uniform spectral resolution of 4.3 cm^{-1}. Figure 10 illustrates typical vertical profiles of temperature retrieved from IRIS spectra. The radiances between 200 and 700 cm^{-1} lie within the S(0) and S(1) pressure-induced hydrogen rotation lines and part of the hydrogen translational continuum (Figure 3), and allow retrieval of temperatures in the troposphere and tropopause region between the 80 and 700 mbar levels. This is illustrated by the inversion kernels in the left panel of Figure 4. The radiances in the ν_4 band of CH_4 (1200–1400 cm^{-1}) permit retrieval of temperatures in the upper stratosphere near the 1-mbar level. The spectra contain little information between 10 and 80 mbar, so the profiles within this region are more or less an interpolation between the bounding regions. The shape of the

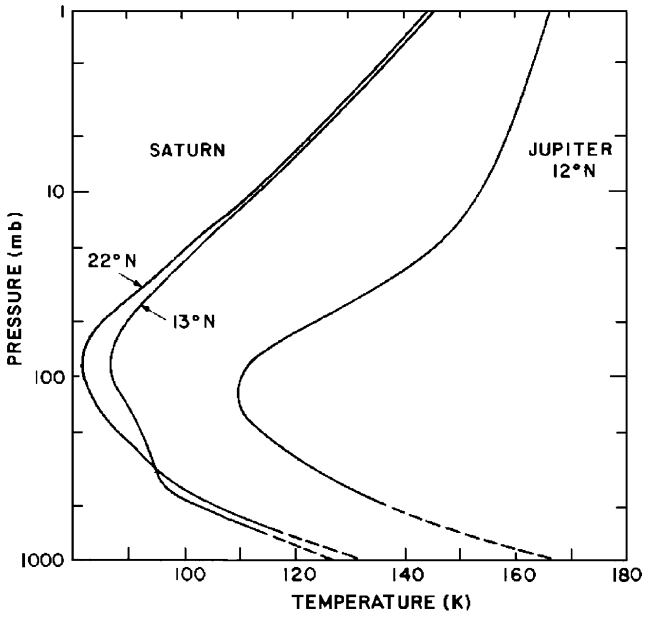

Figure 10. Vertical profiles of temperature for Saturn retrieved from Voyager IRIS observations, compared with Jupiter (Hanel *et al.*, 1980).

22°N profile in Figure 10 is typical of mid northern latitudes during the Voyager encounters. It exhibits a well-defined troposphere (where temperature decreases with altitude) below the 100-mbar level, overlain by a well-defined stratosphere (where temperature increases with altitude), which is similar to the thermal structure seen in Jupiter's atmosphere. The shape of the 13°N profile, on the other hand, typifies low latitudes and much of the southern hemisphere. It exhibits a distinct "knee" in the tropopause region. The cause of this shape difference has never been satisfactorily explained.

IRIS spectra also allowed mapping of temperatures with latitude, at least in the troposphere and tropopause region. Figure 11 illustrates temperatures at three pressure levels. At the deepest level shown, 730 mbar, temperature exhibits little structure with latitude, except for a 4 K warm anomaly at mid northern latitudes, discussed earlier. With increasing altitude, the meridional variation in temperature exhibited a progressively more pronounced north-south asymmetry and a smaller-scale structure that is correlated with the meridional variation of zonal winds that have been inferred from tracking discrete cloud features (Smith *et al.*, 1981). The hemispheric asymmetry is probably a consequence of the radiative-thermal inertia of the upper troposphere and lower stratosphere. At 730 mbar, the relaxation time is long compared to a season, and little seasonal variation is expected. The

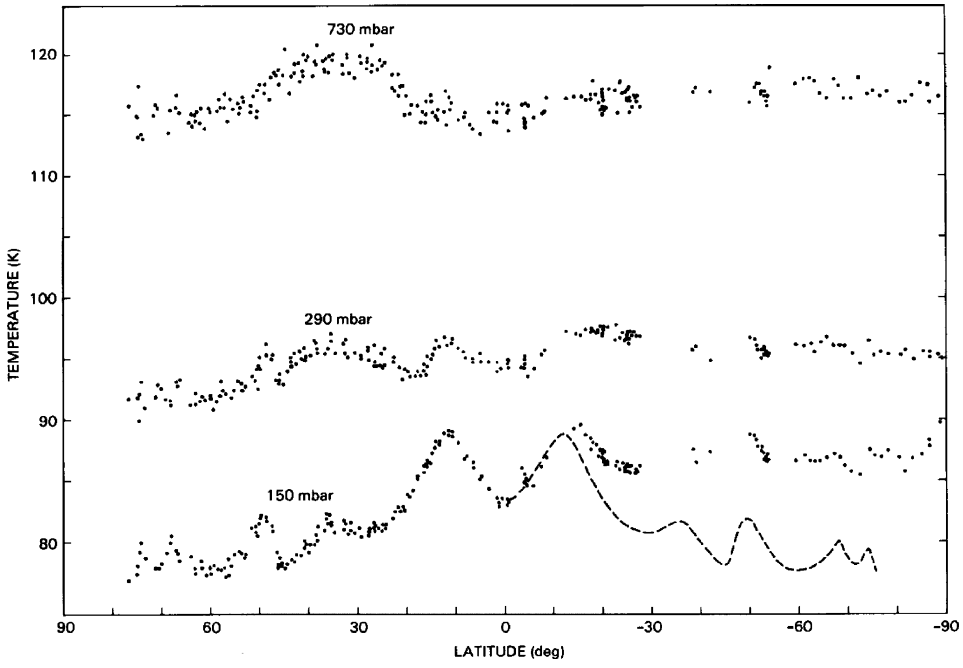

Figure 11. Saturn atmospheric temperatures at three pressure levels as function of latitude, derived from Voyager IRIS observations. The dashed curve in the southern hemisphere at the 150-mbar level is a reflection about the equator of the northern-hemisphere temperatures (Conrath and Pirraglia, 1983).

radiative relaxation time is 2×10^8 s near 150 mbar, comparable to the seasonal time scale; the thermal response there is expected to lag that in radiative equilibrium with the current solar forcing (Conrath and Pirraglia, 1983; Bézard *et al.*, 1984). The Voyagers flew by Saturn shortly after Saturn's northern spring equinox, so the southern hemisphere should be warmer, which is what is observed. Two decades of ground-based observations of Saturn's stratosphere at 7.7 μm (1300 cm^{-1}) have also displayed a seasonal lag of this magnitude (Orton *et al.*, 1989, 2003).

The wind and temperature fields in planetary atmospheres are dynamically coupled. In rotating systems, this gives rise to a diagnostic relation, the thermal wind equation, that relates horizontal temperature gradients to vertical shears in horizontal winds. For example, meridional gradients in temperature and zonal winds are related by (Holton, 1979):

$$\frac{\partial}{\partial \ln p}\left[u\left(2\Omega \sin \Lambda + u\frac{\tan \Lambda}{r}\right)\right] = \frac{R}{r}\left(\frac{\partial T/\mu}{\partial \Lambda}\right)_{\mathrm{p}} \approx \frac{R}{r\mu}\left(\frac{\partial T}{\partial \Lambda}\right)_{\mathrm{p}}, \tag{1}$$

where p is pressure, Λ is latitude, r is radius, R the universal gas constant, μ is the molecular mass of Saturn's atmosphere, $\Omega = 1.66 \times 10^{-4}$ s is the rotation rate of Saturn's interior, assumed identical to the Saturn Kilometric Radiation rotation rate (Desch and Kaiser, 1981), T is temperature, and u is the zonal wind velocity. The thermal wind equation permits the largely two-dimensional wind field derived from cloud-tracked studies to be extended to higher altitudes. From (1), the smaller-scale undulations in the 150-mbar temperatures in Figure 11 imply a slow decay of the zonal winds with altitude, with a vertical decay scale $\sim$5 pressure scale heights. Curiously, the decay in Saturn's stratosphere is toward a state of uniform angular velocity that is eastward with respect to the interior rotation (Conrath and Pirraglia, 1983). The retrieved tropopause temperatures for all the giant planets imply a decay of the zonal currents, at least in the tropopause region. Application of a simple axially symmetric linear model, parameterized with Newtonian cooling and Rayleigh friction, indicates that the zonal winds in this region can be interpreted as the response of frictional and radiative damping to a zonal wind system that is forced at deeper levels. The mechanism providing the vertical decay is not known. In the earth's middle atmosphere, momentum flux divergences associated with the decay of vertically propagating waves are known to be an important mechanism for damping zonal jets (see, e.g., Andrews *et al.*, 1987). Alternatively, Orsolini and Leovy (1989, 1993a,b) and Pirraglia (1989) have interpreted the vertical decay of the jets as a natural consequence when a deep zonal flow in the quasi-adiabatic atmosphere extends upward to the more stably stratified upper troposphere and stratosphere. Instabilities in the wind field generate eddy fluxes that stabilize the zonal winds by acting as a drag force, establishing a vertical decay in the flow profile.

Detailed mapping of the temperatures and winds of the stratospheres of the giant planets has been limited or nonexistent. Ground-based observations, using the ν_4-band of CH_4, have not achieved good vertical resolution in the stratospheres, primarily because of telluric absorption. Voyager IRIS did not have this problem and had adequate spectral resolution to resolve vertical structure in the stratosphere better, but it lacked the sensitivity in the mid-infrared needed for global mapping. CIRS has both the requisite sensitivity and vertical resolution. The Cassini swingby of Jupiter in December 2000 has shown the complexity in the temperature and zonal-wind fields of that planet's stratosphere. The zonal winds derived from the retrieved temperatures do not exhibit the monotonic decay with altitude that characterizes the tropopause region. Indeed, the zonal wind field exhibits a strong equatorial jet centered in the upper stratosphere at 4 mbar (Flasar *et al.*, 2004), which may be driven by the stresses associated with vertically propagating waves (see below).

At Saturn, CIRS gains two additional advantages. First, the orbital geometry afforded by the Cassini tour will allow a more complete thermal spatial mapping of Saturn's atmosphere than previous spacecraft and ground-based observatories could provide. Second, at Saturn, CIRS can also acquire mid-infrared spectra on the limb, at least near periapsis, where the typical range is 3–6 R_S, and the FP3 and FP4 pixel resolution is 1–2 scale heights. (CIRS spectra of Jupiter were largely limited to nadir-viewing observations, because of the 138 R_J swingby distance.) The inversion kernels in the right panel of Figure 4 indicate that limb spectra not only fill in the gap between 10 and 80 mbar left by nadir spectra, but can also extend the range of altitudes up to the 0.01-mbar level. Appendix A discusses the retrieval of atmospheric temperatures from CIRS spectra in more detail.

Meridional circulations. Perhaps the best-known meridional circulation is the terrestrial Hadley circulation, in which high-altitude velocities are poleward, and near-surface velocities equatorward (see, e.g., Lorenz, 1967). This is an example of a thermally direct circulation: warm air near the equator rises, and colder air at mid-latitudes sinks. While one may think that radiative heating and cooling are the drivers of the Hadley circulation, even in this simple case friction is necessary to achieve a steady, balanced flow (see, e.g., Held and Hou, 1980). The tendency of air parcels to conserve axial angular momentum and spin up or down, depending on whether they move poleward or equatorward, is balanced by frictional coupling to the surface. More generally, terrestrial meteorological studies have indicated that zonal-mean meridional circulations are not always thermally direct, and the zonal momentum and heat deposition associated with eddies and propagating waves are important in driving these circulations. However, for zonal-mean flows in thermal wind balance (Equation (1)), the forced meridional circulations tend to cancel the heat and momentum transports by the eddies/waves themselves. In the limit in which the eddies/waves are conservative – not internally forced by some instability, not subject to dissipation or radiative damping – and steady, the cancellation is complete and the net effect of eddy/wave forcing on the zonal-mean flow is zero (Charney and Drazin, 1961; Eliassen and Palm, 1961; Andrews *et al.*, 1987). In

general, this limiting state is not fully realized. Nonetheless, it is the residual mean meridional circulation – the circulation with the eddy/wave fluxes of heat and momentum subtracted out – that is relevant for studies of the general circulation, because it, and not the zonal-mean Eulerian circulation, contains the relevant heat and momentum transports. Dunkerton (1978) has shown that the residual mean meridional circulation in the terrestrial stratosphere and mesosphere approximately corresponds to the Lagrangian circulation, which describes constituent transport.

The terrestrial studies are based on very general concepts, and they should be applicable to the atmospheres of the giant planets, perhaps not so much in the deep tropospheres where convection and dissipation are important, but certainly at higher altitudes, near the tropopauses and in the stratospheres and mesospheres. CIRS spectra are well suited for probing the residual mean meridional circulations on Saturn in several ways:

1. *Gaseous and particulate tracers*. CIRS will acquire maps of several gaseous constituents with good vertical resolution. The discussion in Section 3.1.2 noted that the departure of the H_2 para fraction from the local thermodynamic equilibrium value is a good indicator of vertical Lagrangian velocities. The retrieved para fractions from Voyager IRIS spectra of Jupiter implied a simple global-scale circulation in the tropopause region, with upwelling at low latitudes and subsidence at high latitudes in both hemispheres (Conrath and Gierasch, 1984). The IRIS spectra implied planetary-scale spatial structure in the para fraction on Saturn, and CIRS will provide more detailed mapping with higher sensitivity.

   Gaseous NH_3 is another good tracer of motions, because it condenses and is not uniformly distributed. Zonal mean abundances at the ∼700-mbar level, retrieved from IRIS spectra of Jupiter in the far infrared at 216 cm^{-1} (Gierasch *et al.*, 1986), showed a variation with latitude that was anti-correlated with temperatures, i.e., higher abundances occurred where the zonal-mean temperatures in the upper stratosphere were colder, an indicator of upwelling (see below). Using the more sensitive CIRS data in the mid-infrared near 1000 cm^{-1}, from the Jupiter swingby, Achterberg *et al.* (2003) also concluded that enhanced zonally averaged NH_3 abundances were correlated with colder temperatures. IRIS Saturn spectra did not have an adequate SNR to permit NH_3 retrievals, but as noted earlier, this is not a problem for CIRS, which will obtain retrievals both in the mid- and far-infrared. PH_3 is also a good tracer, as noted earlier.

   Stratospheric hydrocarbons should provide a rich mix of motion indicators. Here the physics depends largely on the magnitude of the photochemical time constants relative to dynamical time scales. When the latter are smaller, lateral transports are efficient and constituent mole fractions should be laterally uniform. When the former are smaller, constituent abundances should be governed by photochemical processes and exhibit strong latitude variations. Consider C_2H_6 and C_2H_2. The loss time constants for photochemical destruction are ∼50 years and 1 year, respectively, near 10 mbar. Estimates of the dynamical turnover times for

the upper troposphere on Jupiter and Saturn, based on the temperature and para-hydrogen fields (see below), are 70 years and 200 years, respectively (Conrath *et al.*, 1998). They may be smaller at higher altitudes in the stratosphere. Retrieved column abundances from CIRS nadir-viewing spectra of Jupiter indicate a meridional variation of stratospheric C_2H_6 that is relatively flat, whereas the abundance of C_2H_2 decreases from the equator toward both poles (Nixon *et al.*, 2004). The latter variation makes sense, given the relatively short photochemical time constant of C_2H_2. The flat distribution of C_2H_6 suggests that stratospheric mixing is strong enough that the turnover time is less than the photochemical time scale. The trend for more sluggish motions and longer turnover times on Saturn (Conrath *et al.*, 1998) suggests that C_2H_6 may exhibit stronger meridional variations there. CIRS will be able to determine this.

Condensates can be good indicators of vertical motions. Gierasch *et al.* (1986), analyzing Voyager IRIS data of Jupiter, found evidence of two cloud components. One of the components had optical depths that correlated well with the gaseous NH_3 abundance. The optical depths were also largest where temperatures in the upper troposphere were colder, indicating upward motions (see below). The subsequent spreading of aerosols after the Comet Shoemaker-Levy 9 impacts in Jupiter's southern hemisphere has been used to infer the magnitude of meridional transport in Jupiter's lower stratosphere (Friedson *et al.*, 1999). Although the SL-9 impact provided an unusual injection of aerosols within a narrow latitude band, convective storms have been known to erupt and spread at low latitudes on Saturn Beebe *et al.*, 1992; Barnet *et al.*, 1992). The sensitivity of CIRS spectra to aerosols and condensates should complement their sensitivity to temperatures and help determine the circulations associated with these phenomena.

2. *Temperature and aerosol distribution*. In terms of the mean residual meridional circulation, the heat equation is (Dunkerton, 1978, Andrews *et al.*, 1987):

$$\frac{\partial T}{\partial t} + \left(\frac{\mathrm{d}T_0}{\mathrm{d}z} + \frac{RT_0}{C_\mathrm{p} H} \right) w = \frac{J}{C_\mathrm{p}} \approx \frac{T_\mathrm{e} - T}{\tau_\mathrm{r}} \tag{2}$$

where R and T have been defined for Equation (1), z is a vertical coordinate, C_P is the specific heat at constant pressure, H is a mean scale height, $T_0(z)$ is the horizontally averaged temperature profile, w is the vertical velocity, and J is the net radiative heating and cooling rate. The right-most term is a simplified parameterication of the radiative term in terms of a radiative equilibrium temperature T_e and relaxation time, τ_r. Equation (2) does not include the effects of heating associated with the lagged conversion between ortho- and para-H_2. These can be included (Conrath *et al.*, 1998), but they are less important in the stratosphere than in the upper troposphere, where temperatures are colder and the energy release larger. Equation (2) indicates that detailed measurements of the temperature field can serve as a good diagnostic of vertical motions. The mean temperature profile, T_0, is well known, and estimates can be made of the radiative heating/cooling. These can be simple parameterizations in terms of τ_r,

which can be readily calculated if the infrared absorbers are known (Gierasch and Goody, 1969; Conrath *et al.*, 1998), or more detailed calculations can be made, using detailed radiative-transfer calculations and measurements of aerosol heating and cooling at infrared, visible, and ultraviolet wavelengths.

Often the heat Equation (2) takes a particularly simple form. For instance if one studies the latitude variation in temperature at the tropopause on the scale of the zonal winds, one can assume $\partial/\partial t = 0$ to first order, since the winds are usually fairly steady. Then the balance in (2) is between the vertical advection term – representing adiabatic heating and cooling associated with vertical motions – and the radiative term on the left hand side. Near the tropopause, T_e is primarily due to infrared heating and cooling. Since temperatures in the upper troposphere are nearly uniform with latitude, as discussed earlier, the variation of T_e with latitude is small. Hence, vertical velocities tend to track temperature variations: colder temperatures indicate upwelling, warmer temperatures indicate subsidence (Conrath and Pirraglia, 1983). Saturn's stratosphere has a hemispheric seasonal variation in temperature. If one wishes to analyze circulations on this temporal and spatial scale, then the $\partial T/\partial t$ would be retained in (2).

3. *Potential vorticity (Ertel potential vorticity)*,

$$q \approx -g(2\Omega \sin \Lambda + \widehat{\mathbf{z}} \cdot \nabla \times \mathbf{u})\frac{\partial \theta}{\partial p} \tag{3}$$

is conserved for single-component fluids when forcing and dissipation are relatively weak. The quantity θ is the potential temperature: $\theta = \text{constant} \times T p^{-\frac{R}{C_P}}$, g is the magnitude of the gravitational acceleration, and $\mathbf{u}$ is the (two-dimensional) horizontal velocity. In hydrogen atmospheres, the presence of ortho- and para- forms with lagged conversion means that there is a two-component fluid, varying spatially, and hence q is not strictly conserved (Gierasch *et al.*, 2003). This conservation-breaking is probably less important in Saturn's upper stratosphere. The attractive feature of (3) is that q can be computed solely from the temperature field, provided $\mathbf{u}$ is known at some reference level. In terrestrial studies, the potential vorticity has proven to be a very useful tracer of atmospheric motions and dynamical processes. An example is the interaction of air masses within the circumpolar vortices with those at low latitudes (Hoskins *et al.*, 1985; Andrews *et al.*, 1987). The polar vortices are marked by sharp gradients in q across their boundaries, and the distortion of the contours of constant q from quasi-circles about the pole can indicate stirring and ultimately irreversible mixing of low- and high-latitude air masses. Such vortices can be expected on the giant planets. Ground-based infrared observations of have identified a cold region in Jupiter's arctic region that is likely associated with a strong circumpolar vortex (Orton *et al.*, 2002). Similarly on Saturn, one may anticipate nearly discontinuous changes in q across analogous features, including the ribbon feature

and the polar hexagon mentioned below, and the detailed morphology of q may be indicative of fluid material transport across these features.

Waves, eddies, and compact vortices. Voyager images of Saturn at visible wavelengths provided several examples of large-scale wave motion at mid and high latitudes, including the so-called 'ribbon wave' at around 40°N (Smith *et al.*, 1982; Sromovsky *et al.*, 1983) and the 'polar hexagon' at around 70°N (Godfrey, 1988, 1990). These wave-like flows appear to be unique to Saturn, and may represent a form of zonally propagating Rossby wave in a "waveguide" produced by the zonal mean flow itself. From sequences of Voyager images, Sromovsky *et al.* (1983) showed that the "ribbon wave" feature appeared to satisfy a dispersion relation that was roughly compatible with that expected for Rossby waves. Observations of the "polar hexagon" from Voyager were limited to a single set of images, revealing a remarkably symmetric pattern centered on a westerly jet at ∼70°N with near-perfect six-fold symmetry about Saturn's rotation axis. The hexagon appears to be associated with an adjacent compact, anticyclonic oval just south of it (Godfrey, 1988, 1990; Allison *et al.*, 1990), and both have persisted and appear in later Hubble Space Telescope and ground-based observations (Caldwell *et al.*, 1993; Sánchez-Lavega, 1993). Some support for this linkage comes from recent Hubble observations of Saturn's south polar region, which show neither a hexagon nor an anticyclonic oval, although there is a moderately strong circumpolar jet (Sánchez-Lavega *et al.*, 2002).However, much remains unclear about the origin and vertical structure of the ribbon and hexagonal waves.

The evidence for Rossby waves in Saturn's atmosphere was reinforced by the detection of wave structure in the temperature field by Achterberg and Flasar (1996). They identified a planetary wavenumber-2 (i.e., two wavelengths around a latitude circle) feature in upper-tropospheric temperatures retrieved from Voyager IRIS spectra. The feature extended from 40°N to equatorial latitudes with nearly constant zonal phase. Achterberg and Flasar determined that the feature was quasi-stationary with respect to Saturn's interior rotation, and they concluded the wave properties were most consistent with Rossby-wave propagation. They suggested that the wave might be a meridionally trapped wave forced by a "critical-layer instability" at midlatitudes, where the (zero) zonal phase velocity of the wave matches the null in the latitude profile of the zonal wind.

A problem that has existed for previous studies is the absence of planetary data sets with adequate horizontal and vertical coverage. CIRS is well equipped to provide this in a 4-year mapping mission, with its vertical coverage from both limb- and nadir-sounding. This is important, as waves are more easily identified when both horizontal and vertical wavelengths can be determined, as well as the horizontal tilts of the constant phase surfaces with altitude. These, together with phase velocities determined from time-lapsed observations, provide a probe of the propagation characteristics of the waves. It is logical to search for waves in the temperature field, but wave structure in gaseous constituent and aerosol distributions should also provide important diagnostics.

Although wave activity on Saturn is not yet adequately characterized, the momentum transports associated with such waves are likely to be important in maintaining the zonal winds. One candidate is the strong prograde equatorial jet that has been observed in Voyager images. The jet is approximately four times the width and strength of the analogous feature on Jupiter, and its strongly prograde motion implies a considerable excess of axial angular momentum. Winds derived from HST images obtained a few weeks after the onset of the major 1990 equatorial disturbance on Saturn indicated changes in the zonal mean winds and an enhancement in the zonal variance of the winds within the jet from those in the Voyager epoch (Barnet *et al.*, 1992). Similar images from 1996–2002 indicate that Saturn's equatorial jet has decreased to $\sim$200 m s^{-1}, one half its earlier value (Sanchez-Lavega *et al.*, 2003). An interesting question is whether this variability (and the onset of the 1990 "storm") could have resulted from changes in the interaction of the equatorial jet with upward-propagating equatorial planetary waves. This is an important source of cyclic variability in the Earth's stratosphere (the Quasi-Biennial Oscillation or QBO, e.g., Andrews *et al.*, 1987), where such oscillations have a characteristic signature in both the thermal structure of both the waves and zonal mean flow in the stratosphere. An analogous temporal oscillation in Jupiter's stratosphere has been reported (Orton *et al.*, 1991; Leovy *et al.*, 1991), with a period of around 4 years. As noted earlier, CIRS mapping during the Cassini swingby of Jupiter showed a high-speed equatorial jet centered in the upper stratosphere (Flasar *et al.*, 2004). Both the temporal oscillation and the spatial structure of the equatorial stratospheric zonal winds on Jupiter may be an atmospheric response to wave forcing. Temperatures retrieved from CIRS spectra will allow a systematic search for similar structure in Saturn's equatorial stratosphere.

Another important large-scale dynamical phenomenon observed in Saturn's atmosphere is the occurrence of long-lived, predominantly anticyclonic compact oval vortices. Such features were found at mid-latitudes on Saturn in Voyager images (Smith *et al.*, 1981, 1982), and appear to be the counterparts on Saturn of major long-lived vortices on Jupiter, such as the Great Red Spot and the White Ovals. On Jupiter, temperature measurements exhibited cold tropopauses over these features, indicating upwelling within the cores and subsidence in the surrounding environment (see, e.g., Flasar *et al.*, 1981b; Conrath *et al.*, 1981). Voyager, on the other hand, obtained little information on the thermal and vertical structure of Saturn's compact vortices. The possibility of obtaining near-simultaneous maps of temperatures and (from cloud-tracking) winds, allowing the computation of potential vorticity and maps of the concentrations of minor trace consituents in the vicinity of these features would provide information on the weak cross-isentropic Lagrangian circulation within these vortices. The latter could indicate the role and character of thermodynamic interactions with the buoyancy field within these vortices, and hence provide valuable insight into their origin and stability.

3.2. TITAN

Titan is Saturn's largest satellite. At 2575 km, its radius is nearly half Earth's. Since Comas Solá (1908) observed limb-darkening on Titan's disk, its atmosphere has attracted the interest of astronomers. CH_4 was the first constituent identified (Kuiper, 1944), from detection of its near-infrared bands. Further progress in characterizing Titan's atmosphere remained in abeyance for nearly 30 years, until ground-based narrow-band radiometric observations, and later high-precision spectrophotometric observations, began and identified several other hydrocarbons – ethane (C_2H_6), monodeuterated methane (CH_3D), ethylene (C_2H_4), and acetylene (C_2H_2) – from their emission features in the thermal infrared (Gillett *et al.*, 1973; Low and Rieke, 1974; Gillett, 1975; Tokunaga, 1980). A leap in the characterization of Titan's atmosphere occurred when the Voyager spacecraft flew through the Saturn system in 1980 and 1981. Molecular nitrogen (N_2) was determined to be the dominant atmospheric constituent, with CH_4 in second place at the few-percent level (Broadfoot *et al.*, 1981; Hanel *et al.*, 1981; Tyler *et al.*, 1981). IRIS also detected numerous organics in its range of sensitivity, below 300 km, expanding the list of hydrocarbons previously identified and adding several nitriles (Table IV). Titan thus has a mid-reducing atmosphere that resembles Earth's primordial atmosphere in several respects (Clarke and Ferris, 1997), albeit much colder. Being rich in organics – nitriles and hydrocarbons – it forms a natural laboratory to study prebiotic chemistry (Hunten *et al.*, 1984; Raulin and Owen, 2003).

Voyager provided the spatial resolution to characterize Titan's meteorology for the first time. It is a mix of that on Venus and Earth. Like Venus, Titan is a slow rotator, and it has a global cyclostrophic zonal wind system, with stratospheric winds corresponding to an angular velocity $\sim$10 times the surface rotation rate. However, its effective obliquity of 26° is much larger than Venus' and comparable to Earth's. Its stratospheric temperatures and winds should have large seasonal variations (Flasar *et al.*, 1981a; Flasar, 1998b). Titan also has a strong circumpolar vortex in the stratosphere, with condensed nitriles and enhanced hazes in the polar region. It may thus have an interaction of chemistry, condensation microphysics, and dynamical transport that is as complex as that in the terrestrial ozone hole in the Antarctic (Flasar, 1998a; Samuelson and Mayo, 1997). Finally, Titan likely has a "hydrological" cycle with cumulus convection, but involving CH_4, not H_2O (Awal and Lunine, 1994). There may be reservoirs of liquefied natural gas to drive the cycle, if not as global oceans, then as more localized lakes, perhaps subterranean (Lunine *et al.*, 1983; Dubouloz *et al.*, 1989). Voyager IRIS was a major player in elucidating the atmospheric composition and meteorology of Titan. CIRS is well equipped to extend this work substantively. Table V lists major scientific objectives for Titan, the physical variables that can be retrieved from CIRS spectra, and relevant measurement sequences, which are discussed in Section 4.3.

TABLE IV
Atmospheric composition of Titan.

Gas	Chemical formula	Mole fraction				Comments-Reference
Major components						
Nitrogen	N_2		0.85–0.98			Inferred indirectly[a]
Argon	Ar		<0.07			Inferred indirectly[b]
Methane	CH_4		0.005–0.034			In the stratosphere[b]
			0.03–0.085			Near the surface[b,1]
Hydrogen	H_2		0.0011–0.0013			b
			North Pole[d]			
Trace constituents		Equator[c]			Disk-average[e]	
		0.5–20 mbar	~ 0.1 mbar	~ 1.5 mbar	0.5–20 mbar	
Hydrocarbons						
Acetylene	C_2H_2	2.85×10^{-6}	4.7×10^{-6}	2.3×10^{-6}	5.5×10^{-6}	
Ethylene	C_2H_4	1.5×10^{-7}		3.0×10^{-6}	1.2×10^{-7}	
Ethane	C_2H_6	1.5×10^{-5}	1.5×10^{-5}	1.0×10^{-5}	2.0×10^{-5}	
Methylacetylene	C_3H_4	6.5×10^{-9}	6.2×10^{-8}	2.0×10^{-8}	1.2×10^{-8}	
Propane	C_3H_8	7.0×10^{-7}		5.0×10^{-7}	2.0×10^{-7}	
Diacetylene	C_4H_2	1.5×10^{-9}	4.2×10^{-8}	2.7×10^{-8}	2.0×10^{-9}	
Benzene	C_6H_6				4.0×10^{-10}	
Monodeuterated methane	CH_3D	1.1×10^{-5}			6.7×10^{-6}	
Nitriles						
Hydrogen cyanide	HCN	1.95×10^{-7}	2.3×10^{-6}	4.0×10^{-7}	3.0×10^{-7}	
Cyanoacetylene	HC_3N	$\leq 1 \times 10^{-9}$	2.5×10^{-7}	8.4×10^{-8}	5.0×10^{-10}	

Cyanogen	C_2N_2	$\leq 1 \times 10^{-9}$	1.6×10^{-8}	5.5×10^{-9}		
Acetonitrile	CH_3CN				1×10^{-8}	At 1 mbar[f]
Dicyanoacetylene	C_4N_2		Solid phase			[k]
Oxygen compounds						
Water vapor	H_2O				8×10^{-9}	At 0.01 mbar[g]
Carbon dioxide	CO_2	1.45×10^{-8}	$\leq 7 \times 10^{-9}$	$\leq 7 \times 10^{-9}$	2.0×10^{-8}	
Carbon monoxide	CO				$(2.2–4.2) \times 10^{-5}$	In the troposphere[h]
					$(2–3.9) \times 10^{-5}$; $(0.33–0.9) \times 10^{-5}$	In the lower and in the upper stratosphere[i]
					$4–6 \times 10^{-5}$	In the upper stratosphere[j]

[a]Lindal *et al.* (1983), Broadfoot *et al*. (1981).
[b]Lellouch *et al.* (1989), Courtin *et al.* (1995), Samuelson *et al.* (1997b).
[c]Unless otherwise indicated in the 7th column, all the results are from Coustenis and Bézard (1995).
[d]Unless otherwise indicated in the 7th column, all the results are from Coustenis *et al.* (1991).
[e]Unless otherwise indicated in the 7th column, all the results are from Coustenis *et al.* (2003).
[f]Marten *et al.* (2002).
[g]Coustenis *et al*. (1998).
[h]Lellouch *et al.* (2003).
[i]Hidayat *et al.* (1998).
[j]Gurwell and Muhleman (1995).
[k]Khanna *et al.* (1987).
[l]Lemmon *et al.* (2002).

TABLE V

Titan science and measurement objectives and observations.

Science objective	CIRS categories: Retrieved physical parameters	Observations
Formation and evolution		
Volatiles	CH_4	Mid-IR nadir maps, far-IR nadir integrations and limb scans
Isotopes	CH_3D, $^{13}CH_4$, $^{13}C^{12}CH_6$, $H^{13}CN$	Mid- and far-IR nadir and limb integrations
Atmospheric gas composition		
Photochemical cycle	Hydrocarbons (C_2H_2, C_2H_4, C_2H_6, C_3H_4, C_3H_8, C_4H_2,. . .) and nitriles (HCN, HC_3N, CH_3CN, C_2N_2. . .), including new species (CH_3, C_6H_6, $CH_2{=}C{=}CH_2$,. . .)	Mid-IR nadir maps and integrations, far-IR nadir integrations, mid- and far-IR limb integrations
Oxygen compounds	CO, H_2O, CO_2	Far-IR limb integrations (CO and H_2O), mid-IR limb and nadir maps (CO_2)
New species/ organics	H_2CO,. . .	Mid- and far-IR nadir and limb integrations
Aerosols and condensates		
Tropospheric clouds	CH_4,. . .	Far-IR nadir integrations and scans
Stratospheric condensates	C_4N_2, HC_3N,. . .	Mid- and far-IR limb integrations
Stratospheric aerosols	Far-IR haze properties	Mid-IR limb maps, far-IR limb scans
Atmospheric structure		
Temperature, pressure, density	Temperature field	Mid-IR nadir and limb maps, far-IR nadir and limb scans
Circulation		
Zonal winds	Thermal winds	Mid-IR nadir and limb maps, far-IR nadir and limb scans
Meridional motions	Constituent tracers	Mid-IR nadir and limb integrations, far-IR nadir and limb integrations
	Aerosols/diabatic heating and cooling	Mid-IR nadir and limb maps, far-IR nadir and limb scans
	Potential vorticity (temperature field)	Mid-IR nadir and limb maps, far-IR nadir and limb scans
Waves and eddies	Temperature and comp fields, variances	” ”
Surface		
Structure	Temperature	Far-IR nadir and limb scans

3.2.1. *Formation and Evolution*

Volatiles – Methane. Aside from argon, which only has an upper limit placed on its abundance, CH_4 is the most common atmospheric constituent after N_2 (Table IV), and a key question is why it is present to the degree observed. Photolytic and catalytic dissociation would deplete the atmospheric inventory of CH_4 in only 10 million years (Strobel, 1982). The logical source to replenish the atmospheric CH_4 is Titan's surface or its interior, but how this occurs is not known. If a surface reservoir, the liquid is not likely to be pure CH_4 (Flasar, 1983), but instead liquefied natural gas (CH_4, C_2H_6, C_3H_8, ..., N_2), with C_2H_6 as one of the major components (Lunine *et al.*, 1983; Dubouloz *et al.*, 1989). C_2H_6 and other hydrocarbons, produced by CH_4 dissociation in the upper atmosphere, end up at the surface by rainout after condensing in the lower stratosphere (Maguire *et al.*, 1981). Radar reflectivity studies (Muhleman *et al*, 1990), however, are not consistent with a global ocean of liquefied natural gas. In addition, near-infrared spectroscopy and imaging indicate bright and dark albedo features that are fixed in location, suggesting a mostly solid surface (Lemmon *et al.*, 1993; Smith *et al.*, 1996b; Combes *et al.*, 1997; Meier *et al.*, 2000; Coustenis *et al.*, 2001; Roe *et al.*, 2002; Gendron *et al.*, 2004). Recent spectroscopic studies have indicated that water ice is extensively exposed (Griffith *et al.*, 2003). An ocean basin-continent configuration similar to Earth's also poses difficulties. It would efficiently circularize Titan's orbit by tidal dissipation, which is inconsistent with the observed 3% orbital eccentricity (Sagan and Dermott, 1982; Sears, 1995; Dermott and Sagan, 1995). Hence, surface reservoirs are likely to be localized lakes or even stored in the regolith (Lunine, 1993). Lorenz *et al.* (1997) have suggested that the atmospheric CH_4 abundance is episodic, with periods of depletion and enhanced outgassing. Atmospheric CH_4 should vary spatially, not only from a possible heterogeneous source distribution, but also because it can condense in the troposphere. CIRS observations can determine the distribution of both tropospheric and stratospheric CH_4, thereby providing some clues to its source and also its transport in the atmosphere.

Information on the distribution of tropospheric CH_4 follows from an analysis of the collision-induced spectrum of CH_4 at 150–600 cm^{-1}, using temperature profiles independently retrieved from radio occultation soundings. The combined method works because the far-infrared spectra and the temperatures retrieved from the radio occultations depend differently on the vertical distribution of CH_4. The technique is fairly involved, and we refer the reader to Courtin *et al.* (1995), Samuelson *et al.* (1997b), and the review by Flasar (1998a) for details. Samuelson *et al.*, derived a CH_4 mole fraction near the equator $\approx$0.06, which decreased with latitude in both hemispheres, by a factor of 3 near 60°. They used Voyager IRIS spectra and the temperatures retrieved from Voyager radio occultation soundings. The latter were equatorial, so they had to assume that the general shape of the temperature profile at other latitudes remained similar to the low-latitude temperature profiles. Both Courtin *et al.* (1995) and Samuelson *et al.* (1997b) found that plausible opacities

from tropospheric gases and condensates were not sufficient to account for the observed spectral radiances, unless CH_4 was supersaturated by 50–100% in the middle and upper troposphere. Otherwise the brightness temperatures in the far-infrared portion of synthetic spectra would be too high compared to the observations, indicating that the emission level was too deep in the troposphere. However, the limited spatial coverage by IRIS and the existence of only one radio occultation sounding, with both ingress and egress were at equatorial latitudes, were a major impediment to these analyses. The mapping capability of CIRS, combined with several radio-occultation soundings by Cassini at different latitudes, will make this approach more viable.

Stratospheric CH_4 can be retrieved using CIRS spectra alone obtained with both nadir- and limb-viewing geometries. Figure 12 depicts the inversion kernels for temperature retrieval in Titan's atmosphere. These derive from the far-infrared portion of the spectrum in which pressure-induced absorption by N_2 dominates, and from the mid-infrared part of the spectrum near 1300 cm^{-1} in the ν_4 band of CH_4. The situation is similar to that discussed earlier for Saturn (Section 3.1.1). The partial overlap of the far-infrared inversion kernels in the limb-viewing mode and with those in the mid-infrared in the nadir-viewing mode allows the simultaneous

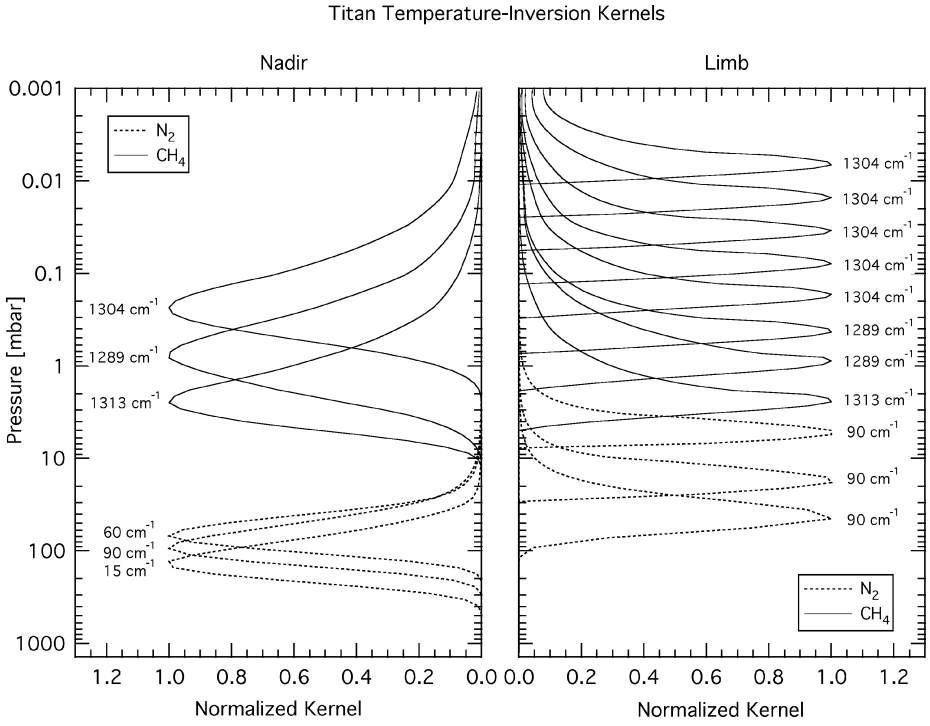

Figure 12. Inversion kernels for temperature sounding of Titan. The kernels for limb viewing have been convolved with a finite FOV have been convolved with a finite FOV approximated as a Gaussian, whose full width at the 1/e points, projected onto the horizon, equals one scale height.

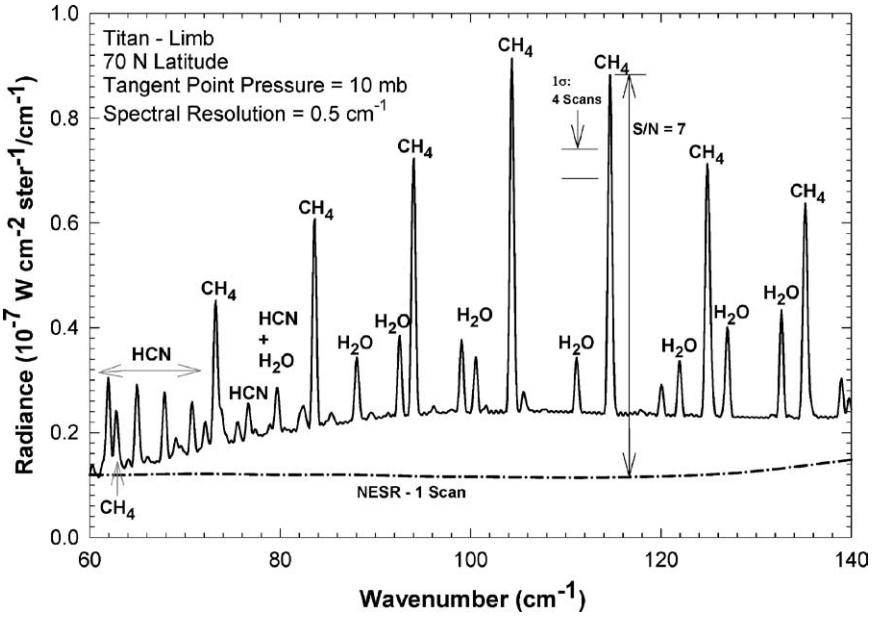

Figure 13. Synthetic far infrared limb spectrum between 60 and 140 cm^{-1} of Titan at 70°N, under conditions observed by Voyager near N. spring equinox. The limb-tangent height is the 10-mbar level. The spectrum contains the rotational lines of CH_4, HCN, and H_2O, seen in emission from the stratosphere, overlying the pressure-induced continuum of N_2. The NESR (Section 5.6.1) is shown for a single scan. The figure depicts the 1-σ error bar corresponding to an average of 4 scans, indicating the accuracy with which the CH_4 abundance can be retrieved.

retrieval of temperature and the mole fraction of gaseous CH_4 near 4 mbar. The retrieval is discussed in greater detail in Appendix A. An alternate method entails the use of the rotational lines of CH_4 in the far infrared at 60–140 cm^{-1}. Figure 13 illustrates this region of the spectrum viewed on Titan's limb, with a tangent point at the 10-mbar level. The optically thin rotational lines ride on the N_2 pressure-induced "continuum." Hence, temperature can be retrieved (as discussed in Section 3.2.4 and Appendix A) by using the radiances in the spectrum between the rotational lines, and temperature and CH_4 abundance can be retrieved unambiguously. To observe the narrow rotational lines, spaced $\sim$10 cm^{-1} apart, a moderately high resolution is needed. Figure 13 corresponds to the full apodized CIRS resolution (0.5 cm^{-1}). In Figure 14, the CH_4 emission probes the 10-mbar level; however, the lines will also be visible in nadir-viewing spectra, and those can probe CH_4 in this region down to 20 mbar.

An unambiguous retrieval of stratospheric CH_4 has never been done. Dynamical overturning times are short compared to the timescale for CH_4 dissociation (see Flasar, 1998a), and this would suggest that it is well mixed in the stratosphere. However, CH_4 condenses in the troposphere, and transport between the troposphere and stratosphere is poorly understood. The best fit of currently available data indicates

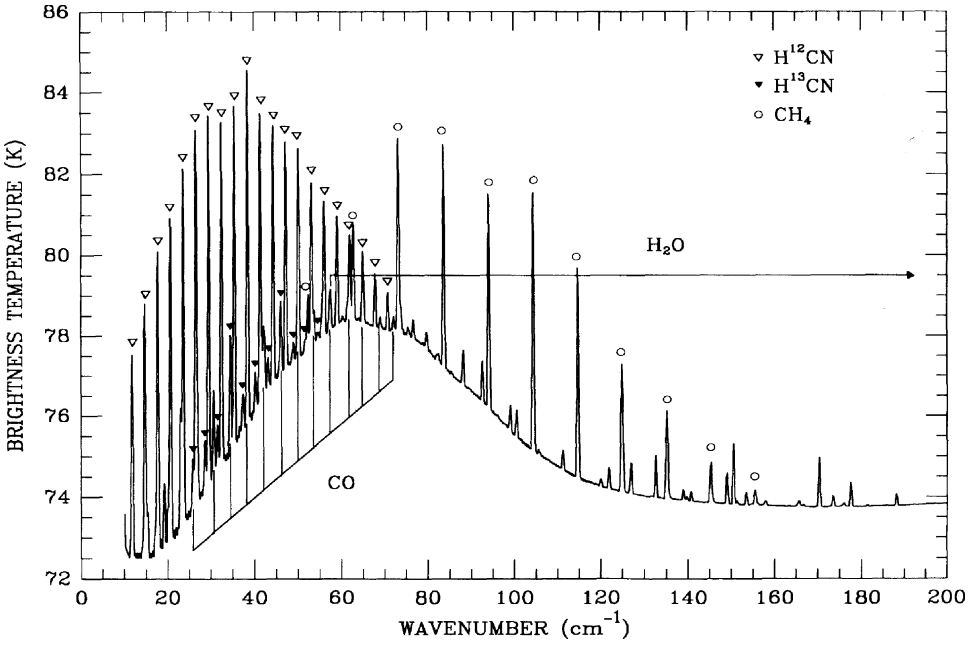

Figure 14. Synthetic nadir Titan spectrum at 10–200 cm^{-1}, with viewing at an emission angle of 48°. Brightness temperatures are depicted for clarity in viewing rotational lines of $H^{12}CN$, CO, CH_4, $H^{13}CN$, and H_2O (Coustenis *et al.*, 1993).

that the CH_4 mole fraction varies between 0.5 and 3.4% above the cold trap (Table IV), although recent studies tend to constrain this value even more (1.0–1.7%). Determining the vertical and horizontal distribution of CH_4 is critical for understanding several key atmospheric processes on Titan, and it is a major goal of CIRS measurements.

Isotopes. Other evidence in addition to CH_4 replenishment requires that the bulk of Titan's atmosphere must have outgassed from its interior. Had the atmosphere been captured directly from the gas in the solar nebula, one would expect twice as many neon atoms as N_2 molecules, which is not the case (Owen, 1982). Recent studies of carbon and nitrogen isotopes of HCN in Titan's atmosphere support this idea. From millimeter measurements, Hidayat *et al.* (1997) have shown that the ratio $[^{13}C]/[^{12}C]$ in HCN lies between 0.008 and 0.014 and equals the terrestrial-solar value within the uncertainties of the measurements. However, Marten *et al.* (1997) and Meier *et al.* (1997) have found that the ratio $^{15}N/^{14}N$ is greater than four times the terrestrial-solar value; more recently Marten *et al.* (2002) have found a ratio of 4.2. This fractionation implies a huge loss of nitrogen from Titan – 30 to 45 bars – much of which may have escaped from the satellite as a result of intense, early solar activity (Lunine *et al.*, 1999; Lammer *et al.*, 2000; Lammer and Bauer, 2003). If nitrogen has been escaping, carbon (and oxygen from CO) should have gone with it. The absence of a comparable fractionation of the carbon isotopes implies a large

reservoir of methane, or some other hydrocarbons, from which atmospheric CH_4 is continually replenished.

Rapid exchange of C between CH_4 and CO prevents enrichment of ^{13}C in CO as well (Wong *et al.*, 2002). Oxygen has been escaping, however, as demonstrated by the fact that $^{18}O/^{16}O \sim$ twice the terrestrial value in CO (Owen *et al.*, 1999a; Wong *et al.*, 2002). The lower enrichment for ^{18}O compared with ^{15}N is presumably the result of an influx of oxygen from the outside (see below).

The far infrared is fertile ground for probing the carbon isotopes of HCN. Figure 14 illustrates a nadir-viewing spectrum between 10 and 200 cm^{-1}. The far-infrared rotational lines are all optically thin, and they sit on the N_2 pressure-induced continuum emission from the lower stratosphere and upper troposphere. The differences in the amplitudes of the lines of $H^{12}CN$ and $H^{13}CN$ are strictly attributable to their relative abundances. The line-formation region for both isotopes is 10–20 mbar. Hence CIRS should be able to retrieve $[^{13}C]/[^{12}C]$ in the far infrared to a much higher accuracy than previously available. CIRS can also observe the ratio in the isotopic forms of CH_4 and C_2H_6 (Orton, 1992). As noted earlier for Saturn, the ability to observe ^{13}C in both parent (CH_4) and daughter (C_2H_6, HCN) molecules simultaneously may provide insight into any fractionation processes that have occurred.

The indirect evidence for a large internal reservoir to replenish atmospheric CH_4 suggests that the present ratio of atmospheric [D]/[H] should represent the value corresponding to the inventory of this reservoir, rather than a value determined by fractionation in the atmosphere itself. The abundance of atmospheric H_2 is too small to detect the rotational lines of HD in CIRS spectra, as can be done on Saturn. The same applies to H_2O and HDO (see below). However, the $[CH_3D]/[CH_4]$ ratio can be determined from the Q-branches of CH_3D and CH_4 near 1150 cm^{-1} and 1300 cm^{-1}, respectively. From Voyager IRIS data a value of $1.5^{+1.4}_{-0.5} \times 10^{-4}$ was found for [D]/[H] in CH_4 (Coustenis *et al.*, 1989b), recently revised from ISO/SWS disk-averaged spectra to something about 2 times less: $8.7^{+3.2}_{-1.9} \times 10^{-5}$ (Coustenis *et al.*, 2003). Mousis *et al.* (2002) argued that this value is representative of the [D]/[H] ratio in methane trapped in crystalline ice in the solar nebula at 10 AU. If correct, this would constrain the value of [D]/[H] in methane in the presolar cloud. The high sensitivity of the CIRS detectors in this region (Figure 37) will permit an improved determination of this ratio in CH_4.

3.2.2. *Atmospheric Composition*

Hydrocarbons and nitriles. Titan's atmosphere has an active photochemical cycle. Photolytic and catalytic dissociation of CH_4 in the upper atmosphere (mainly above 700 km altitude) lead to the formation of C_2H_6, C_2H_2, and higher-order hydrocarbons, including the polyacetylenes and organic oligomers thought to make up the brownish haze observed at visible wavelengths. The concomitant dissociation of N_2 by photolysis above 800 km and cosmic ray impact in the $\sim$100 km region leads to the production of nitriles, e.g., HCN, HC_3N, C_2N_2 (see, e.g., Lara *et al.*, 1996). Most of the hydrocarbons and nitriles condense (Maguire *et al.*, 1981) in

the lower stratosphere and tropopause region, where temperatures are coldest, as low as ~72 K, and precipitate to the surface. As noted earlier, this and the relative ease with which hydrogen, freed in the dissociation cycle, can escape from the atmosphere, ensures that the total inventory of atmospheric CH_4 is irreversibly lost in 10 million years in the absence of a source (Strobel, 1982).

The spatial distribution of the hydrocarbons and nitriles is a product of the coupling of photochemical processes and condensation with atmospheric transport. Voyager IRIS spectra indicated an enhancement of hydrocarbons (other than CH_4) and nitriles at high northern latitudes (Hanel *et al.*, 1981; Kunde *et al.*, 1981; Maguire *et al.*, 1981; Samuelson *et al.*, 1983; Coustenis *et al.*, 1991: Coustenis and Bézard, 1995). Figure 15 illustrates the relative prominence of emission from these species at these latitudes. Note that they are most distinct in the limb-viewing

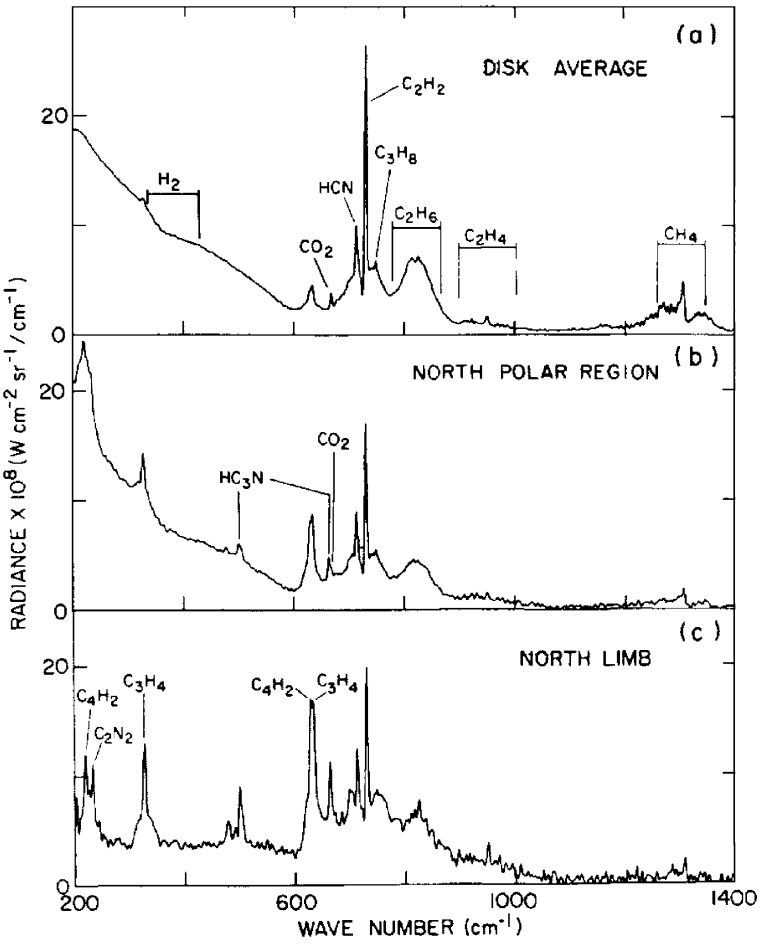

Figure 15. Voyager IRIS infrared spectrum of northern latitudes of Titan showing spectral emission features from hydrocarbons and nitriles.

spectrum, which is freer of the underlying continuum from the troposphere. For several of these (C_2H_4, C_3H_4, C_4H_2, HCN, HC_3N, and C_2N_2), the enhancement was a factor of 10 or greater (Coustenis *et al.*, 1991; Coustenis and Bézard, 1995). The temperatures retrieved at high northern latitudes are cold, suggesting strong circumpolar winds that may inhibit meridional transport between low and high latitudes (see below). Some information on the vertical profiles of the hydrocarbons and nitriles in the north polar region was available from the few IRIS limb spectra obtained, but these were fairly coarse, with 200-km altitude resolution. Several species, including all the aforementioned nitriles, showed a marked increase with altitude, at least in the region of sensitivity, $\sim$1 mbar to 0.1 mbar (Coustenis *et al.*, 1991). Although the ISO/SWS had higher sensitivity and spectral resolution than IRIS (0.3–0.8 cm^{-1}, comparable to that of CIRS), and detected new molecules, such as H_2O (Coustenis *et al.*, 1998) and – tentatively – benzene (C_6H_6; Coustenis *et al.*, 2003), it was only capable of obtaining disk-average Titan spectra. As a consequence, it missed two of the nitriles that IRIS had detected (C_2N_2, and C_4N_2). Adequate spatial resolution is key to studying these compounds.

The IRIS coverage of Titan was limited, and the vertical and horizontal distribution of the hydrocarbons and nitriles can be better retrieved from CIRS limb- and nadir-viewing spectra. Figure 16a shows a synthetic limb spectrum for a portion of the FP3 band pass at 3 cm^{-1} resolution. This spectrum was computed for conditions representative of the high northern latitudes (70°N) during the Voyager encounter. The strong emission features seen from the hydrocarbons C_2H_2, C_2H_6, C_2H_4, C_3H_4, C_3H_8, C_4H_2 and nitriles HCN and HC_3N will be used to determine vertical profiles of these gases. For example, Figure 17 illustrates the limb contribution functions for C_2H_2, C_2H_6, and HCN. These show good altitude coverage from 100–400 km. Adequate SNRs exist to map many of the strong species on the limb in 10 s time steps. Weaker features, such as C_2H_4 and C_3H_8, will require time averages of about 250 s (25 spectra). Although the nadir mapping will have somewhat lower vertical resolution and more limited vertical coverage, it will generally be executed further from Titan and therefore will provide more complete horizontal coverage (Section 4.3). Figure 16b shows a synthetic nadir spectrum for FP3 at 3 cm^{-1} spectral resolution, computed for conditions representative of Titan's equatorial region. The figure indicates that averaging over 16 scans (2.7 min) provides adequate SNR to determine the abundance of the weaker emission features, such as C_2H_4 and C_3H_8.

Oxygen compounds. The observed distribution of CO, CO_2, and H_2O bears on the question of whether oxygen in Titan's atmosphere has a primordial or external origin, or both.

Currently, there is some question on the spatial uniformity of CO in the troposphere and stratosphere (Table IV). A tropospheric value, $q = 6 \times 10^{-5}$, was inferred from spectra near 1.6 μm (Lutz *et al.*, 1983). Recent 5-μm spectra has indicated a tropospheric mole fraction $q = 3.2 \pm 1.0 \times 10^{-5}$ (Lellouch *et al.*, 2003). In the stratosphere, observations of the 115-GHz CO 1–0 rotational line by Marten *et al.* (1988) suggested a CO mole fraction, $q = 2^{+2}_{-1} \times 10^{-6}$. Later observations of

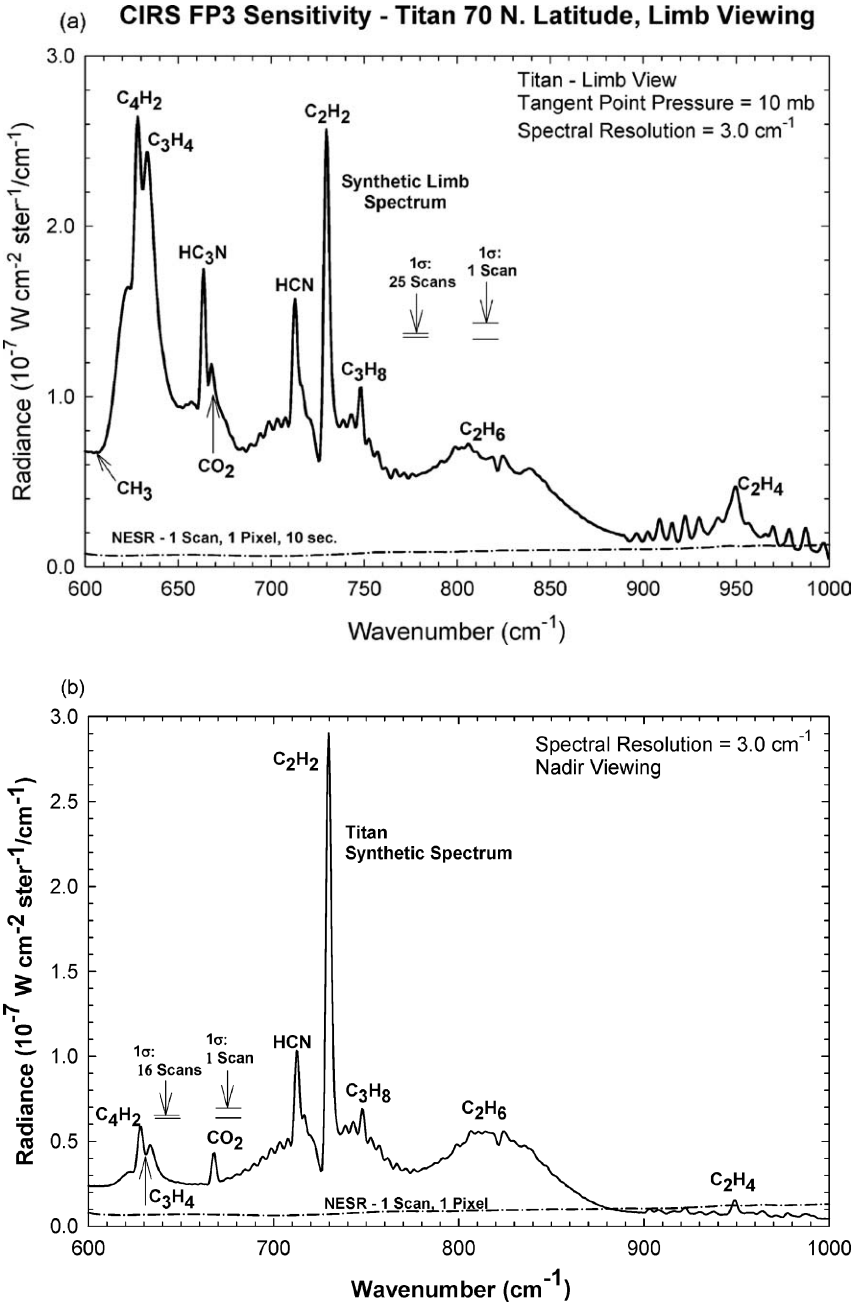

Figure 16. (a) Synthetic mid infrared spectrum (3.0 cm^{-1}) for FP3 for Titan limb viewing. The NESR is shown for a single FP3 pixel for a single-scan 10-s integration time. The 1-σ error bars are indicated for both 1 and 25 scans. (b) Synthetic mid infrared spectrum (3.0 cm^{-1}) for FP3 for Titan nadir viewing. The NESR for a single pixel and a single scan is indicated. The 1-σ error bars are shown for both 1 and 16 scans.

the 115 GHz line by Gurwell and Muhleman (1995) indicate a much higher stratospheric abundance, $q = 5 \pm 1 \times 10^{-5}$. Hidayat *et al.* (1998) used observations at 115 GHz and several other lines of ^{12}CO and ^{13}CO in the millimeter and submillimeter range, to retrieve a vertical profile of CO above the tropopause. They concluded that $q = 2.9^{+0.9}_{-0.5} \times 10^{-5}$ at 60-km altitude, decreasing to $q = 2.4 \pm 0.5 \times 10^{-5}$ at 175 km, and falling to $q = 4.8^{+3.8}_{-1.5} \times 10^{-6}$ at 350 km. The 60-km number is in agreement with Lellouch *et al.* but are smaller than those found by Gurwell and Muhleman, Lellouch *et al.* (2003) enphasize that with the observed influx of H_2O of 3×10^6 cm^{-2} s^{-1}, and a mixing ratio of 30 ppm, CO on Titan is not in

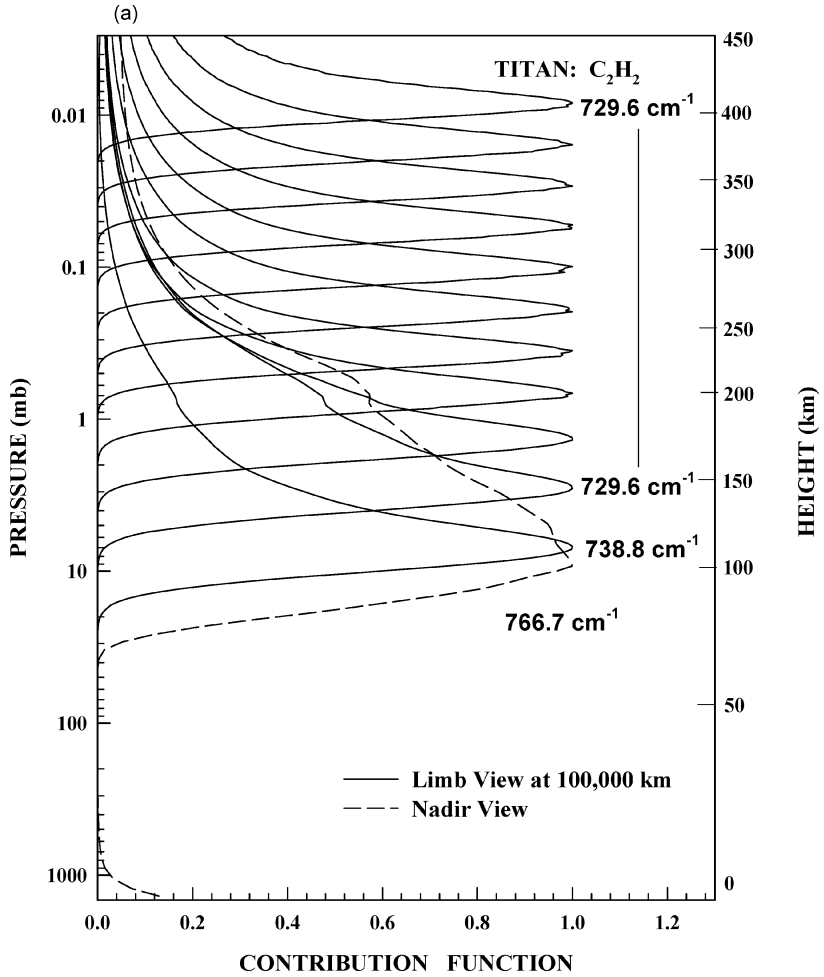

Figure 17. (a, b, c) Contribution functions for C_2H_2, C_2H_6 and HCN for limb and nadir viewing of Titan. The limb contribution functions have been convolved with a finite FOV whose full width projected onto the horizon equals one scale height.

(*Continued on next page*)

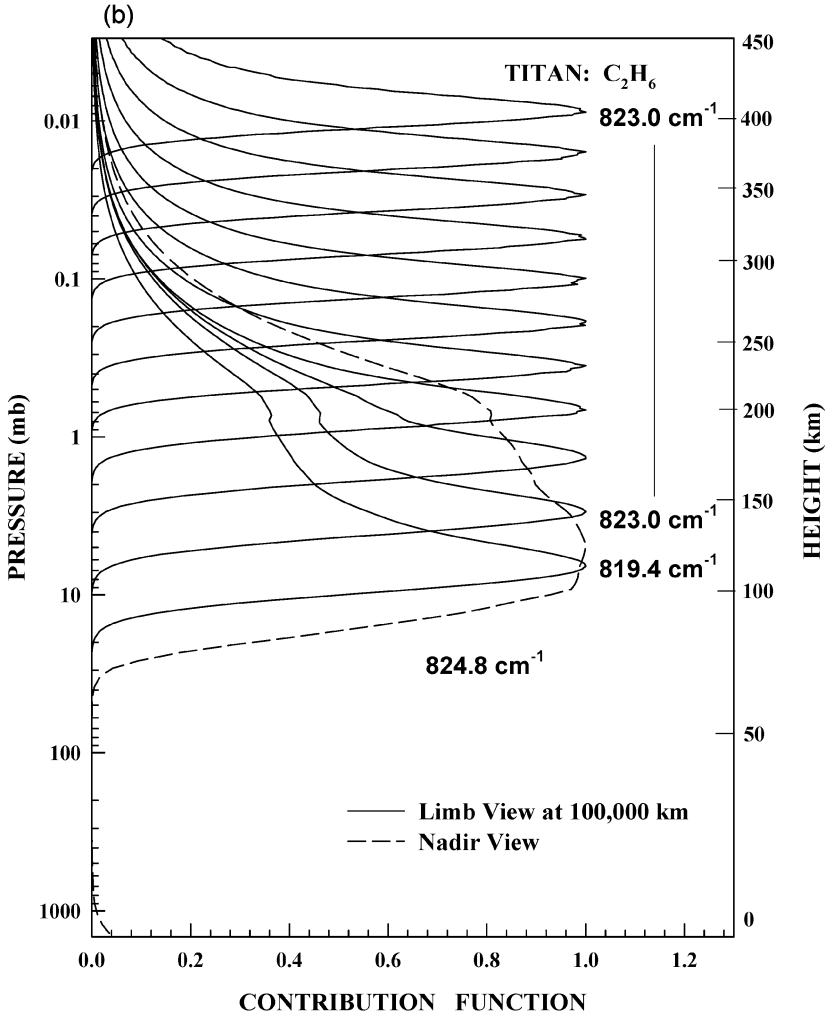

Figure 17. (*Continued*)

equilibrium and must experience continuous loss, reminiscent of CH_4. Replacement may come through cometary or interplanetary dust-particle impacts, or from internal sources. A depleted stratospheric abundance would suggest CO outgassing as the current source, although it would seem difficult to reconcile any nonuniformity with the fact that CO does not condense in Titan's atmosphere and dynamical overturning times that are much shorter than the timescales associated with photochemical destruction (Samuelson *et al.*, 1983). Alternatively, Samuelson *et al.* (1983) have suggested that the source of atmospheric CO is the influx of meteoric water that is photodissociated to form OH, which ultimately recombines with CO to form CO_2 and escaping hydrogen atoms. In their model, the observed abundance

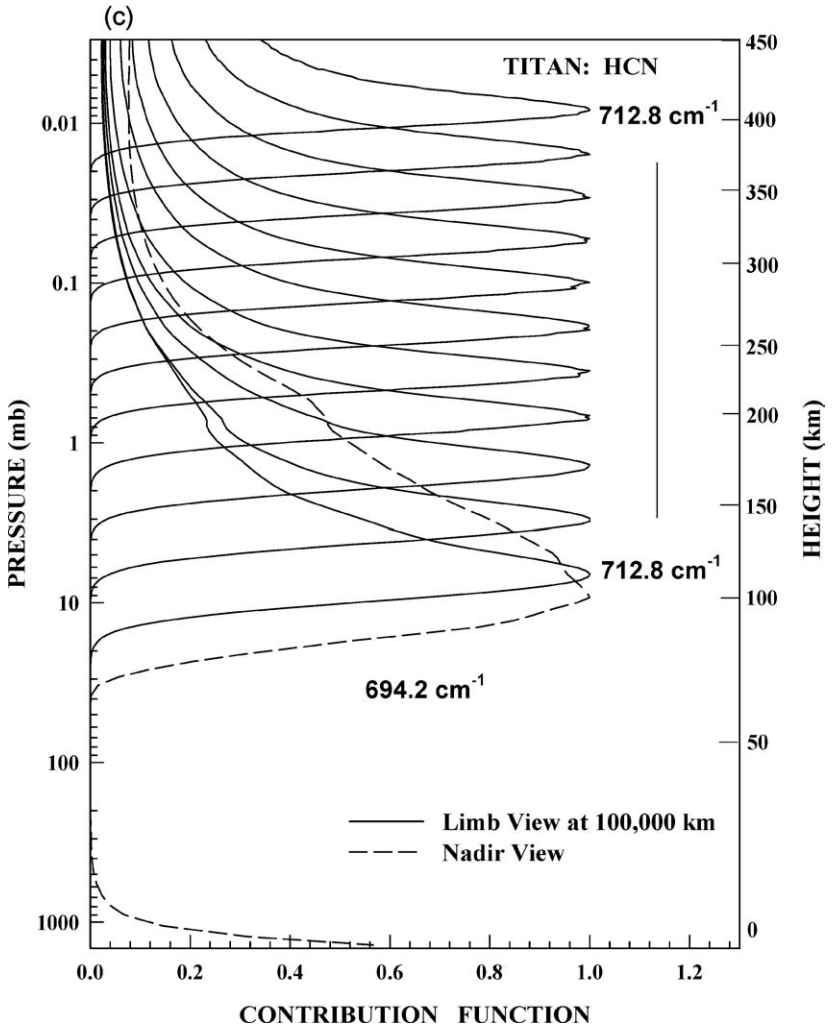

Figure 17. (*Continued*)

of CO_2 is regulated by condensation at the cold trap near the tropopause. Further progress in understanding the oxygen inventory of Titan requires better definition of the abundance and spatial distribution of the oxygen-bearing compounds in its atmosphere.

CIRS spectra in the far infrared can settle the issue of whether CO is depleted in the stratosphere. A synthetic limb spectrum for FP1 at 0.5 cm^{-1} spectral resolution, shown in Figure 18, illustrates the rotational line emission of CO. This spectrum was computed for a limb tangent height of 125 km ($\sim$3 mbar), assuming 24 parts per million CO. The solid line is with CO emission, and the dotted line is without.

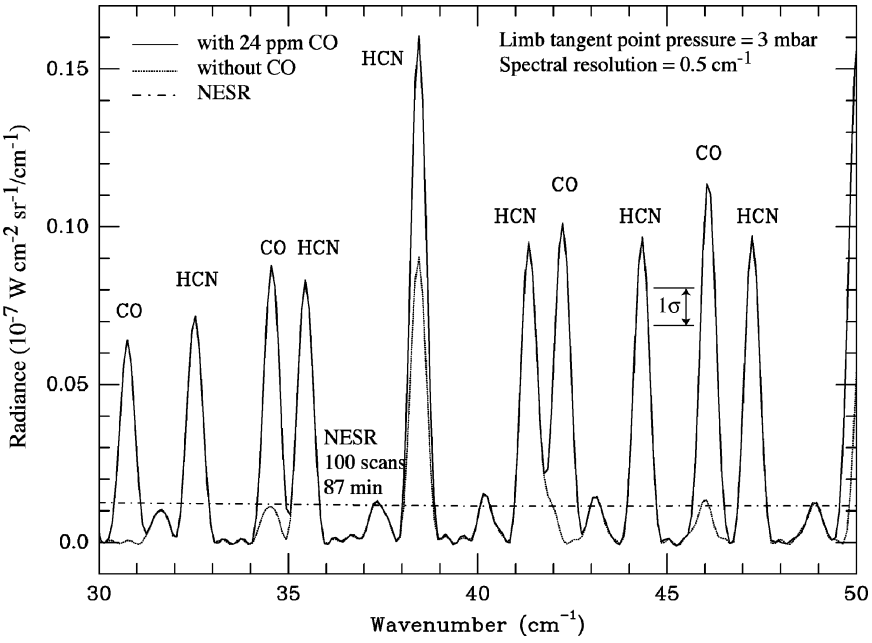

Figure 18. Synthetic far infrared spectrum (0.5 cm^{-1}) in FP1 for Titan limb viewing. The vertical profile of CO will be retrieved from the emission lines shown. Near 38.5 cm^{-1}, the CO and HCN emission are blended together, but all the emission lines can be used if both species are retrieved simultaneously.

The strongest relatively isolated CO lines are shown in the figure. The CO lines are intrinsically weak, and cannot be observed in an individual spectrum; an average of about 100 scans (87 min) at a specified altitude is needed to obtain the NESR and 1-σ error shown. Limb viewing in the far-infrared must be done relatively close to Titan, within two hours of closest approach, for adequate vertical resolution. With the limited time available for this, the CO abundance will not be globally mapped in the limb mode, but at several latitudes from pole to pole. Nadir integrations, performed at greater distances, offer better horizontal coverage, although no vertical structure will be retrieved, only a column abundance down to the lower stratosphere. Although the line-to-continuum ratio is smaller than for limb-viewing, a 90-min integration at 1.5–2 air masses is sufficient to detect the CO lines.

CO_2 was first detected in Voyager IRIS nadir-viewing spectra from emission in the ν_2 Q branch at 667 cm^{-1}, (Samuelson *et al.*, 1983). The line-formation region is centered near 10 mbar (Coustenis *et al.*, 1989a), but otherwise the nadir-viewing observations provided little information on the vertical distribution. Depending on the vertical distribution assumed, estimates of the average mole fraction in the stratosphere range from 1.5×10^{-9} to 1.4×10^{-8} (Samuelson *et al.*, 1983; Coustenis *et al.*, 1989a). A value slightly higher than this range (2×10^{-8}) was derived from ISO high-resolution measurements, in which the CO_2 contribution was separated

from HC_3N (Coustenis *et al.*, 2003; see also Table IV). This analysis assumed a stratospheric mixing ratio that was uniform with height. The IRIS spectra suggested that CO_2 was depleted in the north polar region (Coustenis *et al.*, 1991). However, the retrieval was complicated by the blending of the 667 cm^{-1} CO_2 emission with that from HC_3N, which was enhanced at high northern latitudes during the Voyager flybys. Because CO_2 is photochemically active and condenses near the tropopause (Samuelson *et al.*, 1983), it can vary both vertically and laterally. CIRS observations will better characterize the spatial distribution of CO_2. The vertical distribution of CO_2 can be determined from limb-viewing spectra. Figure 16a illustrates a spectrum characteristic of Titan's north polar region under Voyager conditions. The proximity of HC_3N and CO_2 emission is evident. However, with 25 spectra averaged at 3 cm^{-1} resolution (corresponding to a measurement time of 4.2 min), the SNR is adequate to separate the two features. Figure 16b illustrates that CO_2 can also be detected in a nadir-viewing average of 16 spectra over the same wavenumber range, under equatorial conditions.

Recent ISO/SWS observations in the grating mode have identified water vapor (Coustenis *et al.*, 1998). The distribution of H_2O can be determined from its rotational lines in the FP1 spectrum. ISO measured the emission at two rotational lines at 227.8 and 253.9 cm^{-1} to derive an H_2O mole fraction of 8×10^{-9} at the 400-km level in Titan's stratosphere. CIRS will use the stronger H_2O lines in the 80–160 cm^{-1} range; some of these are shown in Figure 19. These lines are

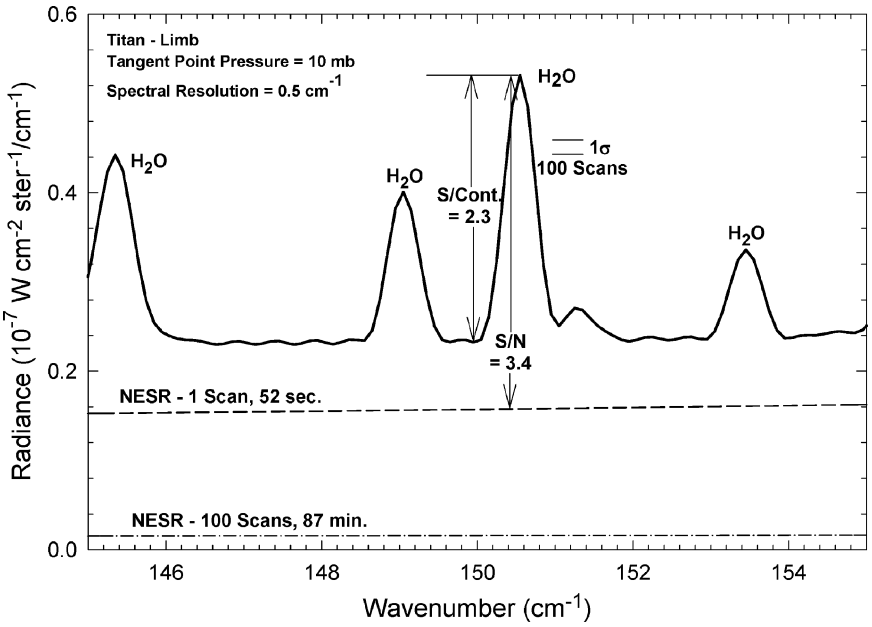

Figure 19. Synthetic mid infrared spectrum (0.5 cm^{-1}) for FP1 for Titan limb viewing. The vertical profile of H_2O will be retrieved from the H_2O emission lines.

relatively weak, and cannot be observed in an individual spectrum; an average of about 100 scans (87 min) is needed to achieve the NESR and 1-σ error bar shown in Figure 19.

New Species. With its unique combination of high spectral and spatial resolution, CIRS is uniquely qualified to search for compounds that were not detected in the Voyager or ISO spectra. Some of the more complex nitriles and hydrocarbons detected by Voyager, which had lower spectral resolution than ISO or CIRS, but better spatial resolution than ISO, were only found over a limited range of latitudes (the north polar region at the northern spring epoch of Voyager observations), and some were only seen at grazing incidence and high air mass.

For the possibility to detecting as yet unobserved molecules on Titan (Table VI) see the studies in Coustenis *et al.* (1993) and Coustenis *et al.* (2003). One important targeted species is the methyl radical, CH_3, discussed earlier for Saturn. This species has a strong emission band at 606 cm^{-1} (in FP3); its location is given in Figure 16a. Although methyl acetylene (CH_3C_2H) – propyne – has previously been observed on Titan (Table IV), the isomer allene ($CH_2{=}C{=}CH_2$) has not. Allene has emission bands at 353 cm^{-1} (in FP1) and 845 cm^{-1} (in FP3). The 353 cm^{-1} band is seven times weaker than the 845 cm^{-1} band, but it is more easily detectable because it is more isolated, whereas the latter is blended with ethane features.

Extrapolation of the data from laboratory simulation experiments to conditions on Titan suggests that several organic compounds unstable at room temperature can be formed only at the low temperatures of Titan's stratosphere. Laboratory experiments simulating the gas phase synthesis of organic compounds indicate that quite complex nitrogen-containing organics are produced in a N_2–CH_4 atmosphere. A few of the most abundant (yet undetected on Titan) are propionitrile, C_2H_5–CN, acrylonitrile, $CH_2{=}CH$–CN, cyanopropyne, CH_3–C=C–CN; also polynes such as $C_6H_2$and C_8H_2 and cyanopolynes, such as HC_5N (Thompson, *et al.*, 1991; de Vanssay *et al.*, 1995; Coll *et al.*, 1997). Other thermally unstable compounds such as CH_3NC, CH_2N_2 and CH_3N_2 should also be present in Titan's atmosphere. All these compounds have relatively strong signatures in the spectral ranges of the three CIRS focal planes, including at low temperatures (Cerceau *et al.*, 1985; Raulin *et al.*, 1990; Khlifi and Raulin, 1991, 1992; Delpech *et al.*, 1994; Nishio *et al.*, 1995; Shindo *et al.*, 2001a,b; Shindo, 2002) – see Table VI. Although some have IR bands interfering with those of other (known) constituents, the 0.5 cm^{-1} resolution of CIRS will permit their separation, and allow their detection or the establishment of upper limits. Detection of even one of these compounds and/or the determination of reduced upper limits would be extremely important to establish key pathways in the synthesis of prebiotic compounds.

CIRS can also search for new oxygen-bearing compounds, such as formaldehyde (CH_2O), or oxyrane (C_2H_4O), which is the most abundant o-organics produced in laboratory experiments simulating Titan's atmosphere chemistry (Coll *et al.*, 2003). The identification of these species can place constraints on evolutionary models of Titan and its atmosphere. Furthermore, CH_2O is a prebiotic organic, and its detection

TABLE VI

Some organics, as yet unobserved on Titan in the thermal IR, but potentially observable with CIRS and their deduced upper limits in Titan's atmosphere from previous observations.

	Strongest signatures		Upper limit of mean mixing ratio in Titan's stratosphere	
Studied compounds	Frequency (cm^{-1})	Band strength at 300 K (cm^{-2} atm^{-1})	using Voyager IRIS spectra	using ISO disk-average data
Hydrocarbons				
CH_2CCH_2	356	65	5×10^{-9}[a]	2×10^{-9}[b]
	845	407		
C_4H_4	629	288	7×10^{-10}[c]	
C_6H_2	622	428	4.4×10^{-10}[d]	
C_8H_2	621.5	496	4×10^{-10}[e]	
Nitriles				
CH_3CN	362[l]	4.4		
CH_2CHCN	230	10	8.4×10^{-8}[g]	$<5 \times 10^{-10}$[b]
	954	100		
CH_3CH_2CN	207	15	2.5×10^{-7}[a]	$< 1 \times 10^{-10}$[b]
	1075	37		
$CH_3CH_2CH_2CN$	728/742	3.5	5×10^{-7}[a]	
$(CH_3)_2CHCN$	538	3.3	2×10^{-7}[a]	
ΔCN	726	19	1.5×10^{-7}[a]	
	818	34		
CH_3CCCN	338	100	1.0×10^{-8}[a]	
	499	91		
$CH_3CHCHCN$	728	230	2.5×10^{-7}[a]	$< 5 \times 10^{-10}$[b]
CH_2CHCH_2CN	557	64	4×10^{-8}[h]	$< 5 \times 10^{-10}$[b]
	942	110		
$CH_2C(CH_3)CN$	535	33	7.5×10^{-8}[h]	$<5 \times 10^{-10}$[b]
	928	130		
C_4N_2	614	34.4	5.6×10^{-9}[i]	
NCCHCHCN (trans)	947	178	1×10^{-8}[j]	
Other N organics				
CH_3NC	526	8.8	1.3×10^{-9}[k]	
CH_2N_2	419	144	5.0×10^{-9}[k]	
CH_3N_3	250	9	5.4×10^{-9}[k]	

[a]Coustenis *et al*. (1993).
[b]Coustenis *et al*. (2003).
[c]Shindo *et al*. (2001a).
[d]Shindo *et al*. (2003).
[e]Shindo *et al*. (2001b).
[f]Nishio *et al*. (1995).
[g]Khlifi *et al*. (1999).
[h]Cerceau *et al*. (1985).
[i]Khlifi *et al*. (1997).
[j]Shindo (2002).
[k]Khlifi *et al*. (1996).
[l]Feature not yet observed. CH_3CN detected in millimeter observations (Bézard *et al.*, 1993; Marten *et al.*, 2002).

would suggest the importance of oxygen compounds and indicate new pathways in prebiotic chemistry on Titan.

3.2.3. *Particulates*

Aerosols. A brownish haze of aerosol particles dominates the visible appearance of Titan. These particles are thought to be organic refractories that consist of a complex mix of polyacetylenes, aromatic compounds, and amino acid precursors (McKay *et al.*, 2001). They are first formed in a photochemically active zone at an altitude of about 400 km, from where they are dispersed by gravity, diffusion, and planetary scale circulations. Initially the particles are roughly spherical monomers that grow one molecule at a time. Once they reach regions where the pressure exceeds 0.1 mbar they grow by coagulation into highly nonspherical aggregates (Cabane *et al.*, 1992; Tomasko *et al.*, 2002). These aggregates then become rapidly larger through cluster-cluster ballistic growth.

Vertical and horizontal distributions of haze particles depend strongly on the relative importance of the rates of atmospheric diffusion and circulation. Because meridional velocities are about three to four orders of magnitude smaller in the stratosphere than those associated with zonal winds (Flasar *et al.*, 1981a), variations of aerosol densities with latitude are likely to dominate along constant altitude surfaces. Rannou *et al.* (2002) have suggested that Titan's detached haze at ∼400 km is traced out by the meridional motion of small monomers that participate in a cross-equatorial Hadley cell circulation. The small size of the monomers precludes significant diffusive settling during a single season. However, the expected circulation pattern, moving from summer to winter hemisphere at high altitudes and returning at low altitudes, causes the monomers to descend rapidly in altitude at the winter pole. The attendant increase in ambient density associated with these monomers converts them into fractal aggregates that in turn settle relatively quickly when the circulation pattern reverses half a Titan year later, leaving a 50-km clear gap between the haze formed by these aggregates and the monomer haze higher up.

This circulation pattern also gives rise to an accumulation of haze at the winter pole, as suggested by Voyager 1 images (Smith *et al.*, 1981). In the absence of sources and sinks, a uniformly mixed atmosphere should give rise to a density scale height for an aerosol haze equal to that for the ambient atmosphere, provided only that the mixing rate is rapid compared with particle fall rates, a criterion that should be valid for Titan. When such sources and sinks are present, however, the relative scale heights will be different. In the case of Titan, the initial photochemical production zone near 400 km lies at a greater altitude than the aerosol sink; the latter is thought to be located in the lower stratosphere near 100 km where condensation of volatiles is expected. A subsequent precipitation of these condensates (hydrocarbons and nitriles) is expected to cleanse the atmosphere of aerosols below this level. Thus the aerosol scale height should exceed that of the gaseous atmosphere,

a characteristic found to be true for the north polar stratosphere at the time of the Voyager 1 encounter (Samuelson and Mayo, 1991).

Far-IR CIRS limb spectra covering the continuum between 250 cm^{-1} and 600 cm^{-1} will provide the vertical distribution of haze with a resolution of about two scale heights. From the work of Samuelson and Mayo (1991) this will determine the aerosol-to-gas scale height ratio to about 20%. Unlike the situation with Voyager IRIS, several limb locations can be sampled, permitting a determination of aerosol abundance with latitude. Measured vertical and latitudinal distributions of haze in turn can provide tests of seasonally-dependent dynamical models.

Condensates. The discussion in Sections 3.2.1 and 3.2.2 has already touched on the CH_4 cycle in Titan's atmosphere. Methane is transported from surface and/or subsurface reservoirs into the upper mesosphere and thermosphere, where it and molecular nitrogen are decomposed by solar EUV radiation and high energy electrons originating from Saturn's magnetosphere. The ensuing products are responsible for initiating the chemistry from which all the observed higher hydrocarbons (C_2H_2, C_2H_4, C_2H_6, C_3H_4, C_3H_8, C_4H_2) and nitriles (HCN, HC_3N, C_2N_2, C_4N_2, CH_3CN) are derived.

Atmospheric motions are also responsible for transporting these organic vapors down into the cold regions of the lower stratosphere where – almost without exception – their partial pressures exceed saturation vapor pressures (Maguire *et al.*, 1981). Whether or not they condense depends on the availability of condensation sites. Courtin *et al.* (1995) have suggested that aerosol particles may be immiscible in methane and ethane, making it unlikely that such particles can act as viable seed nuclei for at least some non-polar hydrocarbons. However, Titan aerosols may be slightly soluble in condensed nitriles (Raulin, 1987). In this case nitrile particles might in turn act as seed nuclei for hydrocarbons in the lower stratosphere. Condensate features of C_4N_2 at 478 cm^{-1} and possibly HC_3N at 503 cm^{-1} were found in Titan's north polar stratosphere by Voyager1 IRIS near the time of northern spring equinox. A C_4N_2 mean particle radius of about 5 μm was inferred from its band shape by Samuelson *et al.* (1997a). Other unidentified features at 225 cm^{-1}, 700 cm^{-1}, and 765 cm^{-1}, tentatively attributed to condensates, were also found (Coustenis *et al.*, 1999). At this time the north polar region was both relatively cold and contained relatively high abundances of several organic vapors, implying that the probability for condensate formation was especially high at this season and location.

Once formed, stratospheric ice particles will begin to precipitate. Their rates of precipitation depend on growth rates, which in turn are strong functions of the degrees of supersaturation prevailing at the time. Particles with radii of 5 μm will fall through the lower stratosphere in times short compared with a Titan season, and stratospheric clouds may be restricted to polar regions during late winter and early spring. Upon reaching the troposphere, precipitating ice particles can serve as nucleation sites for methane condensation. Thus high densities of stratospheric ice particles lead to low degrees of methane supersaturation in the troposphere. Because

particle growth rates are proportional to $S - 1$, the degree of supersaturation ($S = 1$ is saturation), it follows that stable clouds can form and persist only near saturation. If S is substantially greater than unity, any particles that form should grow rapidly and fall out immediately, leaving nothing to form a cloud (Toon *et al.*, 1988).

Still, there is some evidence from ground-based near-IR spectra and images for the presence of occasional tropospheric cloud activity (Griffith *et al.*, 1998, 2000; Roe *et al.*, 2002; Brown *et al.*, 2002). It will be very important to compare near-infrared VIMS and far-infrared CIRS Cassini spectra in an effort to correlate the presence of clouds in space and time with the appearance of condensate spectral features and degrees of methane supersaturation close to unity.

3.2.4. *Atmospheric Structure and Circulation*

Temperatures. Atmospheric temperatures on Titan have been most extensively determined below 200 km altitude (∼1 mbar). The vertical profiles of temperature retrieved from the Voyager radio occultation (Lindal *et al.*, 1983) indicate an atmosphere with a well defined tropopause and stratosphere, separated by a broad tropopause region (Figure 20). Radiative equilibrium studies (Yelle, 1991) suggest a mesosphere between 300 and 600 km altitude. To date, the only temperature retrievals in this region are from light curves that were obtained during the occultation

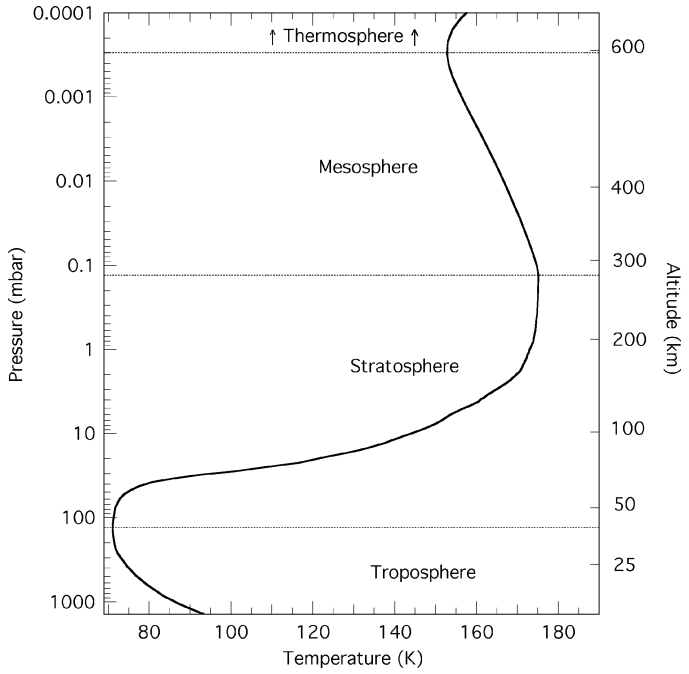

Figure 20. Representative Titan atmospheric temperature profile from the surface to 650 km altitude. The lowest 200 km is the nominal model derived by Lellouch *et al.* (1989) from Voyager radio-occultation and IRIS measurements. Above 200 km the profile is Yelle's (1991) model J.

of the bright K giant star 28 Sgr by Titan in 1989 (Hubbard *et al.*, 1993). These retrievals exhibit large variations that may be attributable more to uncertainties in the retrieval process itself than to spatial variability on Titan. As there was only one radio occultation with Voyager, with the ingress and egress located at equatorial latitudes, the horizontal variation in temperature below 200 km was determined mainly from IRIS spectra. IRIS generally acquired spectra in the nadir-viewing mode, and its coverage did not include the far-infrared portion corresponding to the N_2 inversion kernels in Figure 12. Hence, direct temperature retrieval was restricted to the range of the nadir-viewing CH_4 inversion kernels in the left panel of the figure: 0.3–3 mbar. Because of the limited sensitivity in this spectral region, the IRIS spectra of Titan were also spectrally averaged before the inversion, which effectively reduced the vertical resolution from that indicated in the figure (Flasar and Conrath, 1990). The unambiguous retrieval of temperature at other altitudes was impracticable, because aerosols, which vary heterogeneously, dominate the opacity in most of the IRIS spectra away from the ν_4 band of CH_4. Nonetheless, it was possible to use the brightness temperatures at 520–540 cm^{-1} and 200 cm^{-1} to infer the variation of temperature with latitude at the surface and in the tropopause region, respectively (Samuelson *et al.*, 1981; Flasar *et al.*, 1981a; Courtin and Kim, 2002). Figure 21 illustrates the derived meridional variation of atmospheric temperature at these altitudes. The latitude range of each point is 10–20°, and it is partially indicative of the spatial resolution of the IRIS FOV, but it also results from the need to bin and average spectra to achieve an acceptable noise error. The meridional profiles suggest that the polar regions are colder than the equator by ∼3 K at the surface and ∼20 K in the upper stratosphere (0.4 mbar). Longitude coverage was limited to two bands, one on the day side, the other separated by ∼180° on the night side (Flasar and Conrath, 1992). The ability to establish zonal variations was limited, but the available data suggested variations <1 K at the surface, and <3 K in the upper stratosphere (Flasar *et al.*, 1981a).

The repeated targeted flybys of Titan will enable CIRS to provide a much more complete latitude-longitude mapping of its temperature field (Section 4.3). Its far-infrared coverage allows the use of radiances where pressure-induced N_2 absorption dominates to retrieve atmospheric temperatures. It also can observe Titan's atmosphere in the limb-viewing mode. Hence, atmospheric temperatures can be retrieved from approximately the 400-mbar level up to the 10-μbar level (Figure 12), providing much more continuous coverage with high vertical resolution than previous observations. This will provide the first complete mapping of Titan's mesosphere. There is a gap in the lower troposphere, slightly larger than a scale height, over which CIRS spectra cannot be used for unambiguous temperature retrieval. Recourse will have to be made to temperatures retrieved from radio occultation soundings, and from the onboard probe temperature sensors over a single descent trajectory.

The atmospheric opacity is small at 520–540 cm^{-1}, and the radiances there are indicative of surface temperature (Samuelson *et al.*, 1981, 1997; Flasar *et al.*, 1981a; Courtin and Kim, 2002). Although the surface emission dominates, the

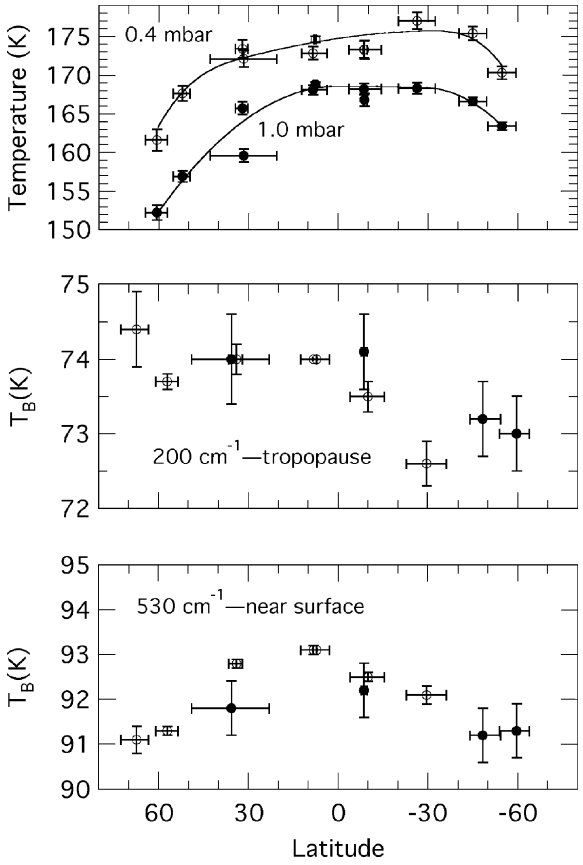

Figure 21. Top panel. Titan stratospheric temperatures retrieved from radiances at 1260–1307 cm^{-1} in the ν_4 band of CH_4. The vertical bars denote errors attributable to instrument noise; the horizontal bars give the range of latitudes of the binned and averaged spectra used in the inversions (Flasar and Conrath, 1990). *Lower panels.* Brightness temperatures renormalized to a constant emission angle at 200 cm^{-1} and 530 cm^{-1}, representative of tropopause and surface temperatures, respectively. In these panels solid points are at night, open circles are during the day. The vertical bars include uncertainties from noise, calibration, and emission angle corrections; the horizontal bars give the latitude range of the binned and averaged spectra (Flasar *et al.*, 1981a).

contribution from the warm stratosphere is not negligible (Figure 21; Samuelson *et al.*, 1981; Toon *et al.*, 1988). Samuelson *et al.* (1981) constructed a two-level model to account for possible effects of stratospheric hazes, using IRIS equatorial spectra obtained at near normal viewing (emission angle = 7°) and high emission angle (53°). The ability of CIRS to observe Titan's stratosphere on the limb, with deep space as the background, will enable one to separate the effects of stratospheric emission more cleanly from that of the surface.

Zonal winds. The equatorial pressure bulge implied by the meridional temperature gradients retrieved from Voyager IRIS spectra requires stratospheric zonal

winds with velocities up to 10 times the equatorial surface rotation velocity, or ∼100 m s^{-1}, to maintain the dynamical balance (see Equation (1)). Subsequent analysis of central-flash data from the 28 Sgr occultation in 1989 indicated an equatorial bulge in the isodensity contours that was consistent with zonal winds of comparable magnitude (Hubbard *et al.*, 1990; Sicardy *et al.*, 1990; Hubbard *et al.*, 1993). Thus Titan has a global cyclostrophic wind system analogous to Venus'. Titan's atmosphere exhibits a very interesting radiative-dynamical transition, in that the radiative response time in the troposphere is long compared to the seasonal modulation, whereas it is much shorter than the seasonal timescale in the upper stratosphere. Tropospheric temperatures therefore should exhibit little seasonal variation, but stratospheric temperatures should vary markedly (Flasar *et al.*, 1981a). As the zonal winds and temperature field are tightly coupled by the constraint of the thermal wind relation, the stratospheric winds should also vary seasonally. Observing this seasonal variation should provide clues to the maintenance of cyclostrophic wind systems, which is poorly understood. Venus, with its small obliquity, has little seasonal driving.

Detailed study of Titan's cyclostrophic zonal winds has been hampered by the lack of adequate spatial coverage and resolution, both horizontally and vertically, in the temperatures, as discussed above. The ability of CIRS to provide the needed temperature maps several times over the Cassini tour will go a long way toward rectifying this, but information from other experiments is needed. With cyclostrophic flows, the quadratic term dominates the left-hand side of the thermal wind Equation (1), and the direction of the zonal wind is ambiguous. If the temperature field is known down to the surface, where the winds are weak (from surface friction) and the linear geostrophic term dominates the left-hand side of (1), then the integration in principal can remove the ambiguity at higher altitudes where the cyclostrophic winds dominate. The radio-occultation soundings and the probe descent measurements should provide information on the temperature and pressure fields in the lower troposphere, but not the degree of mapping that CIRS can provide above the 400-mbar level. Direct measurements of the wind velocity will also be needed. The probe Doppler Wind Experiment (Bird *et al.*, 2002) will provide a valuable profile of the zonal wind along the descent trajectory. Tracking of discrete cloud or haze features, should they be discernible, by the imaging (ISS; Porco *et al.*, 2003) and near infrared mapping (VIMS; Brown *et al.*, 2003) experiments on the orbiter would also be useful.

Meridional Circulations. Gaseous and particulate tracers, the temperature field, and potential vorticity all probe residual meridional circulations, as they do for Saturn. Potential vorticity conservation does not have the complication of lagged ortho-para H_2 conversion, as on Saturn. Even though the flow is cyclostrophic, the Ertel potential vorticity is conserved on time scales over which dissipative and radiative effects can be neglected.

Deviations of the observed meridional variation of atmospheric temperature (Figure 21) from that expected from a purely radiative response have led to estimates of the heat transport by zonally symmetric meridional circulations. The derived

meridional velocities are quite sluggish by terrestrial standards, centimeters per second or smaller (Flasar *et al.*, 1981a; Flasar and Conrath, 1990; Flasar, 1998b). Stratospheric temperatures retrieved from the IRIS spectra indicated a cross-equatorial asymmetry of several degrees, that was not initially expected at the Voyager season (northern spring equinox), given the small radiative response time (Flasar and Conrath, 1990; Coustenis and Bézard, 1995). Flasar and Conrath (1990) suggested that the asymmetry resulted from the additional dynamical inertia caused by the seasonal cross-equatorial transport of angular momentum needed to maintain the thermal wind balance. The adiabatic heat and cooling associated with the vertical motion produces the hemispheric asymmetry in temperature. An asymmetric distribution of solar and infrared opacities (Bézard *et al.*, 1995) and the lag associated with the (albeit small) radiative time constant in a temperature field with a large seasonal amplitude (Hourdin *et al.*, 1995), have also been invoked to explain this asymmetry. Observing Titan at a different season than Voyager will help to differentiate among these models.

The distribution of photochemical species is a promising indicator of dynamical transport on Titan. An interesting example of this is the circumpolar vortex that was observed on Titan by the Voyager spacecraft in 1980–1981. Voyager 2 images showed a thin dark circumpolar ring at 70°N. Voyager IRIS spectra showed that high northern latitudes were enriched in several hydrocarbons and nitriles (Coustenis and Bézard, 1995). The IRIS spectra also indicated cold temperatures in the polar stratosphere (Figure 21) and, from the thermal wind Equation (1), a circumpolar vortex, with winds $\sim$80 m s^{-1} (Flasar and Conrath, 1990). The 28 Sgr occultation data, obtained during Titan northern summer, indicated winds double this at high southern latitudes, again implying a strong vortex about the winter pole. On Earth, circumpolar vortices are known to inhibit meridional flow across the vortex, where the vortical winds are strong (Schoeberl and Hartmann, 1991). The large meridional gradient in hydrocarbons and nitriles retrieved from the IRIS spectra at high latitudes is likely indicative of this barrier effect, coupled with the photochemistry. (Flasar (1998a) discusses several of these issues further.) To understand these complex systems, it is important to be able to map the three-dimensional structure of such vortices. With its ability to map temperatures and composition in both the nadir- and limb-viewing modes, CIRS can provide much of the critical information. CIRS's ability to map several different atmospheric variables simultaneously should also provide a better conceptual understanding of the variability of Titan's stratospheric hazes. Several models have been developed, and we have already discussed the study by Rannou *et al.* (2002) in Section 3.2.3.

Eddies and waves. The transports of heat and angular momentum by eddies and waves must be important players maintaining Titan's global wind system, but little is known about them, except inferentially. No direct sign of waves and eddies has been seen in visible images. The only evidence of thermal waves is from scintillations in the Voyager radio-occultation soundings that seem to be consistent with the signature of vertically propagating gravity waves in the tropopause region and the

stratosphere (Hinson and Tyler, 1983). Temperatures retrieved from IRIS soundings only placed crude upper limits to the variation of temperature with longitude – which, if detected, could have indicated the presence of waves or eddies – but these sampled longitude rather sparsely (Flasar and Conrath, 1992). The capability of CIRS to map both the vertical and horizontal variation of temperature – and of composition – with high sensitivity, will provide an effective probe of wave and eddy structure. CIRS should be capable of defining the phase tilts of any vertically propagating waves over its vertical range of retrieval (Figure 12), which should aid in their identification.

3.3. Icy Satellites

Cassini's orbital tour of the Saturn system includes multiple near and distant flybys of Saturn's satellites (Figure 22), permitting CIRS to address many of the basic goals for satellite investigations, including composition, temperature, thermal properties, and delineation of geologically distinct structures. CIRS will map the satellite surfaces and provide their thermophysical characteristics to understand the differences from satellite to satellite better. The long wavelength data from CIRS provide essential information on the surface and near-surface compositions of the airless satellites. CIRS can probe several millimeters into the regolith, where temperature gradients associated with possible solid-state greenhouse enhancements can be observed. The details of surface thermal, thermophysical and compositional characteristics will allow greater insight into the evolution of these objects. Particular attention will be paid to the unique aspects of Enceladus, where current endogenic activity may be revealed by surface thermal anomalies and by gases and particulate material in associated plumes. Joint investigations with VIMS will strengthen the determination of surface and near-surface compositions. CIRS data, combined with radiometry data from the RADAR experiment, will provide information on the porosity and scattering characteristics of the regoliths to depths of several centimeters. Overall, the extended spectral range of the CIRS instrument, combined with the 4-year orbital mission of the Cassini spacecraft and collaborative investigations, will provide a great increase in the quality and quantity of data returned on satellite surfaces compared to that obtained from the IRIS and other instruments on the Voyager spacecraft.

Saturn's airless icy satellites are intermediate in size between massive haze-shrouded Titan and the myriad small particles of the rings. These range from long-known Iapetus, Rhea, Dione and Tethys, discovered in the 17th century by Giovanni Cassini, to the small, irregularly shaped F-ring shepherds, Pandora and Prometheus, discovered in 20th century Voyager images by Collins *et al.* (1980). In this section we describe the capabilities of CIRS for investigating these objects.

The infrared energy available to CIRS from the icy satellites originates within a centimeter of the surface. Consequently, the instrument senses only satellite

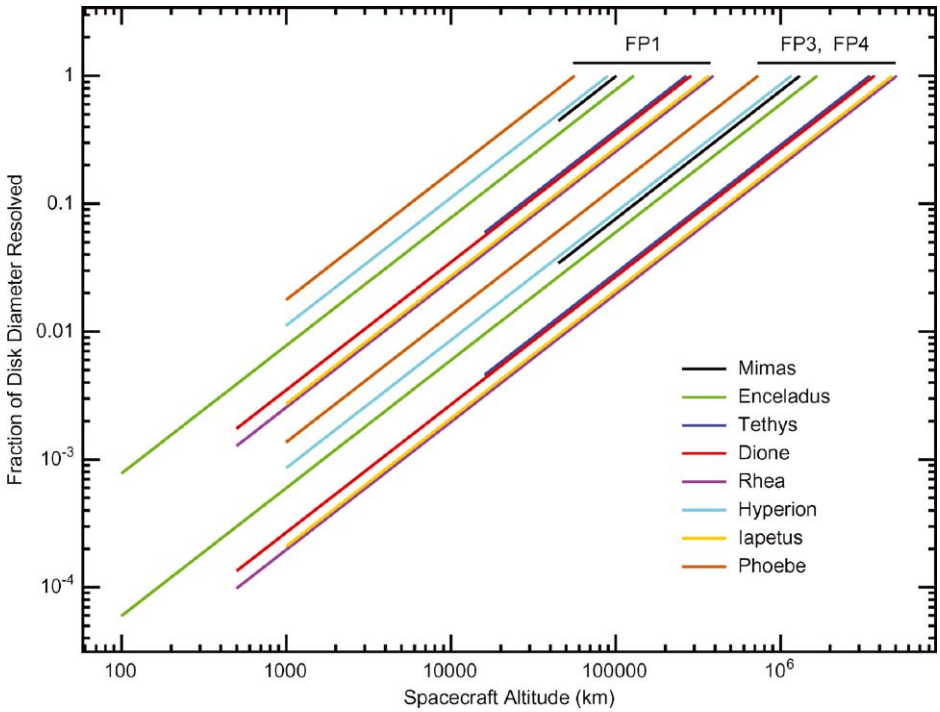

Figure 22. The spatial resolution of CIRS pixels projected onto the disks of various satellites as a function of altitude. The left ends of the curves are for the planned closest approaches during the tour. The right ends of the curves provide the altitudes at which the target objects just fill the pixel. The best Cassini encounters with all but Mimas (45,000 km) and Tethys (15,000 km) will be within 1,000 km of the surface (though for altitudes below ∼2000 km, the spacecraft cannot track the target, so that footprints will be smeared). A resolution of 10% of the disk diameter represents about 12 degrees of latitude at the sub-spacecraft point. The FP1 angular diameter (AD = 3.9 mrad) resolution can be compared with Voyager IRIS resolution (AD = 4.4 mrad), where the altitude for all encounters exceeded 70,000 km. At a given altitude, CIRS FP3 and FP4 resolution will exceed FP1 resolution by more than an order of magnitude.

regoliths or active surface sources. The information derived from such observations must then be related to the satellite interior and to its evolutionary history.

Evolutionary models that consider primordial composition, and heating and transport from accretional, gravitational (differentiation) and radioactive energy have been constructed in order to follow the development of the satellites (Ellsworth and Schubert, 1983; Schubert *et al.*, 1986). Except in the unlikely case that little of the accretional energy is lost during formation through radiation or through convection into the local nebula, the melting point of water would not have been reached. Thus, if the objects accreted as homogeneous ice-rock mixtures, they remained so. The possible presence of ammonia hydrate at the 20% level (Lewis,

1972) does not alter this conclusion, though melting of this fraction in the outer layers could have a profound effect on surface evolution, both through its influence on tectonics, and by providing a solvent for transport of subsurface salts.

Although one to two orders of magnitude less massive than poorly evolved Callisto, these saturnian satellites display considerable endogenic surface modification, both by tectonic and effusive processes. In many instances, two or more episodes of surface modification are recorded by the presence of extensive regions of vastly different crater ages. Superimposed on features from endogenic processes and major bombardment events will be modifications due to subsequent gardening by micrometeorites and implantation and alteration by magnetospheric interactions (e.g., Delitsky and Lane, 1998; Delitsky and Lane, 2002; Delitsky *et al.*, 2003).

Two groups of bodies can be recognized: the large icy satellites and the small, mostly irregularly-shaped objects.

The large icy satellites After Titan, the six largest satellites in the Saturn system are, in order of distance from Saturn: Mimas, Enceladus, Tethys, Dione, Rhea, and Iapetus. The first five can be considered regular satellites, having circular and prograde orbits lying very close to Saturn's equatorial plane with semi-major axes smaller than 10 saturnian radii. The sixth, Iapetus, moves at a larger distance (about 60 saturnian radii) on an orbit inclined 14.7°. The density of these satellites is only slightly greater than that of water, and all show the spectroscopic signature of water ice. Albedos have been determined from Voyager images (Buratti *et al.*, 1990; Cruikshank *et al.*, 1998).

Mimas ($r = 197 \pm 3$ km; $p_V = 0.8$) has an ancient, heavily cratered surface (r denotes radius, p_V visual geometric albedo). Herschel, the largest crater, is 130 km in diameter, and basically unmodified. However, evidence of limited surface modification early in Mimas' history is provided by small differences in crater counts. Brightness variations across its surface are small, with the leading side possibly a few percent brighter than the trailing side.

Enceladus ($r = 251 \pm 5$ km; $p_V = 1.0$) has the highest albedo among solar system objects, reflecting about 90% of incident sunlight. This, with a flat spectrum between 0.35 and 0.59 μm indicates that the surface ice is relatively uncontaminated and unmodified by radiation. The surface is characterized by at least four distinct terrains, ranging from heavily cratered to featureless plains (Smith *et al.*, 1982; Kargel and Pozio, 1996). Even in the cratered areas the crater size distribution indicates a relatively young crust. The maximum density of Saturn's E ring is at the radius of Enceladus' orbit and may be related to possible endogenic activity on the satellite, though other mechanisms have been proposed (Haff *et al.*, 1983; Pang *et al.*, 1984; Hamilton and Burns, 1994). Albedo variations are very small.

Tethys ($r = 530 \pm 10$ km; $p_V = 0.8$) is densely cratered. A plains unit, with relatively few small and intermediate sized craters, indicates a period of internal activity that produced partial resurfacing of older terrain early in the satellite's history. The satellite is strikingly marked by Ithaca Chasma, a deep trench that

spans nearly three quarters of its circumference. The leading hemisphere is 10–15% brighter than the trailing hemisphere.

Dione ($r = 560 \pm 5$ km; $p_V = 0.55$ – leading; $p_V = 0.4$ – trailing) is characterized by at least five terrains that differ in crater density (Plescia, 1983). Bright wispy terrain (linea) dominates the relatively dark trailing hemisphere. Ozone, the only material other than water ice so far identified on Saturn's icy satellites, is found on its surface (Noll *et al.*, 1997). It is believed to be the product of exposure to magnetospheric ion radiation.

Rhea ($r = 765 \pm 5$ km; $p_V = 0.65$ – leading; $p_V = 0.55$ – trailing), the most heavily cratered satellite of Saturn, is characterized by at least three different terrains. Like Dione, its trailing hemisphere is also marked by linea, and ozone has been identified as well.

Iapetus ($r = 718 \pm 18$ km; $p_V = 0.04$ – leading; $p_V = 0.5$ – trailing) is most notable for the extreme difference in albedo between its leading and trailing hemispheres. The leading hemisphere is covered with extremely dark material, while its trailing hemisphere is icy. Some bright-side craters have dark floors, suggesting flooding, but the dark hemisphere still needs explanation (Wilson and Sagan, 1995; 1996; Owen *et al.*, 2001; Buratti *et al.*, 2002). Comparison of the leading side with that of Phoebe indicates different compositions. The dark material is believed to be a complex organic solid (e.g., Bell *et al.*, 1985; Wilson and Sagan, 1995). Owen *et al*. (2001) found that the best match to the spectrum of the dark material over the range 0.3 to 3.8 μm is provided by a mixture of water ice, amorphous carbon, and a nitrogen-rich organic compound. The latter is required to fit the strong absorption found at 3.0 μm; water ice alone will not suffice. Non-biogenic nitrogen-rich organics are rare, leading to the suggestion that the dark material might have been formed on Titan and transported to Iapetus by impact. If so, the surface of Hyperion may be contaminated with the same material.

The presence of H_2O ice on the surfaces of the six larger satellites, the recent detection (Noll *et al*., 1997) of O_3 on Dione and Rhea, plus the presence of unidentified UV absorption on Iapetus, suggest that further close analysis of the spectra of Saturn's satellites may reveal additional species (see Cruikshank *et al*. (1998) for a complete review). Recent results on the Galilean satellites from the Galileo spacecraft's NIMS (Near Infrared Mapping Spectrometer; McCord *et al.*, 1997) seem to indicate the presence of materials containing CO_2, C-N, C-H, SO_2 and all the S-H bearing groups. It is extremely probable that similar kinds of materials, even if in very different proportions, will be found on the Saturn satellite surfaces. Recent studies of tholins have shown that the diagnostic region for organic materials extends far beyond the 5-μm region (see, e.g., Khare *et al.*, 1994; Colthup *et al.*, 1975), where CIRS can give fundamental information.

The small icy satellites. Eleven satellites belong to an inner group, of which several will be observed by CIRS. Encounter geometries during the Cassini tour are not favorable for CIRS to view the smallest of these, or the recently discovered

outer irregular satellites (Gladman *et al.*, 2001). However, the first satellite we encounter will be a distant, irregular one – Pheobe.

Phoebe ($r = 110 \pm 10$ km; $p_V = 0.06$) is small and dark. It possesses a retrograde orbit. The spectrum of its dark material differs from that of Iapetus and Hyperion. As a likely captured satellite, its dark component may be unrelated to that of the satellites that were formed *in situ* with Saturn. Pheobe's photometric characteristics and albedo identify it as a C-type object (Simonelli *et al.*, 1999). Recently, water ice has been detected on its surface by Owen *et al*. (1999b), by Brown (2000), and by de Bergh *et al.* (2003), supporting the hypothesis of a captured primitive body related to the Centaurs or the trans-Neptunians objects.

Hyperion ($164 \times 130 \times 107$ km; $p_V = 0.3$) The rotation of Hyperion is chaotic; its rotation period is therefore indeterminate, though at the time of the Voyager 2 encounter it was 0.5 days (Thomas *et al.*, 1995); it is certainly nonsynchronous. The satellite's highly irregular shape indicates an intense collisional history. The dark component of its surface is as yet unidentified, but it is similar to that of Iapetus at visual wavelengths.

Janus ($110 \times 95 \times 80$ km; $p_V = 0.6$) and *Epimetheus* ($70 \times 58 \times 50$ km; $p_V = 0.5$) are co-orbital satellites somewhat outside the F-ring. Unexpectedly low masses are believed due to unusually low densities (Yoder *et al.*, 1989; Nicholson *et al.*, 1992). No compositional information is available, but ice is suspected to be the major component of both bodies.

An overview of CIRS's capabilities for observing the icy satellites can be obtained from Figure 23. The NESR levels for the instrument are presented for the workhorse low spectral resolution mode that will be used for surface temperature observations (4.75 s scan time, 15.5 cm^{-1} spectral resolution). Also indicated are labels for the blackbody curves corresponding to the maximum temperatures expected on each of the primary satellites. Spatial resolution will be <10 km with FP1, and <0.3 km with FP3 and FP4 for close flybys (Figure 22), although the ultimate spatial resolution will be limited by the ability of the spacecraft to track the rapidly passing target. The improvements over Voyager IRIS in long wavelength coverage, and in the higher sensitivity and spatial resolution in the mid-infrared (600–1400 cm^{-1}) have already been discussed in Section 2. From 200 to 10 cm^{-1} (50 to 1000 μm), the absorption coefficient of water ice at 100 K decreases by over two orders of magnitude, making the material progressively more transparent. In this wavelength range, the unit optical depth in pure ice moves from a physical depth of $\sim$10 μm to $\sim$1 cm. These values are somewhat dependent on water ice structure and temperature (Warren, 1984; Hudgins *et al.*, 1993; Matzler, 1998).

To date, information on surface composition has come from ultraviolet, visible, and near infrared spectroscopy (Cruikshank *et al.*, 1998). Water ice has been identified on all eight classical icy satellites and Titan. As noted above, ozone produced from the interaction of surface ice with magnetospheric charged particle and ultraviolet radiation, has been discovered on Dione and Rhea (Noll *et al.*, 1997). The

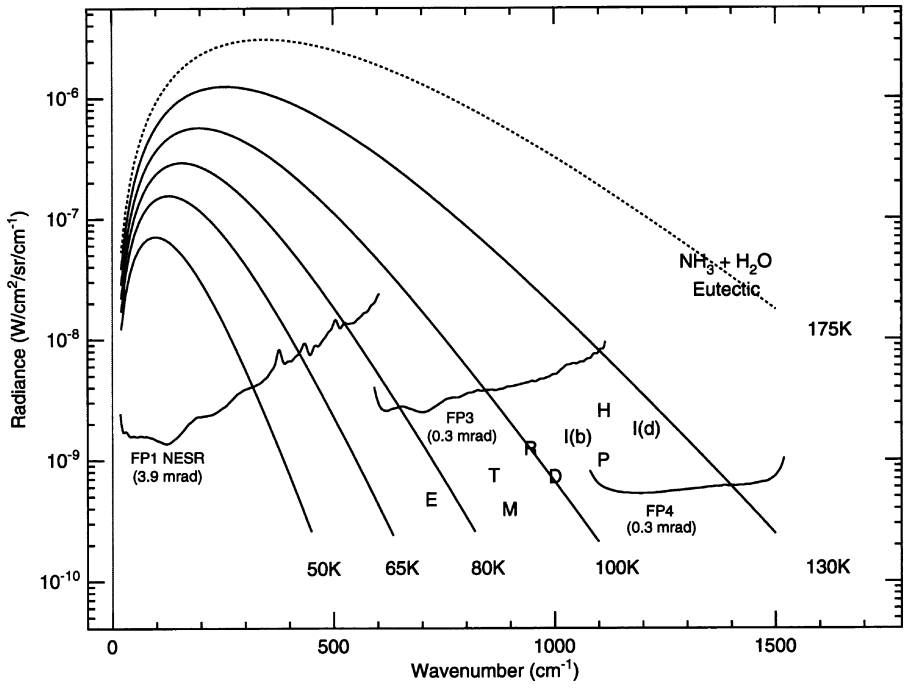

Figure 23. An overview of CIRS's capability for temperature sensing on the icy satellites. The irregular curves represent the NESR of the three CIRS focal planes (and their pixel sizes) for low spectral resolution short scans (15.5 cm^{-1}, 4.75 sec). Blackbody curves are shown for reference. Letter symbols in the lower center of the figure lie on blackbody curves corresponding to maximum expected surface temperatures for the icy satellites; all temperatures are calculated using a thermal inertia of 3×10^4 erg $cm^{-2}s^{-1/2}K^{-1}$. Temperatures are Mimas = M: 88 K; Enceladus = E: 73 K; Tethys = T: 91 K; Dione = D: 101 K; Rhea = R: 100 K; Hyperion = H: 118 K; Iapetus' (bright) = I(b): 109 K; Iapetus (dark) = I(d): 126 K; Phoebe = P: 112 K. The freezing temperature of a eutectic mixture of ammonia and water is approximately 175 K; in the event of current endogenic activity, material of this temperature might be observed.

visible spectrum of Phoebe is distinctly flatter than that of the dark side of Iapetus and of Hyperion; this puts to rest the hypothesis that the dark material on Iapetus results from the infall of dust from Phoebe (Cruikshank and Brown, 1982; Tholen and Zellner, 1983; Brown, 1983). Radar observations from Earth have revealed that the subsurface scattering properties of the bright hemisphere of Iapetus are remarkably similar to those of Titan, and very different from Ganymede, Europa and Callisto (S. Ostro, personal communication).

3.3.1. *Regolith Properties*

Information on Saturn's icy satellites from thermal infrared studies is limited (Cruikshank *et al.*, 1984). Early broadband observations were combined with photometric data to estimate satellite sizes and albedos for Rhea and Iapetus

(Murphy, *et al*, 1972; Morrison, 1974; Morrison *et al.*, 1975), and for Hyperion (Cruikshank, 1979; Cruikshank and Brown, 1982).

The most extensive thermal infrared data on these icy satellites were obtained by the Voyager IRIS experiment (Hanel *et al.*, 1981; Hanel *et al.*, 1982; see also the summary by Cruikshank *et al.*, 1984). Useful results were obtained for Enceladus, Tethys, Rhea and Iapetus. The large flyby distances and relatively large IRIS FOV (4.4 mrad) precluded useful measurements of other satellites, and restricted the above observations to full disk or modest spatial resolution.

Only Rhea was resolved at better than disk resolution, the footprint at best covering 25° of latitude. At a solar phase angle of 15° the brightness temperature near the subsolar point was observed to be 99 ± 2 K. A small correction for phase angle led to an estimate of 100 ± 2 K for the subsolar temperature.

The temperature distribution across the disk was measured at low and intermediate phase angles. At 15° phase, the central disk brightness temperature was observed as 99 ± 2 K with a gradual decrease to 93 ± 2 K at the limb. Seen at phase angle 77°, the variation was from 90 ± 4 K to 83 ± 4 K. This suggests that thermal emission is peaked in the backward direction, in a manner similar to that of the Moon. Such an effect has been ascribed to macroscopic roughness (Spencer, 1990; Hapke, 1996a). It therefore appears that the large and small scale roughnes of the Moon and of Rhea are similar, despite their different compositions and albedos; at Voyager resolution images suggest that this is also true on the topographic scale of a few kilometers (Smith *et al.*, 1981).

A disk observation of a solar eclipse of Rhea by Saturn was obtained. Relative to an observation made before eclipse entry, the pre-emergence flux dropped by roughly 75%, with a strong dependence on wavenumber (Figure 24). The nearly wavenumber-independent pre-eclipse brightness temperature of 96 ± 2 K

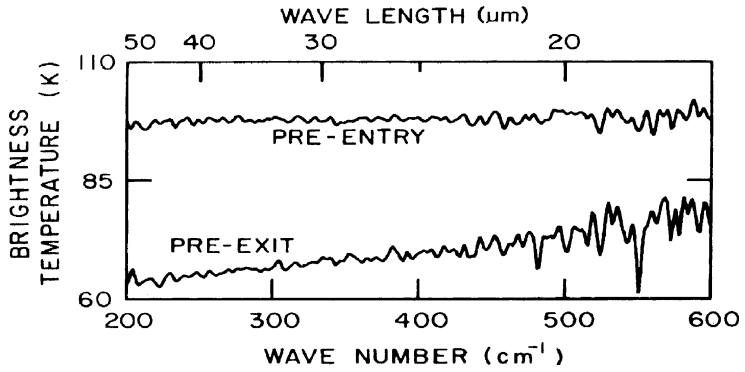

Figure 24. A solar eclipse of Rhea observed by Voyager IRIS. Before entry, the disk brightness temperature spectrum is nearly wavenumber independent; after roughly two hours in eclipse, the spectrum shows wavenumber dependent cooling, which indicates that materials with different thermal inertias are present (Hanel *et al.*, 1981).

is consistent with the spatially resolved measurements discussed above. By decomposing the spectrum in eclipse into two blackbody components, it is concluded that roughly half of the surface cools to ~75 K, while the remainder cools to <55 K. This indicates the presence of components having different thermal inertias: a high inertia fraction of solid material with block size equal to or greater than the thermal skin depth, and a low inertia fraction, possibly frosty or fine-grained.

Striking diurnal deviations from blackbody behavior were also seen by Voyager IRIS on the icy Galilean satellites of Jupiter (Spencer, 1987). Subsolar spectra on Callisto are close to blackbodies, but those taken near the terminator show a large increase in brightness temperature with increasing wavenumber, probably due to temperature contrasts caused by uneven illumination of rough topography. Ganymede is quite different: spectra show a small increase in brightness temperature with increasing wavenumber regardless of time of day, probably due to spatial segregation of surface materials.

Full disk measurements at modest phase angles were used to infer subsolar temperatures for Enceladus, Tethys and Iapetus. To adjust for phase angle, a model for the surface temperature distribution must be used. A simple model for a slowly rotating satellite is $T(\phi) = T_{ss} \cos^{1/n}(\phi)$, where T_{ss} and ϕ are the subsolar temperature and zenith angle of the sun, respectively. For a nonrotating Lambert sphere, $n = 4$; for the Moon, $n \approx 6$; a fit to the IRIS data for Rhea gives $n \approx 7$. Adopting the value derived for Rhea, disk measurements of Enceladus at phase angles between 36° and 39° indicate a subsolar point temperature of 75 ± 3 K (including a 1 K adjustment for thermal beaming), while measurements of Tethys at phase angles between 14° and 19° indicate $T_{ss} = 93 \pm 4$ K. Measurements of Iapetus from 48° and 80° were not corrected for the strong albedo variations across the satellite surface, and were only interpreted to indicate a temperature for the dark component in excess of 110 K.

From the derived subsolar temperatures, the bolometric Bond albedo, A, was estimated by using the equilibrium relation for absorbed solar and thermally emitted radiation for a Lambert surface with unit emissivity, on the assumption of instantaneous equilibrium with sunlight (i.e., no significant radiation of heat from the night side):

$$T_{ss}^4 = T_0^4(1 - A)/R^2, \tag{4}$$

where T_0 is the equilibrium temperature for a black surface at 1 AU, taken as 401 ± 6 K, and R is the distance to the sun in AU. The results: $A_{En} = 0.89 \pm 0.02$, $A_{Te} = 0.73 \pm 0.05$, and $A_{Rh} = 0.67 \pm 0.03$, can be compared with values obtained from analysis of Voyager images: $A_{En} = 0.9 \pm 0.1$, $A_{Te} = 0.60 \pm 0.1$, and $A_{Rh} = 0.45 \pm 0.1$ (Cruikshank *et al.*, 1984). The large discrepancies for Tethys and Rhea probably result from the fact that significant heat is radiated from the night-side of these bodies, invalidating the above equation. The good agreement for Enceladus is consistent with a very bright friable surface layer that cools rapidly at night, i.e., radiates little from the night side. This is also consistent with the high single

scattering albedo, low compaction factor, and large scattering asymmetry factor derived for Enceladus from Hapke analysis (Buratti, 1985).

Physical structure. CIRS will combine observations of eclipses, and measurements of diurnal (orbital) and annual temperature variations to establish the vertical and horizontal structure of surface thermal inertia. From these data and the assumption of an icy regolith, the vertical profile of surface thermal conductivity can be established.

The temporal response of a passively heated surface is related to the period, P, of the radiative forcing through the thermal skin depth, λ:

$$\lambda^2 = Pk/(\pi\rho c), \tag{5}$$

where k is thermal conductivity, ρ is density, and c is specific heat. Thermal skin depths are shown in Table VII for typical time scales and expected densities.

At wavenumbers greater than 200 cm^{-1}, thermal radiation observed by CIRS will be emitted only from the upper few microns of the surface. Qualitatively, the mean level of the diurnal cycle of surface temperature depends on albedo, while the amplitude is a measure of the thermal inertia, $\sqrt{(k\rho c)}$ (Figure 25). The spectrum of a satellite in eclipse (Hanel *et al.*, 1981; Figure 24) or at night will show significant deviations from blackbody behavior, principally due to differential cooling across a lateral distribution of materials having various thermal inertias. Spatially resolved measurements will enable these differences to be located and quantified. Remarkable spatial variations in thermal inertia have been mapped using nighttime temperatures on Mars (Mellon *et al.*, 2000), and on the icy Galilean satellites Europa (Spencer *et al.*, 1999), and Ganymede (Pappalardo *et al.*, 2004). On Europa, Galileo observations show striking and unexplained variations in thermal inertia with latitude and terrain type (Figure 26). On Ganymede, the temperature contrasts between bright and dark terrain reverse at night (dark terrain is warmer during the day, bright terrain is warmer at night), suggesting that the bright terrain contains more spatially-segregated, bright, high thermal inertia, ice than the dark terrain (Pappalardo *et al.*, 2004). On Earth's Moon, fresh craters are warmer at night than their surroundings due to the large abundance of high thermal inertia blocks on their rims (Saari and Shorthill, 1963).

TABLE VII

Thermal skin depths associated with several natural heating periods.

Cycle	Period	λ
Eclipse	~2 h	~0.2 cm
Diurnal	~2 days	~1 cm
Annual	30 years	~70 cm

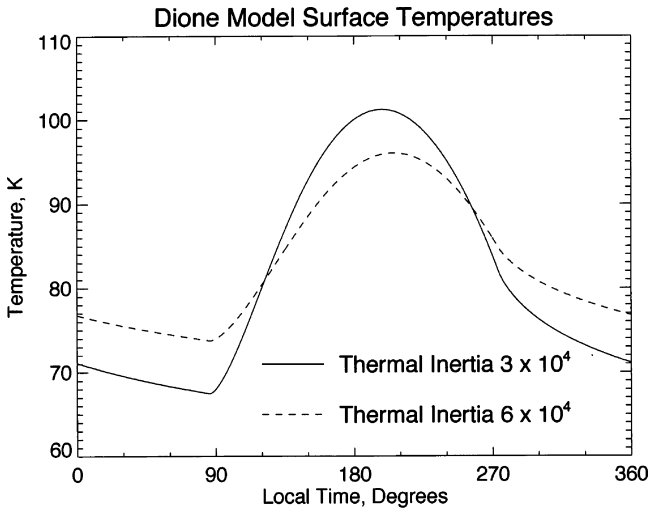

Figure 25. Example model diurnal temperatures for Dione at latitude 15 S, with the subsolar point also at 15 S. Two different but plausible thermal inertias are used to show the sensitivity of temperature to thermal inertia. Thermal inertia units are erg cm^{-2} $s^{-1/2}$ K^{-1}. A bolometric albedo of 0.47 is assumed.

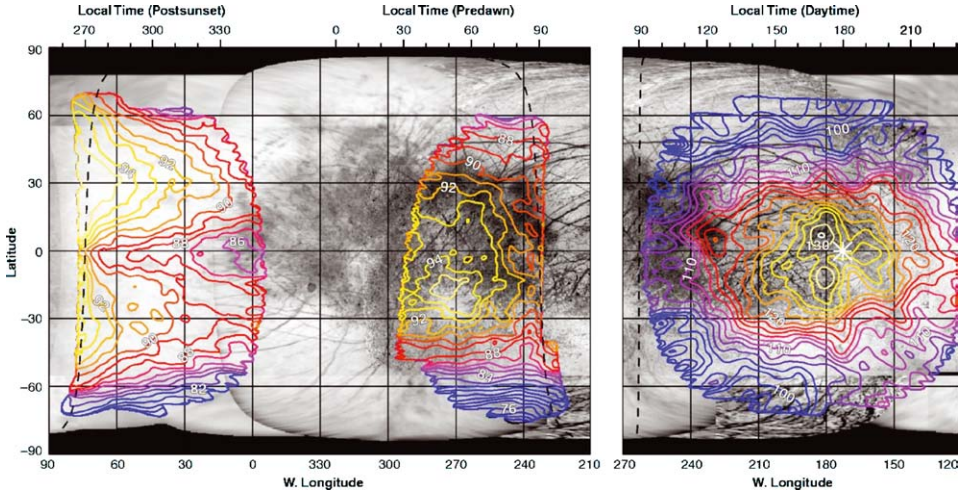

Figure 26. Contours of brightness temperature distributions on Europa. Contour interval is 1 K for the nighttime map, and 2 K for the daytime map; the color scheme is different for the two maps. Local time (top abscissa) is given in degrees of rotation past midnight. The terminator is shown by dashed black lines, and the subsolar point is indicated by a white star (Spencer *et al.*, 1999).

CIRS will obtain both full disk and spatially resolved measurements of the satellites Mimas through Phoebe (Figure 27). Observations of the dark winter north polar regions of Enceladus and Tethys will be obtained to determine the annual minimum temperatures in these regions.

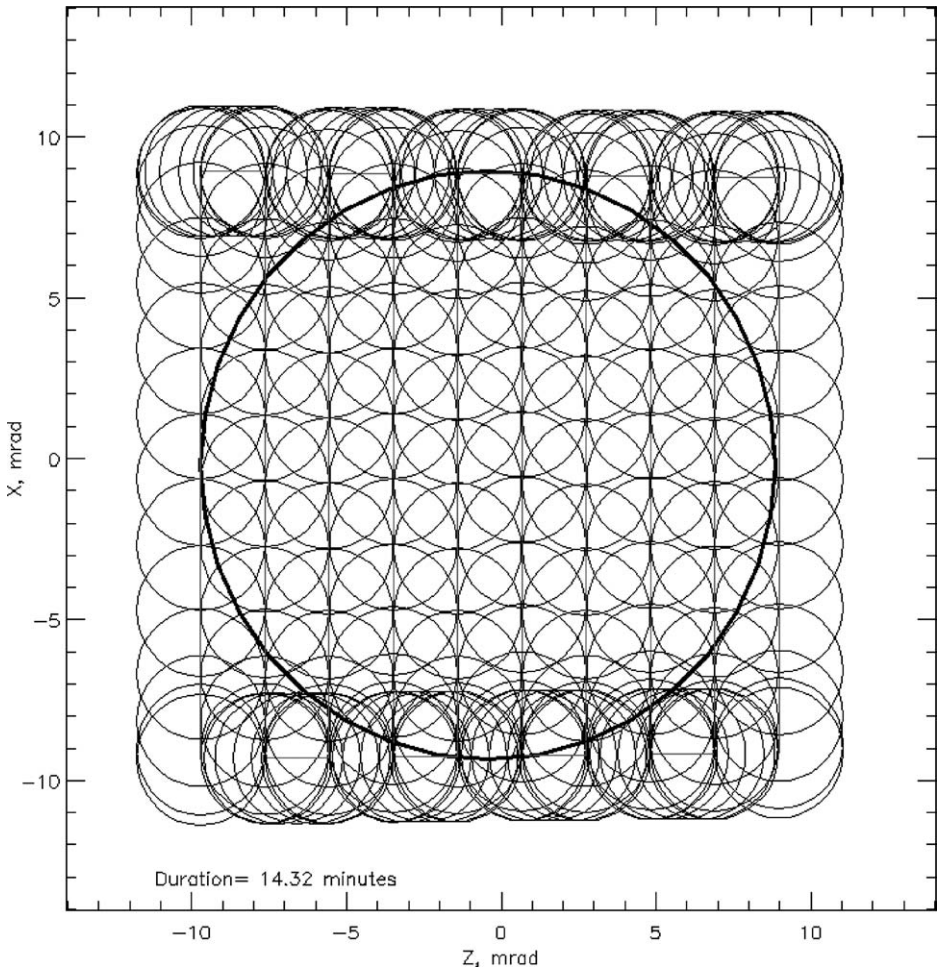

Figure 27. Idealized Nyquist-sampled FP1 map of an 18-mrad diameter disk. For frame time of 4.75 s (low spectral resolution mode) the execution time is 14.3 min. Designs of this type will be employed to map the cold dark sides of satellites to identify and quantify thermal inertia anomalies.

Composition. The utility of the thermal infrared region of the spectrum for determining surface composition has become increasingly well known, e.g., in the study of asteroids (see review by Sprague, 2000) and of Mars (Christensen *et al*., 2000a,b; Bandfield, 2002; Christensen *et al*., 2003; Hoefen *et al.*, 2003) Of special interest to Cassini will be signatures of ices and processed organics, e.g., kerogen- and tholin-like materials. In addition to fundamental and lattice modes, e.g., of H_2O, a number of group frequencies involving stretching and bending modes of C, N, O, and H in various configurations are available to CIRS below 600 cm^{-1} (Socrates, 1980). The icy Galilean satellites are spectrally featureless from ∼8 to 50 microns (Spencer *et al.*, 2004), but the saturnian satellites may be different, or may show features at longer wavelengths. No useful compositional information on the

saturnian satellites was obtained from Voyager IRIS data, due to low signal to noise and to limited spectral coverage. In addition, no adequate spectral database existed at thermal wavelengths. We are now implementing laboratory studies of ices and refractory materials that will cover the spectral range from 10 to 4000 cm^{-1} (1000 to 2.5 μm). The activity will be focused on studying the influence of mixtures of refractory material (silicates, oxides, amorphous carbon) and ice(s) (H_2O, CO_2, CO, NH_3, etc.) on the reflectance and emittance spectroscopic behavior. Another important aim is to improve the knowledge on the temperature dependence of optical properties of refractory and icy materials and their mixtures (Mennella *et al.*, 1998). In the spectroscopic range above approximately 50 cm^{-1} the fundamental diagnostic spectral structures (Christiansen, reststrahlen, and transparency features) are present. Moreover, at longer wavelengths spectral information on deeper layers of the surface is obtained. Detailed laboratory studies are needed to increase the database on the optical properties of different components useful for the interpretation of icy satellite spectra. Of particular interest to CIRS is the spectral range from 200 to 10 cm^{-1}, where water ice becomes increasingly transparent. This offers the possibility of recording increased thermal contrast, which would accentuate the spectral signatures of minor constituents with long wavelength features such as low frequency fundamentals and lattice modes. The associated thermal gradients with depth should have much the same effect as atmospheric gradients in increasing the contrast of spectral features due to components of the medium. To exploit this, CIRS will make extensive FP1 observations at local times at which vertical thermal gradients are at their maximum. In addition, observations will be made with FP3 at very high signal to noise to accentuate subtle reststrahlen features that might be present in the 600–1100 cm^{-1} (15 to 9 μm) region.

Thermal structure (solid state greenhouse). The concept of a solid state greenhouse was first considered for Io and the other Galilean satellites (Matson and Nash, 1983; Brown and Matson, 1987; Matson and Brown, 1989).

It accounts for the fact that sunlight is absorbed over a significant range of depths below an icy surface, while the opacity of ices in the thermal infrared means that thermal emission occurs only from the uppermost surface. As with an atmospheric greenhouse, mean temperature at depth may thus be higher than mean surface temperatures. CIRS can exploit the wavelength-dependent transparency of water ice beyond 50 μm to measure vertical thermal gradients at different local times, using principles analogous to atmospheric thermal sounding. The depth to unit optical depth as a function of wavelength can be estimated using ice optical properties and regolith densities inferred from derived thermal inertias. Sold-state greenhouse effects can thus be identified or constrained.

3.3.2. *Current Endogenic Activity*

Several of Saturn's icy satellites may show evidence of recent activity unknown in other satellite systems. These include the "wispy terrain" deposits of Dione and Rhea, and the uniquely bright surface of Enceladus together with the satellite's

location in the most concentrated part of the diffuse E-ring. Each of these could be interpreted as the result of effusive or eruptive activity (though other possibilities have been considered for the relationship between Endeladus and the E-ring, e.g., Haff *et al.* (1983) or Hamilton and Burns (1994)). CIRS will search for thermal anomalies and unusual spectral signatures as evidence of current activity.

Cosmogonic arguments suggest that the saturnian satellites may have formed with up to 20% ammonia hydrate (Lewis, 1972). While evolution subsequent to accretion may have been inadequate to melt the water ice component of these bodies, it is very likely that the melting point of $NH_3 \cdot H_2O$ ice ($\sim$175K) was exceeded (Ellsworth and Schubert, 1983). If current activity involves the liquid eutectic mixture, its thermal signature will be unmistakable in both FP3 and FP4 (Figure 23). Further, effusion or eruption of this material will be accompanied by an evaporative or ejected plume as material is released to the vacuum of space. CIRS will then be able to detect possible spectral signatures of gases and condensates in the plume, as was done with IRIS data for a plume on Io (Pearl *et al.*, 1979). NH_3 has a strong broad band centered near 1100 cm^{-1}. CIRS will make repeated observations of Enceladus throughout the tour. Emphasis will be on mapping the disk with FP3 and FP4, both to establish ongoing activity, and to follow its temporal behavior.

3.4. SATURN'S RINGS

Saturn has the most massive, extended and diverse planetary ring system in the solar system. Its three main rings (A, B, and C) span a radial distance of almost 70,000 km. A large population of particles orbits Saturn in intricate patterns with recognizable structure on all scales down to the Voyager observational limit of less than 100 m. A number of gaps fall within the main rings, some of which contain narrow ringlets. The total mass of the main rings is equivalent to the mass of the small Saturnian satellite Mimas. Four additional, much fainter rings (D, E, F and G) have been discovered thus far using ground-based or interplanetary spacecraft observations. Cuzzi *et al.* (1984) and Esposito *et al.* (1984) give comprehensive overviews.

Saturn's rings circle the planet in a region where the planet's gravitational tidal force is greater than the attractive forces between individual particles. Here the particles cannot accrete to form satellites. The origin and evolution of Saturn's rings are not well understood. Detailed measurements by the Voyager and Pioneer spacecraft provide evidence that Saturn's rings may evolve rapidly under the action of physical processes that may reduce their lifetime to less than 100 million years, a small fraction of the age of the solar system. The most efficient mechanisms for ring particle removal are erosion by meteoritic bombardment or ultraviolet radiation on ring particles, and the gravitational interactions with nearby satellites that finally drive the ring system toward the planet. However, the evolution of the rings relies on poorly known fluxes of impactors, which set the rate of erosion, and

on poorly understood physical properties of particles, which govern the outcome of interparticle collisions. If the rings are recent, a parent body would have to be destroyed in the neighborhood of the planet within the last few hundred million years, but the probability of having a close satellite disrupted on this timescale is small. Another possibility is that a comet may have been captured and destroyed by tides. However, the water ice on the surface of particles in Saturn's rings appears to be too pure to be of cometary origin, so a different parent may be needed.

Saturn's rings can be observed from Earth only over a narrow range of phase angles (0°–6°), which limits probing their properties. The two Voyager spacecraft did better, in that they observed Saturn's rings at phase angles ranging from 6° to 155°, two different solar elevations (3.8° and 8°), and over a broad range of opening angles on both the illuminated and unilluminated sides. IRIS recorded the ring's spectra between 180 and 2500 cm^{-1} (55.5 − 4 μm) with a spectral resolution of 4.3 cm^{-1} and a 4.4-mrad FOV on the sky. IRIS also had a single channel radiometer with a common FOV operating in the visible and near infrared, 0.8–2.5 μm.

CIRS will provide major advances over previous spacecraft infrared observations of the Saturn's rings in two respects: the extension of the spectral range to submillimeter wavelengths and the use of a linear array with much finer spatial resolution in the mid-infrared. With these new capabilities, CIRS can address many of the ring objectives of the Cassini mission, particularly those pertaining to composition, ring particle thermal properties, vertical dynamics, rotation states, and radial thermal structure. The properties of faint rings will be also explored. Cuzzi *et al.* (2002) provide a more detailed discussion of Saturn's rings and of the integrated ring measurements planned with the Cassini orbiter instruments.

3.4.1. *Particle Composition*

Ring particle composition is a key parameter in determining scenarios for the formation of the rings and their dynamical and chemical evolution. The bulk of the ring material appears to be water ice (Pilcher *et al.*, 1970; Puetter and Russell, 1977; Epstein *et al.*, 1984). Its relatively red color at visual wavelengths requires small amounts of unidentified impurities in the surface layer of ring particles (Cuzzi and Estrada, 1998). The nature of the non-icy constituents, their link with the composition of close satellites, comets or meteoroids, and their degree of mixture with water ice all provide clues to the origin of the rings.

Voyager spacecraft images showed radial color and albedo variations across the rings (Smith *et al.*, 1982; Dones *et al.*, 1993; Doyle *et al.*, 1989; Estrada and Cuzzi, 1996). The A and B rings appear redder than the C ring and the Cassini division. The radial color variations likely indicate variations in composition (Estrada and Cuzzi, 1996). The most probable candidates are silicates, iron oxides or organics, which may account for the features in the observed spectrum not attributable to water ice (Clark and McCord, 1980). Recent modeling of the visual and near-infrared composite spectrum has favored a surface composed of an intimate mixture of water ice with a few percent of organic tholins, with the adjunction of traces of

segregated amorphous carbon grains (Poulet and Cuzzi, 2002). This supports the studies by Cuzzi and Estrada (1998), which showed that the radial color variations of main rings were consistent with the pollution of this same kind of intimate mixture from carbonaceous material brought in by interplanetary debris. While this intrinsic composition is supported by observations, the organic contaminants have not been unequivocally identified (Poulet and Cuzzi, 2002). The ability of organics to explain observations further in the infrared or in the radio wavelength domain has yet to be tested. Finally, ground-based thermal infrared spectroscopy in the 8–13 μm window seems to rule out the presence of silicates in Saturn's rings (Lynch *et al.*, 2000). Voyager IRIS saw no spectral structure out to 50 μm (Hanel *et al.*, 1981, 1982). Future measurements by the CIRS instrument will produce additional submillimeter temperatures at a variety of geometries.

At 100 K the absorption coefficient of water ice decreases by over two orders of magnitude from 200 cm^{-1} to 10 cm^{-1} (50 to 1000 μm), making the material progressively more transparent (Section 3.3). This decrease is primarily responsible for the dramatic variation in the long-wavelength spectrum of Saturn's rings, which changes from nearly blackbody emission at 20 μm to essentially reflected planetary radiation by 1 cm (Figure 28). The ring emissivity is therefore very dependent on the fraction of other non-transparent materials. Ring particles have low emissivity

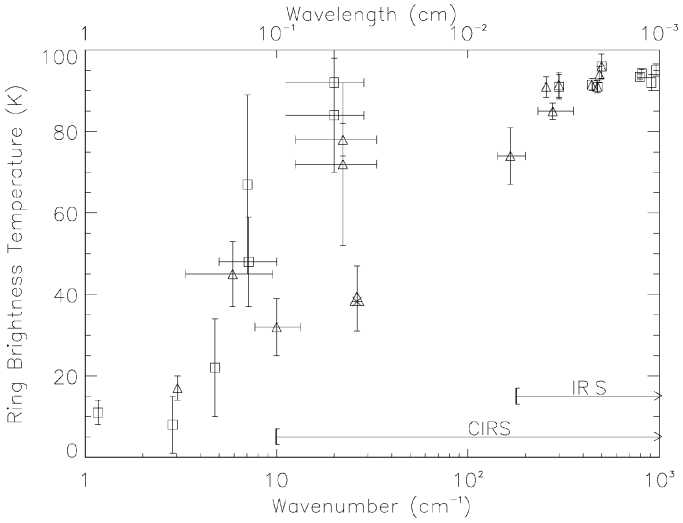

Figure 28. Brightness temperatures of Saturn's B ring for ring tilt angles $\phi > 25°$ (squares) and ϕ between 20° and 25° (triangles) relative to the sun. Between wavelengths of 50 μm and 1 mm (200 cm^{-1} and 10 cm^{-1}), the absorption coefficient for water ice at 100 K decreases by a factor $\sim 10^4$, making the material progressively more transparent. This gives CIRS the ability to probe icy material to various depths, providing a powerful tool for the investigation of the composition and physical properties of this material. The open symbol data can be found tabulated in Esposito *et al.* (1984). The triangle with the embedded asterisk is from Roellig *et al.* (1988).

and high reflectivity in the radio wavelength range and essentially scatter planetary radiation (De Pater and Dickel, 1991). Interpretation of microwave observations, which also sample the bulk of the ring mass by this effect, constrain the mass fraction of the non-icy silicate material to be less than 10% (Epstein *et al.*, 1984); it could be as low as 1% if uniformly mixed (Grossman *et al.*, 1989). Ground-based observations in the 100-μm to 1-mm region are sparse and difficult because of the absorption of water vapor in the Earth's atmosphere. Very broad beam observations, which also suffer from a blending of planetary and ring signals, show that the ring brightness temperature rolls off somewhere in this wavelength region. For example, the B ring brightness temperature changes from 90 K at 20 μm to near 10 K at centimeter wavelengths (Esposito *et al.*, 1984; Cuzzi *et al.*, 1984; Haas *et al.*, 1982). Exactly where the spectrum turns over is not known. Some broadband observations (Courtin *et al.*, 1979; Whitcomb *et al.*, 1980; Cunningham *et al.*, 1981) seem to imply that the spectrum remains flat out to $\sim$400 μm, before particle-size-related effects decrease the emissivity. However, later work by Roellig *et al.* (1988) at 380 μm (26 cm^{-1}) seems to indicate that there may be a gradual decrease in observed ring brightness temperature from the infrared into the radio. Roellig's values are about a factor of two smaller than values determined by the authors listed above.

Thanks to its unique sensitivity in a broad spectral range (Table I) and its good spatial resolution throughout the Cassini tour, CIRS will have the ability to probe icy ring particles to various depths, thus providing a powerful tool for the investigation of their composition and the way it varies with distance to the planet. Although the spectral signatures of C-H-N-rich organic material are mostly located in the near-infrared domain, some are still detectable in the mid-infrared, by the signature of stretch vibrations of N-H single bonds at 750 cm^{-1} (13 μm) for example. Silicate features, if any, may also be detected near 10 μm and 20 μm. The ring material may contain clathrate hydrates of ammonia and methane. The current observations in the near infrared cannot rule them out, because their spectral signatures are masked by water bands (Puetter and Russell, 1977). Identification of clathrate hydrates is only possible in the mid and far infrared where specific features can be distinguished from water and guest molecule signatures (Hudson and Moore, 1993). But laboratory determinations of optical constants in the far infrared of possible constituents (ammonia, methane clathrate hydrates) are required to identify them accurately. Any detection of clathrate hydrates in the mid and far infrared would imply a recent resurfacing of ring particles, as the lifetime of these volatiles should be strongly reduced by sputtering. Cubic crystalline water ice has been identified at the surface of Saturn's ring particles (Grundy *et al.*, 1999). The presence of amorphous ice is not ruled out yet. Condensing at low pressure and temperature (between 40 and 70 K), water ice adopts an amorphous state. If warmed gradually, it is irreversibly transformed into cubic crystalline ice above 110 K and then into hexagonal ice above 150 K (Smith *et al.*, 1994). If formed at a temperature greater than 110 K, solid structure of water ice particles remain crystalline despite their

actual lower temperature (90 K). Absorption features of crystalline water ice at 44 (227 cm^{-1}) and 62 μm (161 cm^{-1}), which disappear in the amorphous state, may be then strong indicators of possible scenarios of ring particle formation. They may be detected in the CIRS spectrum if the regolith particle size is small enough.

3.4.2. *Thermal Properties of Ring Particle Surfaces*

The dynamics and evolution of rings strongly depend on the outcome of interparticle collisions and on the self-gravity of the rings. Energy loss, mass transfer, and sticking probability for relevant impact velocities will favor either aggregation or disruption and erosion of particles, modifying the size distribution and velocity dispersion, and thus the dynamics and structure of the rings. Saturn's rings consist of a vast array of irregular centimeter-sized to house-sized particles, the bulk of the ring mass concentrated in particles with radii of a few meters (Marouf *et al.*, 1983). A single ring particle has never been observed because of the limited spatial resolution of spacecraft instruments (e.g., a few kilometers for Voyager). Surface properties that largely constrain the result of a collision can therefore only be inferred from indirect observations. Reflectance models applied to visible and near-infrared spectra of Saturn's rings support the idea of particles covered by a regolith of 50 μm-sized grains on average (Pollack *et al.*, 1973; Pilcher *et al.*, 1970; Clark and McCord, 1980; Poulet and Cuzzi, 2002). Recent analysis of the phase function of Saturn's rings near opposition suggests that A and B ring particles are significantly rougher than those in the thin C ring, maybe lumpy particles, still covered with micron-sized particles (Poulet *et al.*, 2002).

Measuring the thermal inertia of ring particles is an indirect and independent method to explore the structure of the ring particle surface. The thermal inertia can be obtained from observations of transient changes in temperature as ring particles cross the planetary shadow boundaries or at their surfaces as they rotate. This experiment has been proposed initially by Aumann and Kieffer (1973) to measure the ring particle sizes. Ground-based observations at 20 μm in the early 1980's of the heating rate of B ring particles after eclipse behind Saturn (Froidevaux *et al.*, 1981) have constrained their thermal inertia to be very low, as low as the thermal inertia of Galilean satellites, if the particles are centimeter-sized. Pioneer measured a 15-K drop in temperature of the C ring during eclipse and less than 12 K for the A ring (Froidevaux and Ingersoll, 1980) confirming this qualitative estimate. From the observed heating curves at 20 μm, Ferrari *et al.* (2003) have quantitatively estimated the thermal inertia for the B and C rings to be $3.5 \pm 1.2\ Jm^{-2}K^{-1}s^{-1/2}$ and $6.3 \pm 3.0\ Jm^{-2}K^{-1}s^{-1/2}$, respectively. They are very similar to the thermal inertia of Centaur objects like Chiron or Asbolus. They correspond to very low thermal conductivities, of the order of 10^{-5}–10^{-4} W m^{-1} K^{-1}, depending on the actual porosity of the layer. These thermal properties are consistent with a frosty regolith, fractured by cracks from collisions or thermal stresses, or alternatively with very porous particle aggregates. The estimates have assumed an energy balance typical of slowly spinning particles, but did not account for the anisotropy of the heating

on their surfaces along their orbits. In general the particle surface temperature and thermal emission vary on the surface along the rotation axis ("latitude") and azimuthally ("longitude"). A new model is being developed to use the crossing of the shadow and the day/night anisotropic emission to recover both the spin and thermal inertia of spherical particles from observations at different phase angles (Leyrat *et al.*, 2003).

Ground-based observations are limited to phase angles smaller than about 6°, but observations by the Voyager 1 IRIS spectrometer cover both low and high phase angles. The new model has recently been applied to IRIS observations of the C-ring particles passing into Saturn's shadow (Spilker *et al.*, 2003; Leyrat *et al.*, 2003). However, the data are limited in the azimuthal sampling of the cooling and heating curves, and in phase-angle coverage. This makes it difficult to derive spin and thermal properties of the ring particle surface unambiguously. The 4-year-long Cassini tour will provide the geometries, azimuthal and radial sampling necessary to address these problems. The first minutes of both the cooling and heating curves will be observable. Measurements just at the entry and exit from the eclipse allow one to test the heterogeneity of the individual particles, i.e., whether the thermal conductivity changes between the first few millimeters below their surface and their interior. A change in the cooling/heating rates in these periods may appear depending on the thickness of a low-thermal-inertia surface layer on an eventually more compact core. Energy transport in regoliths depends on the compactness of the layer and the possible existence of fractures that prevent heat propagation, and also on the size, optical and thermal properties of the regolith grains (Hapke, 1996a,b; Snyder-Hale and Hapke, 2002). CIRS will also address the question of the regolith grains by studying their emission as a function of wavelength for the main rings.

3.4.3. *Ring Vertical Dynamics and Particle Spins*

The Voyager observations in the early 1980's revealed numerous radial and azimuthal structures in the disk of Saturn's rings that are the fingerprints of the physical processes at play. Known gravitational interactions with nearby satellites can explain fine to medium scale structures in the rings, e.g., spiral density waves (horizontal perturbations), bending waves (vertical perturbations), satellite wakes, or eccentric ringlets. The observation of these phenomena helps both in understanding local dynamical properties, such as viscosity, random velocities, and vertical height, of the ring layer, and in understanding the physics and efficiency of the processes involved. The scale height is directly related to the particle size, particle spin, and Keplerian velocity (Cuzzi *et al.*, 1984).

Vertical structure. Voyager radio and stellar occultation measurements place upper limits of 150–200 m on ring thickness in the main rings (Tyler *et al.*, 1981; Lane *et al.*, 1982). Locally this may be caused by waves excited by outer satellites. Studies of bending waves give smaller estimates, with a local thickness of about 30 m in the A and B rings (Shu *et al.*, 1982) and perhaps as low as 1 m in the C ring (Rosen, 1989). The A and B rings may thus be many-particles thick, whereas the

thin C ring appears to be a monolayer. The compatibility of the multilayer structure with Voyager observations at high phase angle is questionable (Dones *et al.*, 1993). Cuzzi *et al*. (2002) use HST observations to show that vertical structure may vary with location and the multilayer structure may not always be applicable.

The vertical thermal structure in the rings can constrain the typical ring scale height, as the temperature depends on the mutual shadowing and penetration of the sun's rays into the ring layer(s). A thermal gradient between the lit and unlit face of the rings should exist across a many-particle-thick ring. The brightness temperature of the unlit face of Saturn's rings at 45 μm was first measured by Pioneer (Froidevaux and Ingersoll, 1980). The determined value of 54 $\pm$ 3 K was confirmed by Tokunaga *et al.* (1980) from ground-based observations at 20 μm with a brightness temperature of 56 $\pm$ 1K for the B ring. Tokunaga *et al.*, suggest that this temperature may originate solely from Saturn's visual and thermal illumination and does not require a supplementary heating by scattered solar light. How this gradient varies from the thin C ring or the optically thick A ring is unknown. Several ground-based observations at mid-infrared wavelengths in the 70s and 80s have shown that the lit face temperature increases with solar elevation for the optically thick A and B rings but decreases weakly for the less opaque C ring. Many thermal models have been elaborated to reproduce these observations, including alternatively mono- or many-particle-thick layers, and vertical inhomogeneity (Froidevaux, 1981; Kawata, 1983), but nothing definitive can be concluded. The objections about a possible monolayer structure for the C ring (Esposito *et al.*, 1984) have been overturned by recent ground-based observations in the thermal infrared (Ferrari *et al.*, 2003). In brief, the actual vertical structure of Saturn's main rings is uncertain. Viewing geometries have to be diversified to separate both types of vertical structures, most particularly how the brightness temperature varies with the elevation of the observer at fixed solar elevation and phase angle.

Vertical Dynamics. Ring particles, as they collide, are tumbling around the mid ring plane with a vertical excursion governed by the local dynamics. The ring scale height is one measure of this maximum dispersion. The thermal history of a particle along its orbit is also a marker of vertical dynamics. It is conditioned by the time it spends under sunlight and in the planetary shadow. Its ability to warm up at the exit of the shadow is a function of the average time it spends in the shadow of its neighbors, which is controlled by its vertical dynamics. Any difference in the heating curve between faces will reveal asymmetry in the time spent on each face by particles.

Particle spins. The actual distribution of particle spins in Saturn's rings is unknown. Most of the numerical simulations which have been developed to study this aspect are limited to monodispersed size distributions. The spin is prograde in the planet-fixed frame. The average spin value in the direction perpendicular to the ring plane and in a frame rotating with the particle at mean motion Ω is $\omega/\Omega \sim 0.3$ (Araki, 1991; Salo, 1995; Richardson, 1994). This number is fixed by the spatial distribution of impacts on the particle. The dispersion around this value is highly

dependent on friction, energy loss or on the optical depth. When gravitational scattering is taken into account, $\omega/\Omega \sim 0.66$ in regions when particle clusters can form, in the A ring for example (Salo, 1995). If small particles are added to the simulation, they spin faster and have a wider distribution of spins (Richardson, 1994). The spinning rate of ring particles can be estimated qualitatively from observations with a simple energy balance equation. Both monolayer and multilayer thermal models of Saturn's rings suggest slow rotators for the main rings (Froidevaux, 1981, Kawata and Irvine, 1975; Ferrari *et al.*, 2003; Spilker *et al.*, 2003). Slowly rotating particles means that particles are essentially emitting over just one hemisphere, so that the day/night temperature contrast is important. A thermal model is currently being developed to determine whether results of numerical simulations are compatible with current observations in the thermal infrared (Leyrat *et al.*, 2003).

3.4.4. *Radial Thermal Structure*

Ring opacity and temperature as a function of wavelength and radial distance from Saturn are important CIRS ring objectives. The radial and angular distributions of thermal flux from the rings provide a measure of ring opacity as a function of wavelength for various regions in the rings. Except for the C-ring, only crude estimates of ring opacity were derived from Voyager infrared data (Hanel *et al.*, 1981; Hanel *et al.*, 1982). CIRS will be able to determine ring opacity for all of the rings at high spatial resolution and over a broader range of wavelengths. These observations will provide the missing data on ring opacity from UV to radio wavelengths from which a detailed particle size distribution will be finally derived. The radial dependence of the size distribution in the disk is a key parameter to predict its reaction to perturbations and then its dynamical evolution.

The ring particles reveal their true physical temperatures at wavelengths of 10 to 30 μm; at 20 μm their emission (and measured brightness temperature) is very close to blackbody emission. The physical temperatures of the A and B rings are similar while the C ring and Cassini Division temperatures can be slightly higher. This behavior is consistent with lower visible albedoes observed for the C ring and Cassini Division (Smith *et al.*, 1981; Cooke, 1991). The lit sides of the A and B rings exhibit a pronounced decrease in temperature with decreasing solar inclination. As the solar inclination decreases, the densely packed ring particles in these higher optical depth rings begin to shadow one another, resulting in a decrease in overall ring temperature. Temperatures range from 90 K near maximum solar inclination to less than 60 K as the solar inclination approaches zero. On the other hand, the C ring brightness temperature increases slightly with decreasing solar inclination as a result of its low optical depth and increased filling factor. Temperatures range from 80 K to almost 90 K when the solar inclination is near its minimum. The temperatures on the unlit sides of the A and B rings are typically less than 60 K. With its low optical depth, the C ring temperature is similar on both the lit and unlit sides of the ring. Figure 29 shows the CIRS NESR per minute of integration time for spectral resolutions of 0.53, 3.0 10.0 and 15.53 cm^{-1}. CIRS can easily

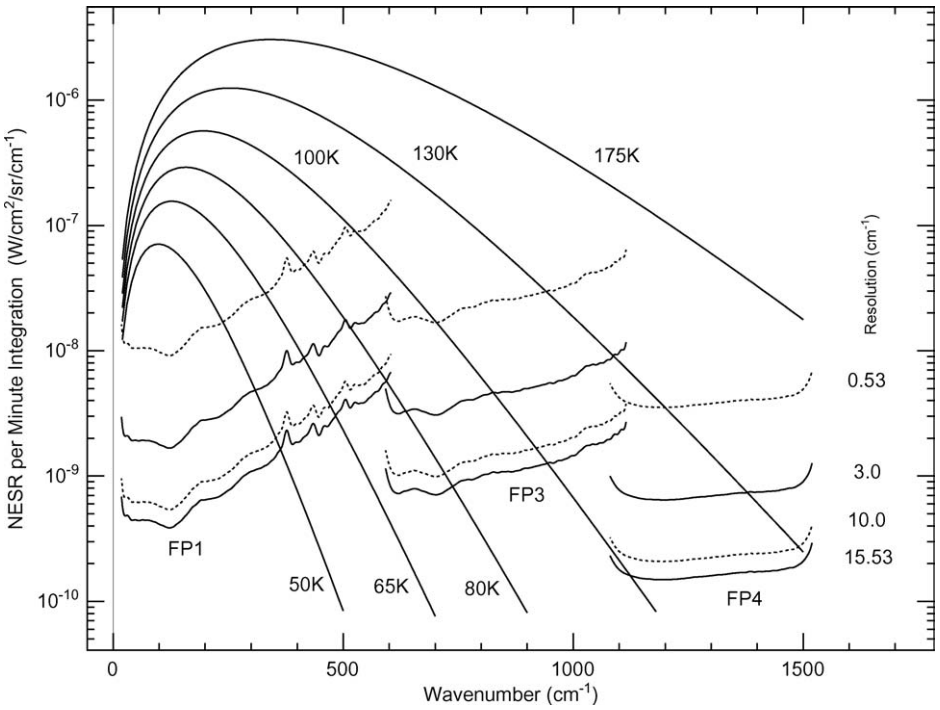

Figure 29. Planck radiances over the full CIRS spectral range for various temperatures. Superposed is the CIRS NESR for several spectral resolutions, assuming one minute of integration time. Ring temperatures vary from 60 K to 90 K, as a function of the solar illumination angle and of the lit or unlit sides of the rings. Comparison with the brightness temperatures of the rings shown in Figure 28 indicates that CIRS has the sensitivity to adequately probe the sub-millimeter portion of the rings' spectra.

measure the brightness temperatures of the main rings. Decreasing temperatures in the submillimeter region will make measurements in this region more challenging (see Figure 28 for submillimeter temperatures).

Brightness temperatures and optical depths were obtained from the IRIS spectra for the A, B and C rings (Hanel *et al.*, 1982). The ring was modeled as a simple, homogeneous, non-backscattering slab (multilayer) that radiates as a blackbody. For the unlit C ring the derived brightness temperature was 85 $\pm$ 1 K, and the optical depth was 0.09 $\pm$ 0.01, consistent with the values obtained by Froidevaux and Ingersoll (1980) from Pioneer data. Brightness temperatures for the A and B rings are 50 K to 60 K for the unlit A ring, <50 K for the unlit B ring and 70 K to 75 K for the lit B ring. These data are uncorrected for optical depth and geometry, so they represent lower limits on temperature. Normal optical depths for the Cassini Division, A and C rings were in agreement with Voyager and ground-based values at shorter wavelengths (Smith *et al.*, 1981; Froidevaux and Ingersoll, 1980; Sandel *et al.*, 1982). The higher temperatures of the C ring and Cassini Division particles

are consistent with their lower visible albedos. Esposito *et al.* (1984) and Cuzzi *et al.* (1984) review in greater detail the observations of thermal radiation at wavelengths $\sim$10 μm to $\sim$1 cm from Saturn's ring particles.

More recent work on the radial thermal structure of the C ring has been done by Spilker *et al.* (2003) assuming that the ring particles are in a monolayer. Temperatures were found to decrease with increasing radial distance in the inner C ring, flatten somewhat in the middle of the unlit C ring and then decrease further in the outer C ring. For an albedo of 0.24 the slight decrease in temperature in the C ring can be mostly explained by including the Saturn visible and thermal contributions. Using this same albedo (0.24), the inner C ring is slightly warmer and the outer C ring is slightly cooler than the model. This implies either that the albedo is not constant throughout the C ring or some other geometric factor must be considered. The downward trend in temperature with increasing radial distance is consistent with previous measurements: temperatures decrease and albedoes increase from the inner to the outer C ring (Cooke 1991). It is also consistent with the optical depth trend since the innermost particles are least shaded and are the warmest.

3.4.5. *Faint Rings*

In addition to the main A, B and C rings, Saturn has four much fainter rings, designated D, E, F and G. All are composed primarily of micron-sized dust and have optical depths τ ranging from 0.1 down to $\sim 10^{-6}$, compared to $\sim$1 for the main rings. Dust grains in the Saturn system are expected to have very short lifetimes, due to a variety of removal and destruction mechanisms including solar radiation pressure, electromagnetic perturbations and drag forces, micrometeoroid erosion, and sputtering. Hence, the dust in these rings must be continuously replenished from (often unseen) embedded populations of "parent" bodies. See Burns *et al.* (2001) for a thorough review of the physical processes at work in these rings.

The D ring occupies the region interior to the C ring. It consists of two narrow ringlets surrounded by broad belts of fainter material with $\tau \sim 10^{-5}$ (Showalter, 1996). The F ring comprises a set of narrow strands orbiting 3000 km outside the A ring. In the finest-resolution images from Voyager, this ring showed peculiar structures variously described as kinks, clumps and braids (Smith *et al.*, 1981). These structures are probably related to gravitational perturbations from the nearby "shepherding" moons Prometheus and Pandora, although the details remain mysterious. This ring shows peak $\tau \sim 1$ but only over very narrow strands of $\sim$1 km width; more typical τ values range from 0.1 to 0.01 (Showalter *et al.*, 1992). Next outward, the G ring is an isolated, 6000-km-wide band centered 168,000 km from the center of Saturn. It is the faintest ring component, with $\tau \sim 10^{-6}$ (Showalter and Cuzzi, 1993). It was discovered in charged particle absorption signatures by Pioneer 11 (Van Allen, 1983) and imaged briefly during the Voyager encounters (Smith *et al.*, 1981). Finally, Ring E is the largest ring in this (or any) system, extending from inside Mimas's orbit to beyond the orbit of Dione. It is also vertically extended, with

a thickness varying from 6,000 km to 40,000 km at its outermost edge (Showalter *et al.*, 1991). Its τ is very low, 10^{-5}–10^{-6}, with a distinct maximum near the orbit of Enceladus, which probably serves as its major source body (Horanyi *et al.*, 1992; Hamilton and Burns, 1994).

All of the aforementioned physical processes at work in these rings depend strongly on the sizes of the dust particles (and on the charge-to-mass ratio, which itself varies with size). For this reason, the distribution of dust sizes in faint rings is a critical parameter for understanding these rings' origin and dynamics. To date, our understanding of the particle sizes is based on photometric modeling of the (typically very limited) visual and near-IR observations from Earth and Voyager. Thermal emission from these rings has never been detected.

Most visual photometry is difficult to interpret for particle sizes because additional particle properties (most significantly, shape) can substantially alter the light-scattering properties of a ring population. Cassini CIRS has a distinct advantage over visual and near-IR observations in that it will be observing the faint rings at wavelengths comparable to or greater than the sizes of the constituent particles. In this regime, the effects of particle shape are negligible, simplifying the interpretation of the data. The thermal emission from these rings is expected to drop off at longer wavelengths, owing to the diminishing thermal emissivity of grains as the wavelength approaches and exceeds the particle size. This dropoff should be readily observed in the data, so CIRS holds out the possibility of providing unique and important new constraints on the dust in Saturn's faint rings.

4. CIRS Observations

4.1. Observing Strategy

CIRS is versatile and complex. It has a commandable spectral resolution, the ability to view in both nadir and limb modes, and different fields of view in the mid and far infrared. This requires careful planning of observations. The angular sizes of the mid- and far-infrared fields of view dictate the distances particular measurements are made of the target body. The mid-infrared array pixels, being smaller, can be the drivers for useful observations further out than the larger far-infrared focal plane. For nadir observations, useful mapping can be achieved on a planet or satellite when the FOV subtends a few degrees of latitude. When limb sounding an atmosphere, best results are obtained when the FOV subtends a pressure scale height or less. Thus, for example, limb sounding of Titan can be usefully executed 5–9 h from closest approach in the mid-infrared (FP3 & FP4), but only within 2 h of closest approach in the far-infrared (FP1). Nadir maps in the mid-infrared will usually be done 12–28 h from closest approach (see below).

There is a tradeoff between spectral resolution and integration time that must be optimized by considering the scientific objective. The instrument noise, or the

Noise Equivalent Spectral Radiance (see Section 5.6.1), varies as

$$NESR \propto \frac{1}{\Delta\nu\sqrt{t}} \tag{6}$$

where $\Delta\nu$ is the spectral-resolution element in cm^{-1} determined by the interferogram scan length, and t is the integration time (Hanel *et al.*, 2003). Observations to retrieve the abundances of trace atmospheric constituents generally require the highest available spectral resolution, because the targeted features are unresolved, and the signal (line – continuum) scales as $1/\Delta\nu$. Although the NESR is greater for a given integration time (because $\Delta\nu$ is smaller), the SNR scales simply as $\sqrt{t}$. Hence, the search for new species entails long integrations. These tend to be done at larger distances from the target body, when there is more time available and fewer conflicts with other scientific objectives. However, other observations, for example the retrieval of vertical profiles of atmospheric temperature and aerosols, can be done with lower- resolution spectra and shorter integration times, allowing more extensive spatial mapping closer to the target body. In this case, the spectral features are either resolved (e.g., the pressure-induced lines of H_2 on Saturn, for tropospheric temperature sounding) or resolved sufficiently for the retrieval (e.g., the manifolds of the P, Q, and R branches of the ν_4 band of CH_4, for sounding the stratospheric temperatures of Saturn and Titan). In this case the signal is just the Planck radiance at the effective emission level, and it is independent of the spectral resolution. The SNR then scales as 1/NESR. One could in principle still use only the longest interferometric scans corresponding to the highest-resolution spectra, and then average adjacent wavenumbers in these spectra to achieve a higher SNR. However, there is a penalty in doing this. The gain in SNR is $\sqrt{\Delta\nu_L/\Delta\nu_H}$, where $\Delta\nu_H$ denotes the spectral resolution of the original spectrum and $\Delta\nu_L$ that for the spectrally averaged one. If shorter scans corresponding to $\Delta\nu_L$ are used instead, the gain in SNR is greater, $\Delta\nu_L/\Delta\nu_H$ from (6), because in this case no information from the scans has been discarded. Hence, it is generally more efficient for the interferometric scan lengths to be tailored to the spectral resolution required for the retrieval problem at hand.

4.2. SATURN

The 4-year Cassini tour has 74 orbits of Saturn, and it provides the opportunity to map Saturn's atmosphere globally, including looking for time variations over the life-span of the mission. This is aided by the varying geometry. For example, the inclinations of the orbits range from near equatorial to almost 78° near the end of the nominal tour. The bulk of the orbits have apoapses in the range 20–70 R_S, and periapses in the range 2.4–16 R_S. Figure 30 depicts typical CIRS observations of Saturn at different ranges from the planet. These correspond to the entries in the last column of Table II, which are linked to the major scientific objectives

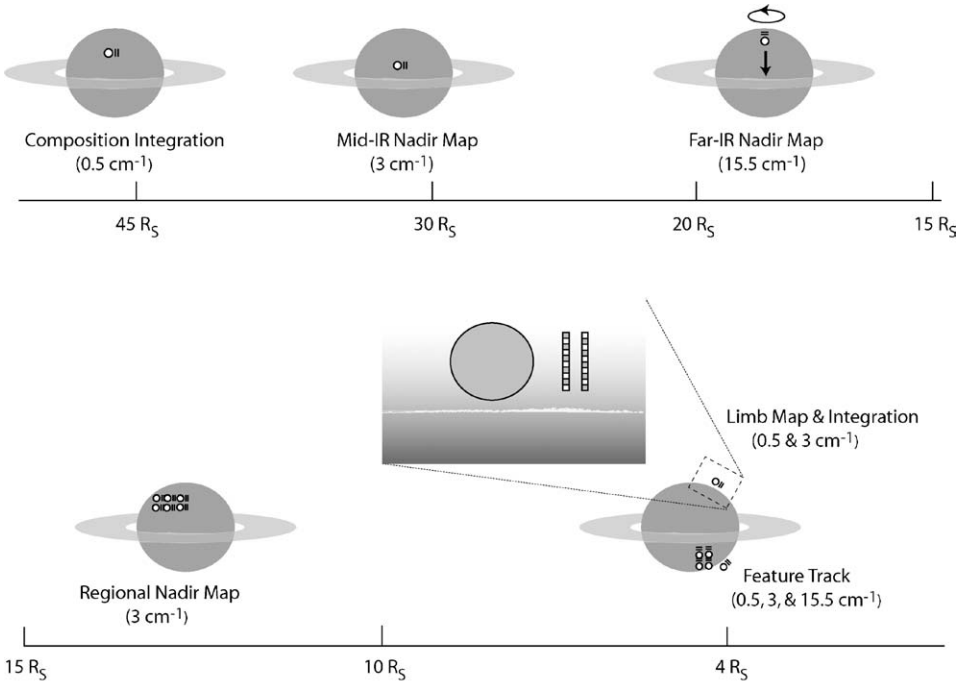

Figure 30. CIRS observations of Saturn at different ranges from the planet. Within a range of 32 R_S the CIRS fields of view are smaller than indicated, relative to Saturn's disk.

and measurement targets. The measurement objectives dictate the required spatial resolution (hence range to Saturn) and the spectral resolution used. Moving toward the planet, the observations are:

- *Composition integrations*. Typically done ∼45 R_S from Saturn, the individual mid-infrared pixels (FP3, FP4) subtend 0.8° of planetocentric arc on Saturn at the subspacecraft point. The arrays are aligned north-south, so they span 10 times that arc, or 8° of latitude at the subspacecraft point. The far-infrared focal plane, FP1, covers approximately 10° of latitude. The arrays are held fixed over one or more Saturn rotations. The spectral resolution is 0.5 or 1.0 cm^{-1}, and generally spectra will be averaged over longitude. The resulting long integrations will map the latitude distribution of the oxygen compounds H_2O (in FP1) and CO_2 (in FP3) and of stratospheric hydrocarbons (in FP3), such as C_3H_4 and C_4H_2. The integrations will also be used to search for new tropospheric species (in FP1), such as HCP, H_2S, H_2Se, and the halides. PH_3 can be mapped both in the far- and mid-infrared (FP1 and FP3). Isotopic ratios, such as [HD]/[H_2], [CH_3D]/[CH_4], [$^{13}CH_4$]/[$^{12}CH_4$], [$^{13}C^{12}CH_6$]/[C_2H_6] can be simultaneously retrieved from the

integrations. Because the fields of view do not cover Saturn's disk, latitude distribution must be composited from several integrations made over the tour.

- *Mid-IR nadir maps*. Executed ~30 R_S from Saturn, these have somewhat higher resolution than the composition integrations, but the attitude of the fields of view is identical. In this case the arrays span a 5°-latitude band (pixel resolution 0.5°) as Saturn rotates. The spectral resolution of the maps is 3 cm^{-1}, and there is sufficient signal-to-noise to provide longitude-latitude maps of temperatures in the tropopause region and in the upper stratosphere, using the FP3 and FP4 radiances. The latitude mapping must be composited from latitude bands acquired during the tour. Most latitudes will be observed at least two times during the tour to obtain median-term temporal variations. Individual bands will be observed for two successive rotations or longer to characterize short-term variations and also to determine the zonal phase velocities of coherent structures, such as waves. In addition to temperatures, the more abundant hydrocarbons, such as C_2H_6 and C_2H_2, and tropospheric compounds, such as PH_3, will be mapped.
- *Far-IR nadir maps*. These are driven by temperature mapping of the troposphere in the far infrared, down to approximately the 1-bar level (Figure 4). A spectral resolution, 15.5 cm^{-1}, is adequate for this purpose. This and the fact that the far-infrared portion of the spectrum is closer to the peak of the Planck function than the mid infrared means that shorter integration times are required. As a result, the fields of view can be scanned across Saturn. The scans are north-to-south scans (or vice versa) with flybacks. A scan rate of 0.25 mrad s^{-1} ensures a precision in the brightness temperature of 0.3 K. The requirement that successive scans be adjacent in longitude implies that they can only cover one hemisphere (northern or southern) as the planet rotates. Scanning over two or more rotations will provide information on short-term temporal variability and on the velocities of propagating waves. The mapping sequences are typically centered at 16–20 R_S, where FP1 subtends 4°–5° of planetocentric arc at the subspacecraft point. Although FP1 is the driver in these maps, temperatures in the upper troposphere and tropopause region can be also be retrieved using the H_2 S(1) line over the 600–670 cm^{-1} portion of FP3 (the spectral resolution is too coarse to resolve the Q-branch of the ν_4 band of CH_4 in FP4). Hence the arrays are aligned east-west for the north-south scans. Averaging the FP3 pixels provide both a good SNR and spatial resolution comparable to that afforded by FP1.
- *Regional nadir maps*. Similar to the mid-IR nadir maps described earlier but limited in time, these are executed at higher spatial resolution for select regions, e.g., a portion of the ribbon wave near 40°N. Typically done at a range of 12–15 R_S, the individual FP3 and FP4 array pixels subtend 0.2°–0.3° and FP1 3° of planetocentric arc at the subspacecraft point. At 3 cm^{-1} spectral resolution, stratospheric and tropospheric temperatures can be retrieved, as well as information on the spatial distribution of PH_3, NH_3, and major stratospheric hydrocarbons. At 0.5 cm^{-1},

better determinations of these gaseous constituents can be made, as well as of trace constituents and new species.

- *Limb maps*. Only the FP3 and FP4 pixel arrays have the spatial resolution to observe Saturn in the limb mode with approximately one scale-height resolution (60 km), and this must be done near periapsis. For these the arrays are aligned normal to the limb. A spectral resolution of 15.5 cm^{-1} is sufficient for retrieving temperatures over the altitude range 10–0.01 mbar (Figure 4). Given the spacecraft attitude-control uncertainty for pointing (± 2 mrad) two vertical positions are used at each location. Twenty minutes ensure a precision in retrieved temperatures better than 1 K. Eighteen locations can be measured over a 6-h period. The observations will cover a series of latitudes, and in some cases, held fixed at a given latitude, with Saturn's rotation providing a succession of different longitudes for the soundings. In addition to temperature profiles, the limb maps will allow the retrieval of stratospheric CH_4 (Section 3.1.1).
- *Limb integrations*. These are similar to the limb maps, except that the fields of view remain at a single location. A spectral resolution of 0.5 or 1.0 cm^{-1} is used to obtain vertical profiles of CO_2 and various stratospheric hydrocarbons.
- *Feature tracks*. This is a $\sim$5-h template for coordinated observations by CIRS, the imaging science experiment (ISS, Porco *et al.*, 2004), the visual and infrared mapping spectrometer experiment (VIMS, Brown *et al.*, 2004), and the ultraviolet spectrometer experiment (UVIS, Esposito *et al.*, 2004). The feature, or some specified area on Saturn, is tracked from limb to limb, as Saturn rotates. As the feature moves across the disk, an area equivalent to the $6^\circ \times 6^\circ$ ISS wide-angle FOV (corresponding to a latitude span of 17° at the subspacecraft point) is mapped by a series of scans. The nadir mapping will measure tropospheric temperature perturbations with a precision of 0.2 K, which, for example, can be correlated with motions and features in ISS images. The observations will also determine heat fluxes associated with the motion of the temperature anomalies. When the feature is on both limbs, limb soundings will retrieve stratospheric temperatures with a vertical resolution of about a scale height. These may show evidence of vertically propagating disturbances associated with the feature that transport momentum and energy to the stratosphere. For the temperature-sounding flavor just given, the spectral resolution is 15.5 cm^{-1}. An alternative, composition-driven, version is executed in similar fashion, except that the spectral resolution is higher (3, 1, 0.5 cm^{-1}). Because of the SNR requirements, a smaller area is mapped, $\sim 5^\circ$ latitude. Specific targets are the spatial distribution of NH_3 (with a SNR of 3–12), PH_3 (SNR $\sim$4–17), and stratospheric hydrocarbons. An important objective is to determine whether meteorologically "interesting" local regions, e.g., with strong vertical motions, are characterized by subtle differences in atmospheric composition.

There are other observations that can fit into the previously listed categories, but which have specific measurement targets. Among these is:

- *Radio-occultation-point observations*. Nearly simultaneous observations by CIRS and RSS exploit synergies of the two types of data. For example, the combination of CIRS and RSS data can provide a better determination of the He abundance (Section 3.1.1). Moreover, higher vertical resolution of temperature profiles retrieved from radio-occultation soundings can help in the analysis of temperature perturbations seen in CIRS temperature maps and cross sections. By the nature of the geometry of the occultation, which is observed on Saturn's limb, and also the relative orientation of the spacecraft high-gain antenna (used by RSS) relative to the CIRS boresight (90° apart in the sky), it is usually not feasible to do near-simultaneous observations, and the CIRS observations often must be done one or two Saturnian rotations away from the actual occultation. The targeted CIRS observation has two parts, nadir and limb. The nadir observation is similar to the MIR nadir maps and regional nadir maps, with the mid-infrared (FP3, FP4) arrays aligned north-south at a location so that the planetary rotation sweeps the occultation location through all three focal planes. Spectral resolution is 3 cm^{-1}. The limb observation is similar to the mid-IR limb map, described above (spectral resolution 15.5 cm^{-1}), except profiles are retrieved only in the vicinity of the occultation. When the competing demands of other activities preclude observing the occultation point, a fallback position is to observe the occultation latitude close in time to the actual event.

4.3. TITAN

There are 44-targeted flybys of Titan during the 4-year nominal Cassini tour. The most distant targeted flyby has a closest-approach altitude of 10,630 km, but virtually all the rest are within 3000 km, with over half around 950 km. Figure 31 provides a generic timeline for a close Titan pass (less than few thousand kilometers altitude at closest approach), and schematically depicts the various types of CIRS observations. These correspond to the entries in the last column of Table V.

The temperature-mapping sequences illustrate well the considerations that come into play for limb and nadir viewing when the different fields of view are the drivers. Moving closer in range to Titan, these sequences are (Figure 31):

- *Mid-IR nadir maps*. These use the radiances in the ν_4 band of CH_4. to map temperatures in the upper stratosphere (Figure 12). They are nominally 7-h sequences, ideally executed within a range of 380,000 km from Titan ($\sim$19 h from closest approach), where the mid-infrared array pixels each resolve 2.5° of body-centric arc at the subspacecraft point. With a fixed remote-sensing pallet, it is more efficient to articulate the spacecraft in a series of continuous slews, rather than discrete steps, across the disk in a push-broom fashion. A spectral resolution of 3 cm^{-1} (10-s interferometric scans) ensures adequate resolution of the P, Q, and R branches of the ν_4 band of CH_4. A slew rate of 4 μrad s^{-1} means that the 0.3 mrad pixels will move half their width in 40 s, or 4 interferometric scans.

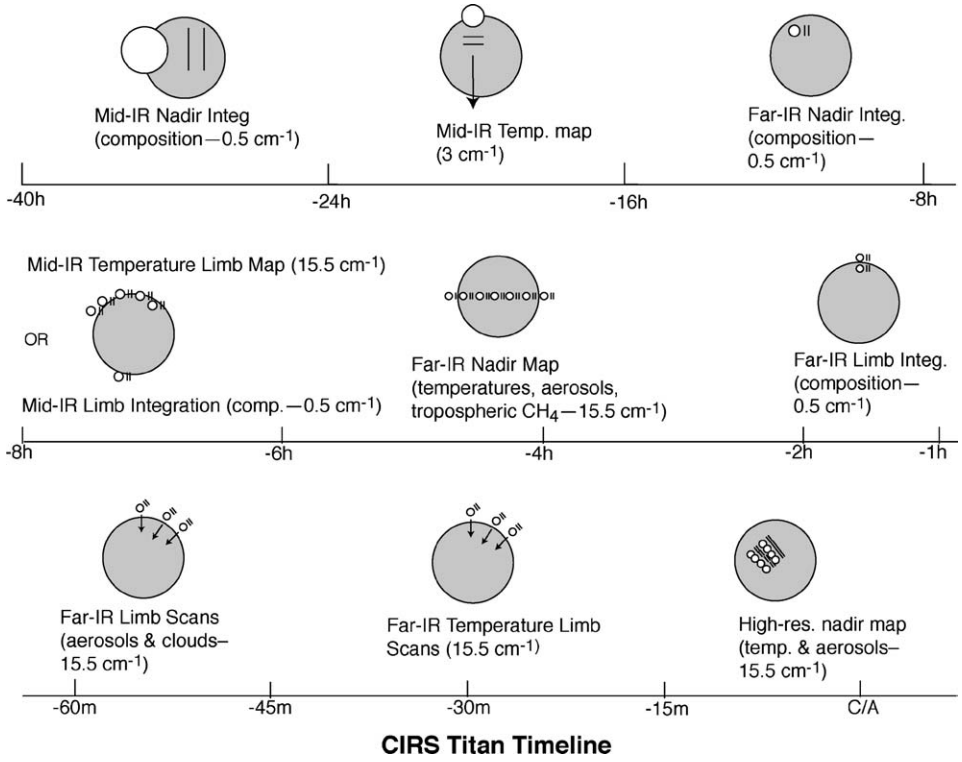

Figure 31. Generic Titan flyby timeline with CIRS observations. Time from closest approach can be converted to range by noting that the spacecraft velocity relative to Titan is typically 5.5–6.1 km s^{-1}. The relative size of the CIRS fields of view is smaller than indicated within 4 h of Titan closest approach.

Averaging these would ensure a precision of 0.25 K in the retrieved temperatures in the upper stratosphere.

- *Mid-IR limb maps*. These provide better vertical resolution in the upper stratosphere and mesosphere (Figure 12). At 6 h from Titan closest approach, or a range of 120,000 km, the mid-infrared pixels resolve 36 km on the limb, comparable to the scale height (42 km) in the upper stratosphere. In the limb mode, 15.5 cm^{-1} is sufficient to resolve the ν_4 band of CH_4 for temperature retrieval. The mid-infrared arrays are held steady on the horizon, normal to the limb. Twenty interferometric scans can be acquired in approximately one minute, sufficient for a retrieved temperature with a precision of 0.25 K. After one location is observed, the arrays are moved to the next position, a few degrees along the limb relative to Titan's center.
- *Far-IR nadir maps*. The 4-mrad FP1 FOV is the driver here. At 3 h from Titan closest approach, the range is 60,000 km, and the FOV subtends 5° of body-centric arc at the subspacecraft point (Figure 31). As with the mid-IR nadir maps,

the FOVs slew across the disk. To retrieve temperatures in the upper troposphere and tropopause region, a spectral resolution of 15.5 cm^{-1} requires a slew rate of 40 μrad s^{-1}. However, if surface temperatures are simultaneously retrieved from the radiances in the window near 520 cm^{-1} (which will usually be the case), much slower slew rates are needed (see below). An additional complication arises in using lower-resolution spectra below 150 cm^{-1} for temperature retrieval, because of the superposition of several optically thin rotational lines of CH_4, HCN, H_2O, and other molecules, discussed earlier, on top of the underlying broader spectrum associated with N_2 pressure-induced absorption. Adequate resolution of these lines requires a spectral resolution of at least 1 cm^{-1}. To avoid a systematic bias in tropospheric and tropopause temperatures retrieved from the lower-resolution spectra, an empirical correction will be applied as a function of latitude. This will be based on the far-IR nadir composition integrations described below, which will be done at 0.5 cm^{-1} resolution and at 160,000–270,000 km from Titan. As a check, a few of the far-IR nadir map scans closer in will be executed at 1 cm^{-1} resolution.

- *Far-IR limb temperature and aerosol scans*. Done within 75 min of closest approach (Figure 31), the best resolution for temperature sounding occurs inside of 45 min. At 30 min out the FP1 FOV resolves 40 km altitude on Titan's limb, about one scale height in the upper stratosphere. Spectra with 15.5 cm^{-1} spectral resolution will be acquired during vertical scans of 40 μrad s^{-1}. From these, vertical profiles of temperature between 8 and 100 mbar will be retrieved. As with the nadir-viewing spectra, the low-resolution limb spectra will require the effects of unresolved rotational lines to be corrected before temperatures are retrieved. This is possible through the use of far-infrared limb integrations, acquired at one to two hours from closest approach at full spectral resolution.
- *Surface-temperatures mapping.* As noted in Section 3.2.4, both nadir and limb observations in the far-infrared are required to separate surface and stratospheric emission. The requisite limb spectra will be obtained in the dedicated aerosol limb and temperature scans, taken within 75 min of Titan closest approach (range 25,000 km), which were described above. The far-infrared nadir mapping can be done during the sequences described for mapping the troposphere and tropopause temperatures. However, the scan rates must be very slow, $\sim$6 μrad s^{-1}; this is equivalent to an integration time of 5 min in the 4-mrad FP1 FOV.

The sequences described above can also be used for compositional studies. However, there are other observations dedicated to longer integration and high spectral resolution, 0.5–1.0 cm^{-1}. Moving toward Titan closest approach, they are:

- *Mid-IR nadir integrations*. These are typically done 500,000–1,000,000 km from Titan; for targeted flybys, this occurs one day or greater from closest approach. At this point the arrays span 60% or more of Titan's radius. When the arrays are oriented north-south, the integrations will the latitude distribution of hydrocarbons

(CH_4, CH_3D, C_2H_2, C_2H_4, C_2H_6, C_3H_8, C_4H_2, C_3H_4), nitriles (HCN, HC_3N and CH_3CN), the oxygen compound CO_2, and new species (e.g., the CH_3 radical, C_6H_6, $CH_2{=}C{=}CH_2$, etc.).

- *Far-IR nadir integrations*. These integrations are executed closer in to Titan, at a range of 160,000 to 270,000 km (8–13 h from closest approach). They will measure the stratospheric emission from the rotational lines of CH_4, HCN, CO, and H_2O, as well as providing a basis for detecting new compounds. For better spectral contrast of the stratospheric emission, the integrations are at 1.5–2 airmasses. Generally, only one location will be observed during an integration. Spatial mapping must be composited from multiple flybys during the tour.
- *Mid-IR limb integrations*. Done 5–9 h from Titan closest approach, these are similar to the mid-IR limb maps described above, except in the execution. Instead of repositioning at successive locations on the limb, the arrays are centered at two altitudes – 125 km and 225 km – on the limb at a single location. The targeted species are identical to those for the mid-IR nadir integrations, above, but the limb-viewing geometry provides better vertical resolution with the arrays.
- *Far-IR limb integrations*. These occur between ∼one and two hours from closest approach. The FP1 focal plane is centered at 225 km and 125 km, for coarse vertical profiles of CH_4, HCN, CO, and H_2O. The latter two require the longest integrations, about 90 min for each position. Typically this cannot be accommodated during a single flyby, and the vertical profiles and latitude mapping must be composited from several Titan flybys.

Nadir observations are typically done further from closest approach than the corresponding limb observations. The former therefore have more time afforded to them and thus offer better horizontal coverage, although the information on vertical structure is more limited than with limb sounding. Repeated observations at the same location, separated well in time during the Cassini tour, will define temporal variability on seasonal time scales.

4.4. Icy Satellites

During the Cassini tour, there are eight flybys of the classical icy satellites targeted at 1000 km or less, as well as a number of "Voyager-class" (<300,000 km) encounters. There are also flybys of several much smaller satellites, such as Janus and Epimetheus, at various distances. The dimensions of these objects range from less than 100 km to as much as 1530 km (Rhea). Consequently, it is most useful to discuss CIRS observations in terms of the angular diameter of the object, rather than its distance from the spacecraft (see Figure 22).

Normally the spacecraft orientation is controlled by momentum wheels, which provide pointing accuracy and precision of ∼2 mrad and ∼0.04 mrad, respectively. Consequently, the full spatial resolution of the FP3 and FP4 pixels (0.3 mrad) cannot be utilized with reasonable confidence until the target exceeds 1 mrad in

diameter. At that point, the separation between focal planes 3 and 4 (0.9 mrad), and the large size of FP1 (nominally 3.9 mrad) offer reasonable assurance of obtaining useful data in either FP1 or at least one of FP3 and FP4. As with the planet and the rings, the order of magnitude difference in FOV scale between FP1 and the other focal planes plays heavily in the design of the icy satellite observations. Approaching from a distance, CIRS observations might proceed roughly in the following order.

- *Compositional integrations*. These are typically performed at ranges where the target angular diameter (AD) is 1–3 mrad. Because spectral features of solid materials are generally broader than those of molecular lines, these observations are made at 1–3 cm^{-1} resolution. Conducted in staring mode, using FP1 and the center detectors of FP3 and FP4, these are concentrated in geometries with low phase angles, so as to view the icy satellite surfaces at their warmest and maximize the SNR. Due to the nature of the Planck function, there is a steep rolloff of thermal intensity with increasing wavenumber. This requires increasing integration time to extend the range of the spectrum. For a 100 K surface and a spectral resolution of 3 cm^{-1}, a SNR of 10 at 600 cm^{-1} can be obtained with one minute of integration, but extending the spectrum to 800 cm^{-1} with the same SNR requires integration of 100 min (Figure 29). Therefore, extending the spectrum to the highest wavenumbers will involve coadding spectra over the entire tour.
- *Eclipse observations.* Several passages of the satellites through Saturn's shadow will be observed at entry and exit. Typically AD $>$ 1 mrad, phase angle $\phi < 100^\circ$, $\Delta\nu = 15.5$ cm^{-1}, and the eclipse duration is $\sim$2 h. The high sensitivity of FP1 permits observations of objects even when the FOV is incompletely filled, or when the phase angle is moderately high. At low phase angles, even FP3 can be used to follow the initial portion of the cooling curve for relatively dark objects (Figure 23); this allows observations with body-centric spatial resolution better than 10° to be made when the apparent target size exceeds $\sim$3 mrad. Eclipses provide the thermal inertia of the upper mm or so of the surface, as well as estimates of surface coverage by relatively large fragments of consolidated material (Figure 24).
- *Phase/longitude (diurnal cycle) coverage* (AD $>$ 1 mrad, $\Delta\nu = 15.5\,cm^{-1}$, 10–20 min). Focal plane 1 will be utilized to determine the disk-averaged temperature of the satellites. From the resulting diurnal behavior, mean thermal inertias in the upper cm or so of the surface will be derived.
- *Global thermal inertia mapping and/or hot spot monitoring* (AD $>$ 3 mrad, $\Delta\nu = 15.5$ cm^{-1}). Maps are made by slewing and rastering FP3 and FP4 across the disk at rates not to exceed that for Nyquist sampling (16 μrad/s in blinking mode); observation durations will typically be 10–30 min. These maps will be successful for varying portions of a satellite, depending on its albedo, thermal inertia and phase angle. The exception is Enceladus, which is so cold that even the subsolar regions will be barely detectable in an individual measurement. In this case, mapping will serve to monitor the satellite for ongoing endogenic activity;

e.g., active sources at or above the $NH_3 \cdot H_2O$ eutectic temperature will be easily observed if they fill more than a few percent of an FP3 or FP4 pixel (Figure 23).

- *Search for a solid state greenhouse* (AD > 10 mrad, $\phi < 40^\circ$, $\Delta\nu = 15.5$ cm^{-1}, 15 min). In the far-IR the decreasing absorption coefficient of water ice with decreasing wavenumber permits detection of radiation from increasingly far below the surface, reaching as deep as 1 cm at 10 cm^{-1}. Slow east-west slews using FP1 allow following the gradual penetration of the thermal wave into the regolith throughout the day.
- *Polar night (annual cycle) coverage* (AD > 10 mrad, $\Delta\nu = 15.5$ cm^{-1}, 15 min). FP1 observations of the dark winter polar region from high latitude permit determination of the seasonal cooling curve. This enables an estimate of thermal inertia in the upper tens of centimeters of the polar regolith.
- *High-resolution hemispheric FP1 mapping*, near closest approach (AD > 10 mrad, $\Delta\nu = 15.5$ cm^{-1}). The high sensitivity of FP1 permits rapid mapping of satellite disks near closest approach, where time is at a premium. Nyquist-sampled maps at low spectral resolution (slew rate 420 μrad/s) will typically take 10–30 min. These permit identification of minor thermal anomalies, even on the night hemisphere, as for example, revealed for Europa from Galileo Photopolarimeter measurements (Figure 26).

4.5. Saturn's Rings

The 4-year Cassini tour has three distinct intervals of inclined orbits which are of primary interest for ring science (Cuzzi *et al.*, 2002; Matson *et al.*, 2002; Wolf, 2002). The early inclined sequence, which begins about 9 months into the tour, catches the rings close to their maximum opening angle, and near their warmest. These orbits reach a maximum inclination of about 20°. This sequence is followed by almost a year with the spacecraft orbiting in Saturn's equatorial plane. This time is good for edge-on ring measurements, primarily of the faint rings. The Titan 180° transfer sequence begins about two years into the tour. This sequence has two stages, an "up-leg" where the orbit inclination is increasing, and a "down-leg", where the orbit inclination is decreasing. The maximum inclination in this sequence is about 50°. A few months later the final, high inclination sequence begins. The spacecraft ends the 4-year tour in a high-inclination orbit (about 75°) with periapse on the lit side of the rings. This time provides a unique, high-inclination view of the rings.

SOI. The short period of time immediately following the Saturn Orbit insertion burn is of key interest for CIRS ring science. The spacecraft soars over the unilluminated side of the main rings and is nearly an order of magnitude closer to the rings than it will be at any other time in the mission. A single scan of a portion of the main rings will be obtained at 15.5 cm^{-1} resolution. CIRS FP1 resolution will range from 100 to 250 km, and FP3/4 resolution will range from 8 to 19 km, with the highest resolution over the A ring.

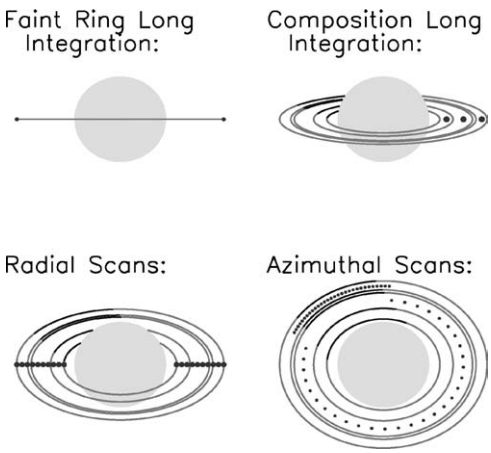

Figure 32. CIRS observations of Saturn's rings as a function of spacecraft elevation. Typical CIRS ring observations are depicted as a function of the observed ring opening angle.

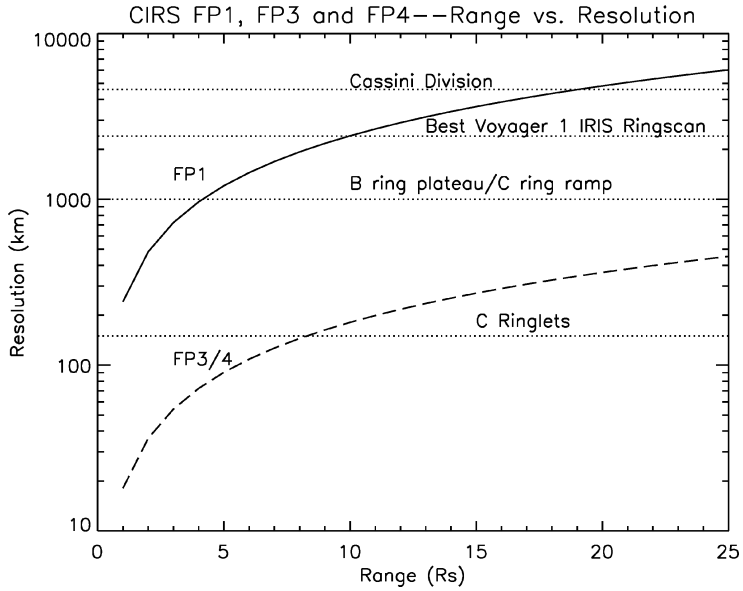

Figure 33. CIRS FP1 and FP3/4 spatial resolution as a function of distance from the rings. The spatial resolution for FP1 and a single pixel in FP3 or FP4 are shown as a function of the distance from the rings, for normal ring viewing. The curves above also depict the ring radial resolution when viewing the rings at either ansa. For comparison, the radial extent of ring features such as the Cassini Division, B ring plateau/C ring ramp, and C ringlets are indicated.

The main types of CIRS ring observations are listed below, in order of increasing spacecraft elevation. A schematic of these observations is shown in Figure 32. Typical ring radial resolution for focal planes FP1 and FP3/4 as a function of distance from the rings is shown in Figure 33.

- *Faint ring long integrations.* The low optical depths of the faint D, E, F and G rings will pose particular observing challenges for CIRS. These rings are best viewed edge-on because this geometry enhances the fill factor of the instrument field of view. Low spectral resolution of 15.5 cm^{-1} with FP1 provides the best signal-to-noise and should be sufficient for detecting the variations of emissivity with wavelength, which is our primary measurement goal. From close range ($\sim$10 R_S) and small opening angle, the FP1 filling factor will approach 1% when pointed at the F ring's ansa. Integrations of $\sim$10 min should yield usable signals. However, because the F ring is so clumpy, it needs to be sampled at many longitudes before a truly representative spectrum can be obtained. Observations will consist of alternating between both ring ansae every $\sim$30 min to achieve the most complete rotational coverage of this ring. The E ring will be observed by pointing FP1 near the orbit of Enceladus, where the long edge-on line of sight through the ring maximizes the fill factor. However, this fill factor will still remain quite low, $\sim 10^{-4}$, so, detecting the E ring will require many, perhaps 100 or more, hours of integration. On the other hand, because the ring is so thick vertically, the observing range can be quite large (30–40 R_S). More observing time is available then during these apoapse periods of the tour. The VIMS and UVIS instruments will also require substantial integration on this ring, so E ring observations will be cooperative activities between all of Cassini's optical remote sensing instruments. Unfortunately, the best possible fill factors for the remaining rings, D and G, are still lower than for Ring E. It is unlikely that either will be detected with CIRS.
- *Composition integrations.* CIRS will determine with unique accuracy the ring spectrum between 50 and 1000 μm. As intimately mixed contaminants significantly influence this part of the spectrum, mixtures derived from the visible and near-infrared spectra will be tested against this new spectrum. Spectra of the three main rings over the full CIRS wavelength range will be obtained to determine possible radial variations in the bulk composition. Two types of observations will be made: high spectral resolution (0.5 cm^{-1}) FP3 emission measurements of the A, B and C rings, and high spectral resolution transmission measurements of the rings with the rings against Saturn. The former can be obtained from large ranges 20–40 R_s because of FP3's fine spatial resolution; long integrations of 10–20 h will be obtained on representative radial locations in each ring. The transmission measurements will be made from 20 R_s at relatively low ring opening angles. This will allow a search for absorption features in the A and C rings, and the Cassini division. The same region of Saturn will be observed in at a similar spatial resolution when the rings are not present, to establish the background. The transmission spectra will be obtained over a series of emission angles.
- *Stellar occultations.* A handful of stellar occultations are observed by CIRS to directly obtain the ring opacity in the infrared. Only a limited number of targets are observable by CIRS, including CW Leo and Eta Carinae. Eta Carinae occultations are only observable during the final month of the tour. Occultations are observed

in one FP3 pixel (CW Leo) or one FP4 pixel (Eta Carinae) at 15.5 cm^{-1} spectral resolution.

- *Radial scans*. These scans are typically executed between 5 and 20 R_s over a range of spacecraft inclinations, from low (5°) to highest possible inclination (75°). Radial mapping (FP1, FP3) of the rings, on both lit and unlit sides, over a range of spacecraft elevations, local times and phase angles, is performed to obtain broadband radiometric measurements of the total flux and spectral shape in the CIRS wavelength range. Sets of observations are obtained in each of the inclined orbit intervals to map the temperature variation in the rings with changing solar illumination. Two types of scans are planned. Temperature scans will consist of spectra taken at 15.5 cm^{-1} spectral resolution of the lit and unlit sides of the rings at many incidence and emission angles and provide prime information on the ring thermal gradient as a function of radial distance to Saturn. Submillimeter scans will be made of spectra at 1 cm^{-1} spectral resolution of the lit and unlit sides of the rings to map the thermal characteristics and composition of the ring particles out to 1 mm.
- *Azimuthal scans.* These observations are executed between 5 and 20 Rs at spacecraft inclinations greater than 20°. They will be used to study the surface properties, the vertical dynamics, and the spin of ring particles. Observations of the cooling and heating of the ring particles entering and emerging from the planetary shadow are planned to derive particle thermal inertias for all three main rings. Measurements at moderate radial resolution (typically 1000 km) across the shadow boundaries at low spectral resolution (15.5 cm^{-1}) with the FP1 FOV. To constrain the vertical dynamics of ring particles, the temperatures of the main rings will be measured by CIRS along the azimuth of the main rings, from the exit of the shadow (morning) to the evening ansa, both on the unlit and unlit faces. This unique experiment will be realized with spectra at low spectral resolution (15.5 cm^{-1}). Spins create both an azimuthal asymmetry in the ring temperature and a dependence of the temperature with the emission angle, due to day/night contrast. Circumferential scans at a variety of phase and emission angles will be executed to detect azimuthal asymmetries and the anisotropy in the ring particle emission function which are both function of particles spin and thermal inertia. Occasionally, when observing time is highly disputed, long azimuthal scans (8–20 h long depending on geometry and face) will be replaced by a series of radial scans at different azimuths.

There are other types of joint observations as well. Combined data from CIRS and VIMS, over a wide range of geometric and illumination conditions, will define the interior thermal distribution, from which a density distribution within the particles can be estimated. The thermal inertia and the infrared optical depth will be derived, which will provide information on regolith density, and possibly on collisional processes. The determination of the interior thermal distribution relies on the opportunities afforded by the orbiter and the semi-transparency of the ring

particles at submillimeter wavelengths. Information about the particle interiors will be obtained by long spectral averages at various locations in the rings with spatial resolutions from a few hundred to several thousand km. These observations will be taken at many incidence and emission angles over the mission.

5. Instrument Description

5.1. Overview

The CIRS instrument consists of the Optics Assembly (OA), Electronics Assembly (EA), and an interconnecting External Harness (EH). A photo of the CIRS Engineering Model (EM) on the Remote-Sensing Platform (RSP) is shown in Figure 34; the EM has the telescope cover off while undergoing ground optical boresight tests. The CIRS instrument evolved from the Voyager Infrared Interferometer Spectrometer (IRIS) (Hanel *et al.*, 1979), a single infrared interferometer covering the 180–2000 cm^{-1} (56–5 μm) region with an apodized spectral resolution of 4.3 cm^{-1}. IRIS had a single thermopile detector with a 4.4-mrad diameter field of view (FOV). The CIRS instrument consists of two combined interferometers, operating in the far-infrared (10–600 cm^{-1}) and mid-infrared (600–1400 cm^{-1}) with a commandable apodized spectral resolution as high as 0.5 cm^{-1}. The two interferometers share a common telescope and scan mechanism. The far-IR interferometer is a polarization interferometer, with a focal plane (labeled FP1) consisting of two thermopile detectors with a 3.9 mrad FOV. The mid-IR interferometer is a conventional Michelson interferometer with two focal plane arrays (FP3, FP4), each having 10 HgCdTe detectors, with 0.273 mrad FOV per pixel. (An additional focal plane, FP2, was eliminated in a Cassini downsizing). Table I summarizes the instrument characteristics. Kunde *et al.* (1996) provide a more complete engineering description of the instrument.

5.2. Optics Assembly

The OA consists of the beryllium telescope, relay optics, scan mechanism, two infrared interferometers, a reference and white-light interferometer, an 80 K passive radiator cooler, an instrument radiator, and detectors.

5.2.1. *Optical Design*

Figure 35 illustrates the conceptual design of CIRS. Infrared radiation is focused by the telescope on a field splitting mirror, which divides the incident beam between the far-IR and mid-IR interferometers. In each interferometer, fore-optics collimate the beam and pass it through a beamsplitter and retroreflectors. In both interferometers, one retroreflector is fixed and the other is attached to the scan mechanism. After the beamsplitters, the recombined output beams go to the focal planes and are focused on the detectors. A reference interferometer provides servo signals for the

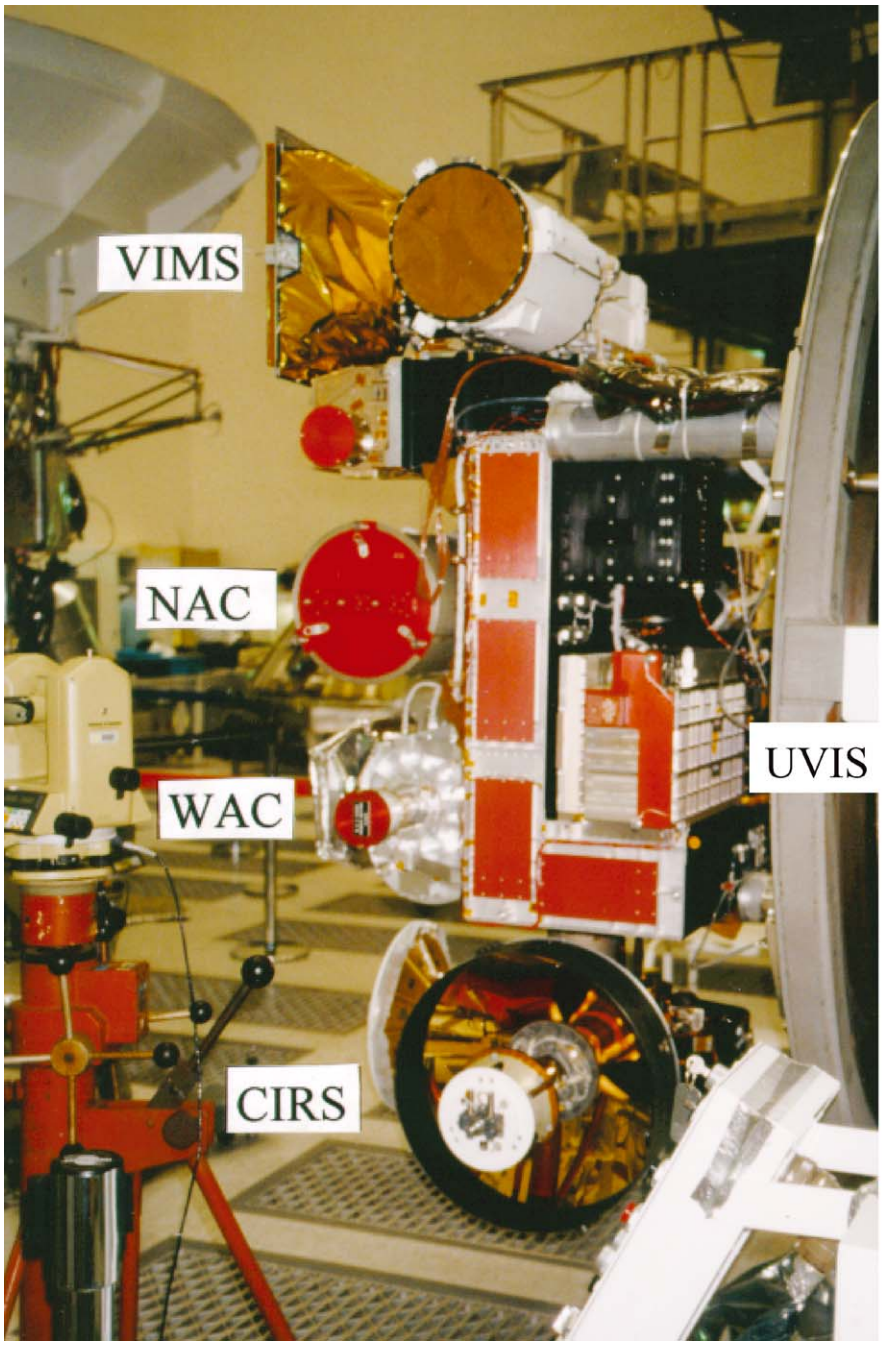

Figure 34. CIRS on the Cassini Optical Remote Sensing Pallet.

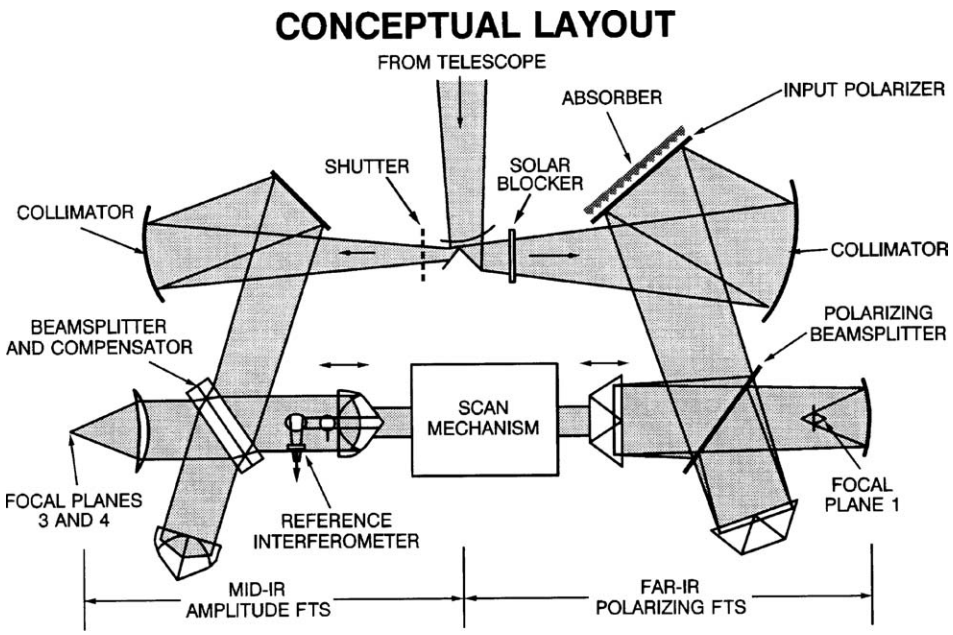

Figure 35. CIRS conceptual layout. Radiation from the telescope is field-split between the mid-IR and far-IR. interferometers. The moving retroreflectors share a common drive mechanism.

scan mechanism to maintain a constant velocity and to control data sampling. The reference interferometer uses the same moving retroflector as the mid-IR interferometer in order to track the motion of the mechanism. The instrument, telescope and FP1 are operated at a temperature of 170 K. FP3 and FP4 are mounted on a passive cooler radiating to space, and are operated near 80 K (typically in the range 75–80 K).

A brief description of the major optical subsystems follows:

Telescope. The CIRS Cassegrain telescope is identical in size to the Voyager IRIS telescope, with an improved optical quality. It provides a large aperture, small field-of-view, and minimum volume. The telescope consists of a 50.8-cm F/6 paraboloidal primary mirror and 7.6 cm diameter hyperboloidal secondary mirror. A cylindrical tube extends from the central portion of the primary mirror to support the secondary mirror. The mid-IR FOV is centered on the telescope axis (see Figure 1) to provide good image quality for the FP3 and FP4 arrays. The central obscuration of the telescope is 41%. The primary and secondary each has its own sunshade/radiator.

Fore-optics. An entrance aperture plate, located at the telescope focus, directs the incoming radiation into the two infrared interferometers. There are two field stops at the exit focal plane of the telescope, corresponding to the fields-of-view of the two interferometers. The center of the mid-IR field stop is coincident with the telescope axis. The axis of each interferometer is aligned with its respective field stop. Between each field stop and its interferometer is a field splitting mirror,

a collimator, and a folding flat. The mid-IR fore-optics has a mechanical shutter which can be commanded to block the beam for calibration. The far-IR beam passes through a solar blocking filter, which rejects wavenumbers short of 600 cm^{-1} to protect the thermopile detectors against accidental solar illumination. A polarizer acts as the folding flat in the far-IR. To minimize the sizes of beamsplitters and mirrors, the fore-optics are arranged to place the pupils (images of the primary telescope mirror) at the retroreflectors in the two interferometers.

Infrared interferometers. The far-IR and mid-IR interferometers provide complete coverage of the 10–1400 cm^{-1} range, with an apodized resolution as high as 0.5 cm^{-1}. The far-IR interferometer uses polarization modulation, produced by mylar mounted wire grid polarizers, to provide coverage of the 10–600 cm^{-1} region. The mid-IR interferometer is a conventional Michelson using a KBr beamsplitter, covering the 600–1400 cm^{-1} range. The far-IR and mid-IR interferometers use two types of retroreflectors. Cube corners are used in the mid-IR to provide tilt compensation during scanning and to minimize misalignment at 170 K. Dihedral mirrors are used in the far-IR to rotate the beam polarization by 90° before returning it to the beamsplitter (so that the transmitted/reflected incoming beam is reflected/transmitted toward the detector).

Reference interferometer. A reference interferometer, using a 785 nm (@170 K) diode laser, shares the mid-IR moving retroreflector and provides a servo signal for velocity control. The reference interferometer also produces a white-light fringe just before the start of scan to initiate sampling.

Focal planes. Radiation exiting the interferometers is focused on the detector focal planes with a germanium lens (FP3, FP4) and an on-axis mirror (FP1). The focal-plane detectors are discussed in detail below.

5.2.2. *Fields of View*

Figure 1 summarizes the locations of the CIRS focal planes in the plane of the sky. These were obtained from several scans of Jupiter and bright infrared stars, which were made in April to October, 200l, after the Jupiter swingby (closest approach: December, 2000). Over this period, Jupiter's diameter, viewed from the spacecraft, decreased from 1.24 mrad to 0.48 mrad. In May, 2002, another set of scans was made across Jupiter, when its angular diameter was 0.290 mrad, to determine the spatial response of FP1. This is discussed in Appendix B. A final set of scans will be made in May, 2004, when Jupiter subtends 0.114 mrad, to determine the spatial response of each pixel in FP3 and FP4.

5.2.3. *Far-IR Interferometer*

The far-IR interferometer operates on the principle of polarization modulation introduced by Martin and Puplett (1969), and Martin (1982). The interferometer operates by first polarizing the radiation and then modulating its polarization. The beam entering the interferometer is linearly polarized by an input polarizer. At the beamsplitter polarizer, which is oriented at 45° with respect to the input polarizer,

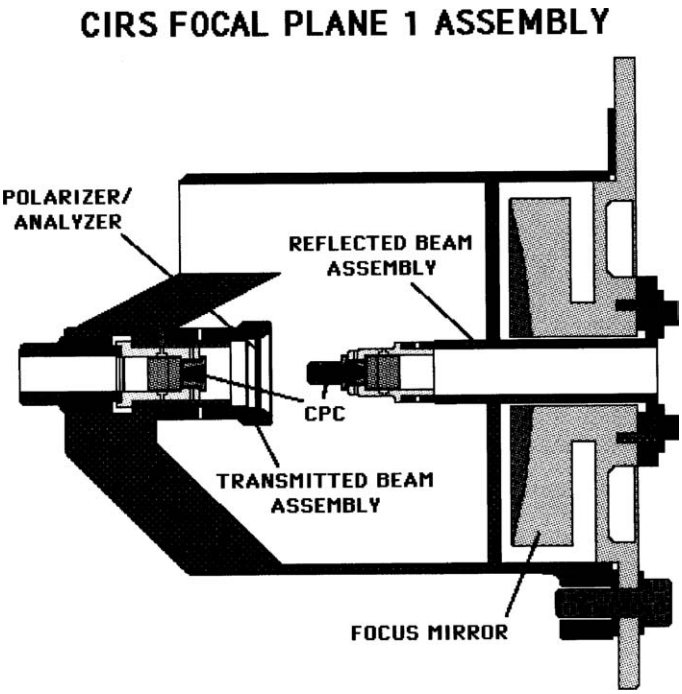

Figure 36. CIRS far-IR FP1 assembly, consisting of the focusing mirror and mechanical structure supporting the thermopile detectors and polarizer/analyzer.

the beam is further split into two orthogonal components. These are sent to the two retroreflectors, rotated 90°, and returned to the beamsplitter. A phase difference between the two components is introduced by the path difference between the two arms. The beams are recombined at the beamsplitter and sent to the focal plane. The recombined beam is elliptically polarized and its instantaneous state of polarization switches between two orthogonal linear states as the moving mirror is scanned. These are selectively transmitted (and reflected) by the polarizer/analyzer, located in front of the detectors. The detector signals are therefore modulated, and the modulation frequency is proportional to the wavenumber (cm^{-1}) of the radiation. The result is a conventional interferogram.

The beam from the interferometer is focused by an on-axis parabolic mirror (f/1) at the entrance of a compound parabolic concentrator (CPC) located in front of each thermopile detector (see Figure 36). Prior to reaching the CPC's, the beam is split by the polarization analyzer. The transmitted polarization component is detected by one thermopile detector and the reflected polarization component is detected by the other thermopile detector. The use of two detectors gives a gain in signal, eliminates unmodulated intensity fluctuations, and provides redundancy.

The polarizing interferometer (10–600 cm^{-1}) uses substrate-mounted wire-grid polarizers to split, recombine, and analyze the radiation. This technique takes

advantage of the existence of nearly ideal wire-grid polarizers for the far infrared to make an instrument with high efficiency and broad frequency response. The CIRS wire grids (input polarizer, beamsplitter, output analyzer) are 1-μm diameter wire, with 2-μm spacing, supported by a thin (1.25 μm) film of Mylar. These grids give good efficiency from 10 to 600 cm^{-1}. The grids were designed and developed at Queen Mary and Westfield College, London, England.

5.2.4. *Mid-IR Interferometer*

The MIR interferometer (600–1400 cm^{-1}) is a conventional Michelson design. The beamsplitter is a potassium bromide (KBr) substrate with a multiple-layer coating including a layer of germanium, an antireflection coating, and protective coatings. A matched compensator is placed adjacent to the beamsplitter to correct for refractive effects in the substrate. The beam coming from the collimator is divided equally at the beamsplitter, and the two halves are sent to the fixed and moving retroreflectors. The beams are reflected back to the beamsplitter, where they are recombined and sent to the focal planes. The beam is imaged by a Ge lens on the FP3 and FP4 HgCdTe detector arrays, which are mounted on the 80 K cold stage. As the moving mirror is scanned, the path difference between the two beams is varied, which modulates their interference and, therefore, the detected intensity. The modulation rate is proportional to the spectral wavenumber, and the total modulated signal at the detector creates the recorded interferogram. The detector arrays are mounted on a common carrier, and are rigidly mounted to the 80 K cooler using a tripod of titanium alloy supports. A cold shield limits out of field background radiation from the warm instrument onto the arrays.

5.2.5. *Reference Interferometer*

The reference interferometer generates a signal for sampling the detector outputs from the far-IR and mid-IR interferometers. Sampling of the interferograms takes place at zero crossings of equally spaced reference fringes. This signal is also used in a phase-locked loop to control the velocity of the scan mechanism. The reference interferometer uses the central portion of the mid-IR optics and beamsplitter, and is constrained by the envelope of the central obscuration shadow of the mid-IR interferometer. The source for the reference interferometer is a solid state GaAlAs laser diode operating in the red region (811 nm at room temperature, 785 nm at 170 K). For redundancy, two laser diodes are available, selectable via command. Due to dependences on operating temperature and viewing geometries, the monochromatic emission source can provide only a short-term wavenumber calibration standard for the interferometer. The long-term standard is well-characterized molecular lines, H_2O and NH_3 in FP1, C_2H_2 and C_2H_6 in FP3, and CH_4 in FP4.

The zero path distance (ZPD) must be located in each interferogram to facilitate co-adding of interferograms in flight, in order to lower the CIRS telemetry data rate. For this purpose a white light interferogram must be produced so that the ZPD point can be located consistently from scan to scan. The source for the white light

interferometer is a Light Emitting Diode (LED), with a center wavelength of 870 nm, and a full width at half max of 70 nm. The white light shares the reference interferometer with the laser.

5.2.6. *Detectors*

The detectors used in CIRS were chosen to maximize sensitivity in each wavelength range for the achievable operating temperatures. Thermopile detectors (FP1) give optimum performance in the far-infrared at 170 K. HgCdTe detectors (FP3 and FP4) can be tailored for highest performance near 80 K in the 7–16 μm range.

Far-IR: Thermal detectors. The most important properties of a thermal detector are high sensitivity, a short response time and low excess noise. High sensitivity is achieved by having maximum absorptance in the absorbing element. The short response time is achieved by having a small heat capacity of the absorbing layer. Low excess noise is achieved by operating a thermoelectric detector without external bias. A thermopile detector consists of two elements, an absorber to convert infrared photons into heat, and a thermoelectric element that produces a voltage proportional to its internal temperature gradient. The cold side of the thermoelectric material is thermally sunk to a heat reservoir, and the hot side is attached to the radiation absorber.

Mid-IR HgCdTe arrays. The detectors for FP3 are a 1×10 linear array of photoconductive (PC) HgCdTe elements operating near 80 K. The FP3 array was fabricated for a 15.7 μm cut-off wavelength to optimize response in the 9–16 μm range. The detectors for FP4 are a 1×10 linear array of photovoltaic (PV) HgCdTe elements operating near 80 K. The FP4 array was fabricated for a 9.4 μm cut-off wavelength to optimize response in the 7–9 μm range. The use of a photovoltaic array allows a much lower bias-induced power dissipation, lessening the demand on the radiative cooler. The noise level for the photovoltaic array is also lower, due to its relative lack of 1/f noise.

Five signal channels are available for each of the FP3 and FP4 10-element arrays. Therefore, only five detectors, or five paired detectors, are used in each observation. Four patterns of detectors – all even, all odd, center five or five pairs – are selected by scripted commands.

5.2.7. *Thermal Control*

The CIRS optics assembly is passively cooled, and actively controlled to operate at 170 ± 0.1 K for short time periods, with a maximum allowable drift of ± 0.1K/day. This temperature is achieved by thermally isolating the instrument from the warmer spacecraft scan platform by a titanium mount, and by using thermal radiators to cool the instrument and FP1 detectors by radiating to deep space. Three control regions are monitored and controlled at 170 K: the telescope primary, telescope secondary, and instrument housing. The temperature at each of the control points is controlled by silicon diode thermistors. The temperature controller circuit power amplifies an

error signal and applies it to heater strips that warm the control point back up to 170 K. To minimize heater transient effects on the infrared signal, proportional heaters are used.

In addition to the thermal control heaters, the instrument also contains decontamination heaters. These high-powered heaters are command controlled, and are capable of increasing the instrument temperature to 270 K, and the cooler temperature to 300 K. They serve to drive off contaminants that might condense on the cooled optics and detectors.

5.3. Electronics Assembly

The analog and digital circuitry resides in a module outside the OA. Exceptions to this are preamplifier electronics, which must be close to detectors to minimize noise, and thermal-control sensors. The CIRS electronics assembly includes electronics for: (1) conditioning spacecraft power for electronics subassemblies; (2) communicating with the spacecraft, and processing of commands, science data and housekeeping data; (3) temperature control and temperature monitoring of the optics subassemblies; (4) operating and controlling the scan mechanism; (5) operating and controlling the science data sampling; and (6) processing the detector signals.

An instrument microprocessor provides instrument operation, on-board data processing, and communication with the spacecraft central computer. The signal handling and on-board processing are designed to minimize both the data rate and data volume. The data rate is minimized by tightly bandlimiting each signal by numerical filtering, and then resampling the numerical filter output at a reduced rate. The data volume is minimized by compressing the interferograms through efficient encoding. The dynamic range is high near zero path difference, and significantly lower in the wings of the interferogram. This allows the bits/word to be reduced in the wings. The on-board data processing for CIRS is performed under software control. CIRS is able to downlink individual interferograms, and summed pairs of sequential interferograms. The microprocessor carries out the functions of command and control, instrument operation, signal handling, and data compression/packetization.

5.4. 80 K Cooler

The FP3 and FP4 detector (HgCdTe) temperature is controlled with a single-stage passive cooler radiating to space. The temperature may be set via ground control to temperatures at discrete set points between 75 and 85 K, depending on the amount of backload present on the cooler from Saturn or its rings. The cooler is sized to drive the focal plane temperature below the selected set point, and control heat is supplied to stabilize the temperature at the set point. Temperature control is carried out with silicon diode sensors and thermostatic heaters. Calcutt *et al.* (1992) provide a preliminary discussion of the cooler design. The focal plane is rigidly

attached to the instrument, rather than to the cooler, which helps maintain optical alignment between the mid-infrared interferometer and the arrays through vibration and thermal cycling. The cooler cold stage supports the two HgCdTe arrays. The radiating cold panel is an aluminum honeycomb painted with electrically conductive black paint. The radiator panel is supported by a titanium cone-shaped housing. This is held by an aluminum tube, which surrounds the focal plane and forms the interface with the OA. The arrays are cooled via an aluminum alloy cold finger and a conductive strap from the cold finger to the arrays, which allows the cold finger to shift with respect to the instrument. A deployable aperture cover protected the cooler during launch and early cruise, and was jettisoned when the spacecraft was 2 AU from the sun.

5.5. Interferogram Processing

After the data are received on the ground, the interferograms are edited and transformed into calibrated spectra. Steps in this process include eliminating bad scans, removing predicted noise patterns, calibrating, apodizing, and Fourier transforming. Algorithms remove interferograms that have anomalous intensities and adjust interferogram lengths for uniformity. Known noise patterns are removed from the interferograms. Calibration is performed using deep space and internal shutter reference interferograms. The calibration uses untransformed interferograms and complex spectra, so that phase correction is an intrinsic part of the process. The interferograms are apodized (using a Hamming function) and Fourier transformed to produce calibrated spectra. A version of the spectra is also created without apodization.

5.6. In-Flight Radiometric Calibration and Sensitivity

The basic approach for the calibration of the CIRS measurements to absolute radiance units follows the calibration techniques developed previously for thermal emission interferometers (Hanel *et al.*, 2003; Hanel *et al.*, 1980; Revercomb *et al.*, 1988). Appendix C describes the calibration equations in detail. In-flight calibration of FP1 will be performed by periodically viewing deep space. FP3 and FP4 are calibrated by viewing deep space and an internal shutter at 170 K. The spectra amplitudes of the planetary spectra are scaled, at each wavenumber, to the amplitudes of the calibration targets. The detectors and electronics are designed to be linear at all wavenumbers with respect to the incoming radiance, a necessary condition for scaling the target spectra from the calibration spectra.

5.6.1. *In-Flight Sensitivity – NESRs*

The NESR is the signal for which the SNR is unity (Hanel *et al.*, 2003). In-flight instrument responses and NESRs have been determined from in-flight calibration

data obtained during cruise. Detailed results will be reported elsewhere. The NESRs are calculated from noise changes observed in consecutive scan to scan interferograms. The standard deviation in response, σ, is calculated from the individual responses included in each average. This noise level includes random noise from detectors, scan-to-scan changes, and systematic noise from thermal drifts, etc. The NESR is calculated from:

$$NESR(\nu) = a\frac{\sigma[R(\nu)]}{R_{\mathrm{Avg}}(\nu)}B_{\mathrm{r}}(\nu) \tag{7}$$

where $R_{\mathrm{Avg}}(\nu)$ = the average of K measurements of the response, $R(\nu)$; $\sigma[R(\nu)]$ = the standard deviation of the response:

$$\sigma[R(\nu)] = \sqrt{\frac{\sum_{i=1}^{K}[R_i(\nu) - R_{\mathrm{Avg}}(\nu)]^2}{K-1}}. \tag{8}$$

B_{r} is the Planck function at 170 K. FP1 is at the same temperature as the interferometer, so only deep space is required for the calibration (Appendix C). B_{r} corresponds to the instrument self-emission, and $a = 1$ (Hanel *et al.*, 2003). For FP3 and FP4, the detectors are at a different temperature than the interferometer, and observations of a warm target (the detectors' view of the instrument with the shutter closed) and of deep space are both required for the calibration (Appendix C). In this case B_r corresponds to the 170-K warm target, and $a = 1/\sqrt{2}$ (Hanel *et al.*, 1970).

The in-flight spectral responses and NESRs are shown in Figure 37. These responses cover the free spectral bandpass, which is the spectral region not affected by aliasing. Instrument "set points" are available to raise the FP3 and FP4 focal planes temperature above their nominal 76.4 K. These can be used to avoid calibration drifts that may result when the cooler is briefly exposed to the sun or Saturn during operations. However, an increase in focal plane temperature of 1 K causes an increase in the NESR of roughly 4%. The choice between sacrificing stability or SNR must be based on the objective of the observations affected.

5.6.2. *Long-Term Stability*

The CIRS temperature is maintained within 0.1 K (Section 5.2.7). Such a temperature excursion changes the uncalibrated detector signal due to changes in the instrument self-emission and also in the response term (Appendix C). The process of calibration removes these changes. Beyond these reversible short-term, temperature-driven changes, there remains the issue of possible long-term change or degradation, perhaps from contamination of optical surfaces, radiation damage, shift in optical alignment from stress relaxation, or detector degradation. In fact, CIRS appears to be quite stable once the short-term changes are accounted for. Observations of deep space made over two years, beginning with the telescope cover release in September, 2000, (3 months before the Jupiter swingby closest

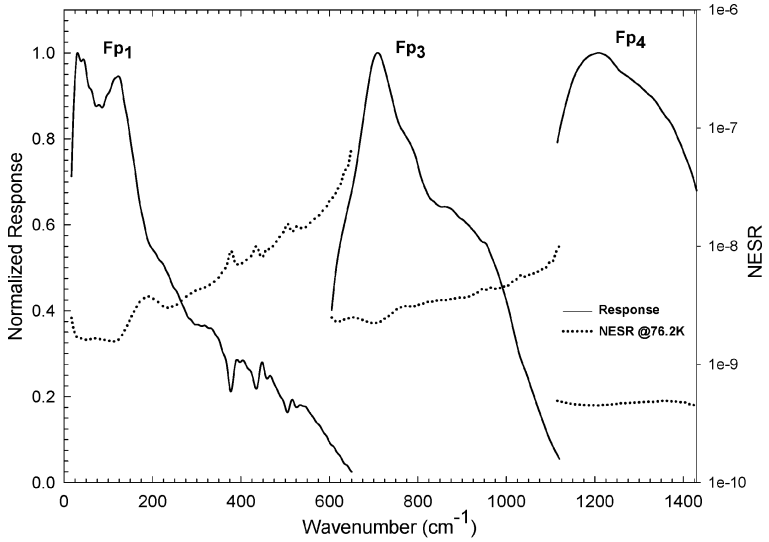

Figure 37. Spectral responses and NESRs for the three CIRS focal planes at a spectral resolution of 15.5 cm^{-1}. The FP3 and FP4 curves represent the average of the 10 detectors in each array, with each detector being within 20% of the average. The FP3 and FP4 NESRs correspond to a focal plane temperature of 76.2 K.

approach) show a cumulative decline in the mean FP1 signal level that is no larger than 0.5% (Brasunas and Lakew, 2003).

Acknowledgments

We thank M. H. Elliot, J. S. Tingley, F. Carroll, S. Albright, S. Pilorz, and B. Wallis for their continuing support in the investigation science planning and operations, and P. J. Schinder for his assistance in setting up the CIRS database architecture.

Appendix A: Retrieval of Atmospheric Parameters

Because CIRS measures thermal infrared emission, the measurements in a given spectral region will depend on both the atmospheric temperature and the abundances of the atmospheric constituents that are optically active in that region. The radiance I_ν observed at wavenumber ν is given by

$$I_\nu = \int_0^\infty B_\nu(T) \frac{\partial \tilde{\mathrm{T}}}{\partial \mathbf{x}} \cdot d\mathbf{x}, \tag{A.1}$$

where B_ν is the Planck function at wavenumber ν, T is temperature, $\tilde{T}$ is the transmissivity, and $\mathbf{x}$ is the coordinate measured along the line of sight from the

observer to the portion of the atmosphere being observed. In the far- and mid-infrared, B_ν is a strong function of temperature, while $\tilde{T}$ primarily depends on the amount of absorber along the path length, with a weaker dependence on T. The retrieval of parameters within a given portion of the atmosphere requires the independent determination of temperature for that part of the atmosphere, either from the spectra or from an independent source.

Figure 2 illustrates the two types of observing geometry, nadir and limb viewing. In nadir viewing, atmospheric pressure and absorber mass increases along the line of sight until the surface is reached or else the local contribution to the observed radiance becomes negligible. In limb viewing the line of sight passes through the atmosphere, and deep space is the background; pressure increases along the line of sight to the tangent point and decreases beyond, while the absorber mass continues to increase monotonically. In nadir sounding there is no direct information on the dependence of the atmospheric parameters with the coordinate **x**, and the optical depth is determined by the integrated number density of the absorber along the line of sight to a given pressure level. In this situation it is more straightforward to use pressure P as the vertical coordinate and rewrite (A.1) as

$$I_\nu = -\int_0^\infty B_\nu(T)\frac{\partial \tilde{\mathrm{T}}}{\partial \ln P} d\ln P, \tag{A.2}$$

The viewing geometry is implicitly contained in the transmissivity, which depends both on the vertical distribution of the absorber, and the viewing angle along the line of sight with respect to the local vertical direction. Equation (A.2) formally holds even when surface contributions matter, as they do over certain wavenumber intervals on Titan; one then includes delta functions at the surface pressure P_S within the integral. Alternatively, (A.2) can be expanded:

$$I_\nu = -\int_0^{P_S} B_\nu(T)\frac{\partial \tilde{\mathrm{T}}}{\partial \ln P} d\ln P + B_\nu(T_S)\tilde{\mathrm{T}}_S, \tag{A.3}$$

where T_S is the surface temperature, $\tilde{\mathrm{T}}_\mathrm{S}$ is the transmissivity along the line of sight to the surface, and the surface emissivity is assumed to be unity. The retrieval of temperature and composition profiles from (A.1) is generally an ill-posed problem, and solutions tend to be unstable unless structure at small spatial scales, which is dominated by instrument noise, is filtered out. Physically, this means that the profile information contained in the measurements is limited to relatively large vertical scales. Several general retrieval algorithms that introduce appropriate filtering, either explicitly or implicitly, are available (see, e.g., Craig and Brown, 1986; Hanel *et al.*, 2003; Rodgers, 2000).

Similar considerations apply to the inversion of limb-viewing spectra, but in this case one has additional information because of the viewing geometry, namely the dependence of the radiance on the tangent point altitude of the central ray within the FOV. Retrieval of both temperature and pressure at a given altitude is possible, because the spectrum typically has several wavelengths at which the optical depths

to the tangent point are ≤ 1, but with different relative sensitivities to T and P (see, e.g., Gille and House, 1971). In practice, the absolute dependence of pressure on altitude is not precisely established, because of the inevitable errors associated with knowledge of the pointing of the instrument FOV during the measurements. However, the pressure-altitude relation is well determined relative to an arbitrary reference level, by application of the hydrostatic balance equation.

Conrath *et al.* (1998) and Conrath and Gautier (2000) discuss the retrievals of temperature (as well as the para fraction of H_2 and the He abundance) for the outer planets from Voyager IRIS nadir-viewing spectra. Inversion of (A.2) typically entails the assumption that horizontal variations in atmospheric variables are small within the FOV. The sensitivity of the measured spectrum to the temperature at various atmospheric levels can be examined by assuming a reference temperature $T^{(0)}(P)$ and computing the radiance spectrum $I_\nu^{(0)}$, assuming that the sources of opacity are known. Neglecting the temperature dependence of $\tilde{\mathrm{T}}$, linearization of (A.2) gives

$$\delta I_\nu = -\int_0^\infty \frac{dB_\nu}{dT}\frac{\partial \tilde{\mathrm{T}}}{\partial \ln P}\delta T\, d\ln P \equiv \int_0^\infty K\,\delta T\, d\ln P, \tag{A.4}$$

where $\delta I_\nu = I_\nu - I_\nu^{(0)}$ and $\delta T = T - T^{(0)}$; K is the kernel for the retrieval problem, and it depends both on the derivative of the Planck function with respect to temperature and the derivative of the transmissivity with respect to $\ln P$. Similar considerations can be applied to the limb-viewing geometry.

The success of a temperature retrieval depends on the knowledge of opacity sources. For Saturn, the principal gaseous opacities used in temperature retrieval are H_2 and CH_4. Figure 4 depicts the kernels, normalized to a maximum value of unity, with respect to absorption in the collision-induced S(0) and S(1) lines and the translational continuum of H_2 ($\nu < 600\ \mathrm{cm}^{-1}$) and the ν_4 vibrational-rotational band of CH_4 ($\nu \sim 1300\ \mathrm{cm}^{-1}$). Both nadir- and limb-viewing geometries are included. In the latter, the repetition of wavenumbers indicates that several tangent heights are being used. The Voyager IRIS observations were mostly done in the nadir-viewing mode, corresponding to the kernels on the left-hand side. In the spectral region dominated by collision-induced H_2, the opacity is a function of the height-dependent ratio of ortho to para hydrogen as well as the He/H_2 ratio. Since both the temperature and ortho-para profiles are expected to vary with position on the planet, it is necessary to retrieve both parameters simultaneously. This is possible because there are multiple spectral intervals that sound the same atmospheric levels but have different relative sensitivities to temperature and the ortho-para ratio (Conrath *et al.*, 1998). In the initial analysis of Voyager data, IRIS spectra and radio occultation-derived profiles of the ratio of temperature to mean molecular were combined to obtain He/H_2. Temperature profiles for various mean molecular weights were used to calculate theoretical spectra, which were compared with the measured IRIS spectra at the occultation point. The molecular weight giving the best fit was then used to infer He/H_2. Subsequent comparisons with Galileo probe

results on Jupiter and a reanalysis of Saturn data in which only IRIS spectra were used indicate possible systematic errors in this technique (see Section 3.1.1). Both approaches will be used to obtain the Saturn He/H_2 ratio from the Cassini data.

Examination of the Saturn nadir kernels in Figure 4 reveals a gap in altitude coverage between ~3 and 100 mbar. The addition of limb viewing helps to fill in this gap. Indeed the highest H_2 limb kernels, at 600 cm^{-1}, overlap the nadir-viewing kernels corresponding to the ν_4 band of CH_4, indicating that the CH_4 abundance of Saturn can unambiguously be determined. The additional air mass provided by limb viewing in the ν_4 band of CH_4 also permits one to obtain temperatures to higher altitudes, to μ bar levels, although the retrieval at these levels is probably more complicated than discussed, because of non-LTE conditions.

Figure 12 depicts the normalized kernels for retrieval of atmospheric temperatures on Titan. Here collision-induced absorption of N_2 below 150 cm^{-1} replaces collision-induced absorption by hydrogen as the dominant opacity source in the far-infrared. Again, limb viewing in the far infrared allows one to retrieve temperatures in the tropopause region and lower stratosphere that would otherwise be inaccessible from nadir viewing alone. The slight overlap between the inversion kernels from N_2 absorption and those from the ν_4 band of CH_4 will allow one to separate the effects of temperature and CH_4, permitting the unambiguous retrieval of the distribution of CH_4 in Titan's stratosphere. The rotational lines of CH_4 near 100 cm^{-1}, whose kernels (not shown) lie at lower altitudes in the stratosphere than those near 1300 cm^{-1}, provide more overlap with the kernel from N_2. Unlike the situation on Saturn, CH_4 on Titan is a condensable, and the stratospheric abundance potentially can vary with latitude. The direct retrieval of its spatial distribution is of great interest.

In addition to CH_4 on both Saturn and Titan and the Saturn hydrogen ortho-para ratio and He/H_2, a number of other atmospheric parameters will be retrieved, including the abundances of hydrocarbons in the stratospheres of both Saturn and Titan. For these retrievals, the necessary independent constraint on the stratospheric thermal structure is provided by the retrievals from the ν_4 band of CH_4 band discussed above. Normalized nadir and limb contribution functions for spectral regions of C_2H_2 and C_2H_6 absorption are shown in Figure 9 for Saturn. Figure 17 depicts the contribution functions for spectral regions of C_2H_2, C_2H_6, and HCN absorption on Titan. Here, the contribution function is defined as the integrand in the first term on the right-hand side of (A3) and serves to indicate the portion of the atmosphere to which the measurement is sensitive. (Technically, the contribution function contains $B(T)$ instead of $dB(T)/dT$.) In the case of the nadir measurements, the stratosphere is not completely opaque in these bands, and significant contributions to the measured radiances originate in the troposphere. Only mean abundances over relatively thick layers can be obtained; however, these retrievals can provide detailed horizontal mapping of these gases. In contrast, the limb-viewing measurements can provide significant vertical information on these gases when sufficiently near Saturn or Titan. The retrieval of the mole fraction profile of a gas from limb measurements is a highly non-linear problem, usually requiring considerable iteration. In addition, to

match the finite FOV of the instrument, contributions along several ray paths must be calculated for each limb foot print and each wavenumber. The problem is made computationally tractable by adopting the correlated-k approach for atmospheric transmittances (Goody and Yung, 1989). While C_2H_2, C_2H_6, and HCN have been used as illustrations here, similar analyses will be applied to other constituents on Saturn and especially Titan. The inversion approach will provide a framework for assessing information content and analyzing error propagation even for gases that yield relatively weak spectral signals.

Appendix B: FP1 FOV Response

CIRS is calibrated by viewing uniformly bright targets (the calibration shutter and/or deep space). This establishes the mean spatial response of the instrument FOV. For an ideal interferometer, the spatial response is uniform, so that the above procedure defines an adequate calibration protocol. However, the CIRS spatial response of FP1 is center-weighted. During the tour, many targets observed using FP1 will either not fill the field (such as satellites at large distances) or will be nonuniformly bright across the field (such as cloud structures on Saturn, or radial structure in the rings). To adequately calibrate such data it is therefore necessary to quantify the departure from the spatially uniform ideal. On 10–11 May 2002, we carefully executed two sets of orthogonal raster scans that covered an area 8 mrad x 8 mrad centered on the FP1 boresight. Jupiter was used as the target source. At the time of this measurement, the subtended angular diameter of Jupiter was 0.290 mrad., or 0.075 of the nominal 3.9 mrad FP1 diameter. This was chosen as a compromise between strong signal and fine spatial resolution. Pointing was verified against support images and against the reconstructed pointing files provided by the Cassini Project. Because the spacecraft was stabilized using reaction wheels, pointing was excellent, with jitter less than 10% of the apparent diameter of Jupiter.

Results of the test are illustrated in Figure 38. The FP1 response is greatest in the center and approximately follows a 2-D gaussian form, truncated in the wings. When viewing a spatially uniform source, a circle of 2.54 mrad diameter contains 50% of the total energy. The outer circle with diameter 4.58 mrad encircles 95% of the total energy (slightly more, actually, because the data have not yet had the finite size of Jupiter deconvolved). The nominal FOV diameter of 3.9 mrad contains 83% of the total.

Next, the signal from a uniform target disk, located at various distances from the FP1 center, was convolved with the spatial response function displayed in Figure 38. The ratio of the detected energy from a uniform target disk of a given radius, to the detected energy for a similar target that fills the FP1 FOV, was then calculated. The results, shown in Figure 39 enable calibration adjustments for imperfect pointing. Along the abscissa, the target is centered in FP1; the radii of contours, such as

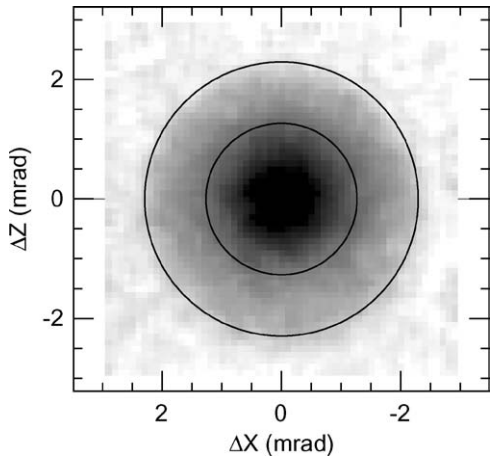

Figure 38. The spatial response of CIRS FP1 as derived from distant observations of Jupiter. The response is center-weighted, and approximately follows a 2-D gaussian form with truncated wings. Viewing a uniform target, the inner circle (radius 1.27 mrad) encloses 50% of the total signal. The outer circle (radius 2.29 mrad) encloses 95% of the total signal.

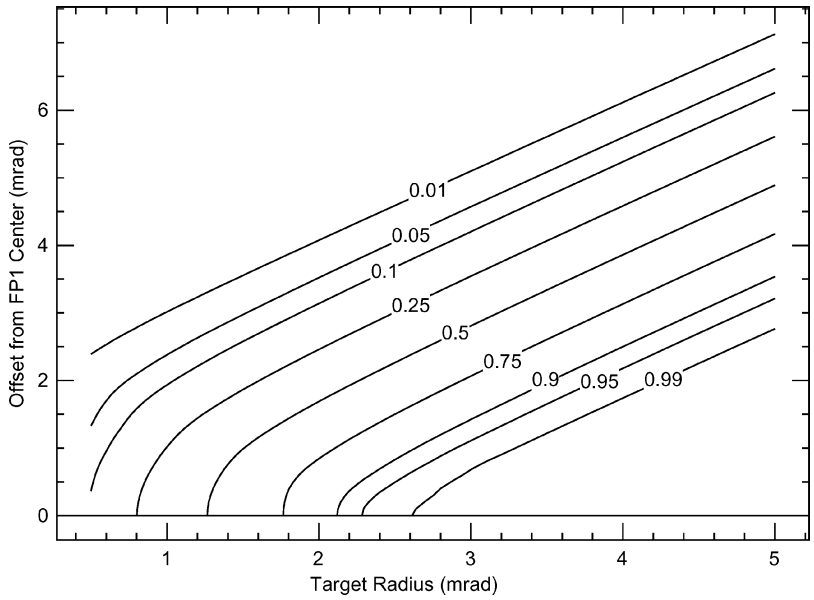

Figure 39. The fraction of a filled FP1 signal contributed by a finite circular target that is arbitrarily located within the FOV. The largest signal from such an unresolved target is obtained by centering it in the FOV where the spatial response is greatest.

shown in Figure 38, can be determined. The largest fractional encircled energy is obtained by placing the target in the center of FP1 where the spatial response is greatest.

Appendix C: Radiometric Calibration Equations

The response of the instrument is one of the basic parameters describing the instrument and is monitored during flight to watch for any changes in instrument performance. The uncalibrated power spectrum (C_T) of a thermal emission instrument is proportional to the difference between the spectral radiance of the instrument (self-emission) and the incoming target radiance:

$$C_T(\nu) = R(\nu)[B_I(\nu) - I_T(\nu)] \tag{C.1}$$

where ν = the frequency in wavenumbers (cm^{-1}), $C_T(\nu)$ = the amplitude of the observed uncalibrated power spectrum when viewing a target at temperature T_T, $R(\nu)$ = the spectral response of the interferometer in digital counts/spectral radiance, $I_T(\nu)$ = the spectral radiance of the target in W cm^{-2} $ster^{-1}/cm^{-1}$ at temperature T_T, and $B_I(\nu)$ = the spectral radiance of the instrument (self-emission) in W cm^{-2} $ster^{-1}/cm^{-1}$.

The instrument self-emission is the dominant source of signal in any observation.

Far-Infrared Interferometer. The far infrared polarizing interferometer uses detectors at the same temperature as the instrument and telescope (170 K). Consequently, we only have one calibration parameter ($R(\nu)$) to determine, and need only one calibration target, which is deep space. We may assume that $B_I(\nu) = B_{170K}(\nu)$. Then, from Equation (C.1) the applicable calibration equations are:

$$C_{\mathrm{T}}(\nu) = R(\nu)[B_{170K}(\nu) - I_{\mathrm{T}}(\nu)] \tag{C.2}$$

$$C_{\mathrm{C}}(\nu) = R(\nu)[B_{170K}(\nu) - B_{\mathrm{C}}(\nu)] \tag{C.3}$$

where $C_{\mathrm{C}}(\nu)$ = the amplitude of the observed uncalibrated power spectrum when viewing a target at temperature = $T_{\mathrm{C}} = 3$ K, $B_{\mathrm{C}}(\nu)$ = the spectral radiance of the cold blackbody calibration target (deep space) at temperature = T_{C}, $B_{170K}(\nu)$ = the Planck function in W cm^{-2} $ster^{-1}/cm^{-1}$ at temperature $T_I = 170$ K.

Equations (C.2) and (C.3) may be solved for $I_{\mathrm{T}}(\nu)$ and $R(\nu)$:

$$I_{\mathrm{T}}(\nu) = B_{170K}(\nu) - \frac{C_{\mathrm{T}}(\nu)}{C_{\mathrm{C}}(\nu)}[B_{170K}(\nu) - B_{\mathrm{C}}(\nu)] \tag{C.4}$$

$$R(\nu) = \frac{C_{\mathrm{C}}(\nu)}{B_{170K}(\nu) - B_{\mathrm{C}}(\nu)} \tag{C.5}$$

Mid-Infrared Interferometer. The mid-infrared interferometer has two sets of detectors cooled to ~80 K, quite different from that of the interferometer at 170 K. Consequently, the instrument emission term is due to a unknown combination of 80 K and 170 K radiation from the different optical components in the optical

train. Thus we need to determine two calibration parameters ($R(\nu)$ and $B_I(\nu)$) and need two calibration targets. For the mid-infrared interferometer, two blackbody reference sources will be viewed to establish the calibration: deep space at $T_C \sim$ 3K, and a warm blackbody (via the shutter) at $T_W = T_I$ =170 K. In addition to Equation (C1) the applicable calibration equations are:

$$C_C(\nu) = R(\nu)[B_I(\nu) - B_C(\nu)] \tag{C.6}$$

$$C_W(\nu) = R(\nu)[B_I(\nu) - B_W(\nu)] \tag{C.7}$$

where $B_C(\nu)$ = the Planck function at temperature $T_C = 3$ K; $B_W(\nu)$ = the Planck function at temperature $T_W = 170$ K.

Assuming that the spectral response is independent of the target radiance, and that the signal processing chain and detectors are linear, the three equations may be solved for $I_T(\nu)$, $R(\nu)$, and $B_I(\nu)$:

$$I_T(\nu) = \frac{(C_T(\nu) - C_C(\nu))B_W(\nu) + (C_W(\nu) - C_T(\nu))B_C(\nu)}{C_W(\nu) - C_C(\nu)} \tag{C.8}$$

$$R(\nu) = \frac{C_C(\nu) - C_W(\nu)}{B_W(\nu) - B_C(\nu)} \tag{C.9}$$

$$B_I(\nu) = \frac{C_C(\nu)B_W(\nu) - B_C(\nu)C_W(\nu)}{C_C(\nu) - C_W(\nu)} \tag{C.10}$$

The above formalism has assumed that the combined optical and electrical phase characteristics of the instrument are the same for all target radiances and for the internal instrument emission. This assumption is correct for FP1, because it is isothermal (Brasunas, 2002), but it only approximately holds for FP3 and FP4. For these, the above formalism will have to include complex Fourier transforms, using the complex power spectra and not just their amplitudes (Revercomb *et al.* 1988). A more detailed discussion of the CIRS calibration procedure will be given elsewhere.

References

Abbas, M. M., LeClair, A., Owen, T., Conrath, B. J., Flasar, F. M., Kunde, V. G., *et al.*: 2004, *Astrophys. J.* **602**, 1063–1074.

Achterberg, R. K., Conrath, B. J., Gierasch, P. J., and Flasar, F. M.: 2003, *Bull. Amer. Astron. Soc.* **35**, 997.

Achterberg, R. K. and Flasar, F. M.: 1996, *Icarus* **119**, 350–369.

Allison, M., Godfrey, D. A., and Beebe, R. F.: 1990, *Science* **247**, 1061–1063.

Andrews, D. G., Holton, J. R., and Leovy, C. B.: 1987, *Middle Atmosphere Dynamics*, Academic Press, Orlando, U.S.A., 489 pp.

Araki, S.: 1991, *Icarus* **90**, 139–171.

Atreya, S. K., Edgington, S. G., Trafton, L. M., Caldwell, J. J., Noll, K. S., and Weaver, H. A.: 1995, *Geophys. Res. Let.* **22**, 1625–1628.

Atreya, S. K., Mahaffy, P. R., Niemann, H. B., Wong, M. H., and Owen, T. C.: 2003, *Planet. Space Sci.* **51**, 105–112.
Atreya, S. K., Wong, M. H., Owen, T. C., Mahaffy, P. R., Niemann, H. B., de Pater, I., *et al.*: 1999, *Planet. Space Sci.* **47**, 1243–1262.
Aumann, H.H. and Kieffer, H. H.: 1973, *Astrophys. J.* **186**, 305–311.
Awal, M. and Lunine, J. I.: 1994, *Geophys. Res. Lett.* **21**, 2491–2494.
Baines, K. H. and Bergstralh, J. T.: 1986, *Icarus* **109**, 20–39.
Baines, K. H., Michelson, M. E., Larson, L. E., and Ferguson, D. W.: 1995, *Icarus* **114**, 328–340.
Bandfield, J.L.: 2002. *J. Geophys. Res. (Planets)* **107** (E6), CiteID 5042.
Barnet, C. D., Westphal, J. A., Beebe, R. F., and Huber, L. F.: 1992, *Icarus* **100**, 499–511.
Beebe, R. F., Barnet, C., Sada, P. V., and Murrell, A. S.: 1992, *Icarus* **95**, 163–172.
Bell, J. F., Cruikshank, D. P., and Gaffey, M. J.: 1985, *Icarus* **61**, 192–207.
de Bergh, C., Schmitt, B., Binzel, R. P., and Bus, S. J.: 2003, *Bull. Amer. Astron. Soc.* **35**, 940.
Bézard, B., Coustenis, A., and McKay, C. P.: 1995, *Icarus* **113**, 267–276.
Bézard, B., Drossart, P., Lellouch, E., Tarrago, G., and Maillard, J. P.: 1989, *Astrophys. J.* **346**, 509–513.
Bézard, B., Feuchtgruber, H., Moses, J. I., and Encrenaz, T.: 1998, *Astron. Astroph.* **334**, L41–L44.
Bézard, B., Gautier, D., and Conrath, B.: 1984, *Icarus* **60**, 274–288.
Bézard, B., Gautier, D., and Marten, A.: 1986, *Astron. Astrophys.* **161**, 387–402.
Bézard, B., Marten, A., and Paubert, G.: 1993, *Bull. Amer. Astron. Soc.* **25**, 1100.
Bézard, B., Moses, J. I., Lacy, J., Greathouse, T., Richter, M., and Griffith, C.: 2001a, *Bull. Amer. Astron. Soc.* **33**, 1079–1080.
Bézard, B., Drossart, P., Encrenaz, T., and Feuchtbruber, H.: 2001b, *Icarus* **155**, 492–500.
Bird, M. K., Dutta-Roy, R., Heyl, M., Allison, M., Asmar, S. W., Folkner, W. M., Preston, R. A., Atkinson, D. H., Edenhoffer, P., Plettemeier, D., Wohlmuth, R., Iess, L., and Tyler, G. L.: 2002, *Space Sci. Rev.* **104**, 613–640.
Bossard, A., Kamga, R., and Raulin, F.: 1986, *Icarus* **67**, 305–324.
Brasunas, J. C.: 2002, *Appl. Optics* **41**, 2481–2487.
Brasunas, J. C. and Lakew, B.: 2004, Long-term stability of the Cassini Fourier transform spectrometer en route to Saturn, in *Recent Res. Devel. Optics.* **4**, 95–113.
Bregman, J. D., Lester, D. F., Rank, D. M.: 1975, *Astrophys. J.* (*Lett.*) **202**, L55–L56.
Briggs, F.H. and Sacket, P. D.: 1989, *Icarus* **80**, 77–103.
Broadfoot, A. L., Sandel, B. R., Shemansky, D. E., Holberg, J. B., Smith, G. R., Strobel, *et al.*: 1981, *Science* **204**, 979–983.
Brown, M. E.: 2000, *Astron. J.* **119**, 977–983.
Brown, M. E., Bouchez, A. H., and Griffith, C. A.: 2002, *Nature* **420**, 797–797.
Brown, R. H.: 1983, *Icarus* **56**, 414–425.
Brown, R. H. and Matson, D. L.: 1987, *Icarus* **72**, 84–94.
Brown, R. H., Baines, K. H., Bellucci, G., Bibring, J.-P., Buratti, B.J., Capaccioni, F., *et al.*: 2004, 'Cassini Visible and Infrared Mapping Spectrometer experiment', *Space Sci. Rev.*, this issue.
Buratti, B. J.: 1985, *Icarus* **61**, 208–217.
Buratti, B. J., Hicks, M. D., Tryka, K. A., Sittig, M. S., Newburn, R. L.: 2002, *Icarus* **155**, 375–381.
Buratti, B. J., Mosher, J. A., and Johnson, T. V.: 1990, *Icarus* **87**, 339–357.
Burns, J. A., Hamilton, D. P., and Showalter, M. R.: 2001. Dusty rings and circumplanetary dust: Observations and simple physics, in: Grün, E., Gustafson, B. A. S., Dermott, S. F., and Fechtig, H. (eds.), *Interplanetary Dust*, Springer-Verlag, Berlin, pp. 641–725.
Cabane, M., Chassefière, E., and Israel, G.: 1992, *Icarus* **96**, 176–189.
Calcutt, S. B., Taylor, F. W., Ade, P., Kunde, V. G., and Jennings, D.: 1992, *J. Brit. Interplanetary Soc*. **45**, 811–816.
Caldwell, J., Hua, X.-M., Turgeon, B., Westphal, J. A., and Barnet, C. D.: 1993, *Science* **260**, 326–329.

Carlson, B. E., Rossow, W. B., and Orton, G. S.: 1988, *J. Atmos. Sci.* **45**, 2066–2081.
Carlson, B. E., Lacis, A. A., and Rossow, W. B.: 1992, *Astrophys. J.* **393**, 357–372.
Cerceau, F., Raulin, F., Courtin, R., and Gautier, D.: 1985, *Icarus* **62**, 207–220.
Charney, J. G. and Drazin, P. G.: 1961, *J. Geophys. Res.* **66**, 83–109.
Christensen, P. R., Bandfield, J. L., Bell, J. F., Gorelick, N., Hamilton, V. E., Ivanov, A., *et al.*: 2003, *Science* **300**, 2056–2061.
Christensen, P. R., Bandfield, J. L., Smith, M. D., Hamilton, V. E., and Clark, R. N.: 2000a, *J. Geophys. Res.* **105**, 9609–9621.
Christensen, P. R., Bandfield, J. L., Clark, R. N., Edgett, K. S., Hamilton, V. E., Hoefen, T., *et al.*: 2000b, *J. Geophys. Res.* **105**, 9623–9642.
Clark, R. N. and McCord, T. B.: 1980, *Icarus* **43**, 161–168.
Clarke, D. W. and Ferris, J. P.: 1997, *Origins of Life and Evol. Biosphere* **27**, 225–248.
Coll, P., Bernard, J.-M., Navarro-González, R., and Raulin, F.: 2003, *Astrophys. J.* **598**, 700–703.
Coll, P., Coscia, D., Gazeau, M.-C., and Raulin, F.: 1997, *Adv. Space Res.* **19** (7), 1113–1119.
Collins, S. A., Cook, A. F. II, Cuzzi, J. N., Danielson, G. E., Hunt, G. E., Johnson, T. V., Morrison, D., Owen, T., Pollack, J. B., Smith, B. A., and Terrile, R. J.: 1980, *Nature* **288**, 439–443.
Colthup, N. B., Daley, L. H., and Wiberley, S. E.: 1975, *Introduction to Infrared and Raman Spectroscopy*, Academic Press, New York, 523 pp.
Comas Sola, J.: 1908, *Astron. Nachr.* **179**, 289–290.
Combes, M., Vapillon, L., Gendron, E., Coustenis, A., Lai, O., Wittenberg, R., and Sirdey, R.: 1997, *Icarus* **129**, 482–497.
Connerney, J. E. C. and Waite, J. H.: 1984, *Nature* **312**, 136–138.
Conrath, B. J., Flasar, F. M., Pirraglia, J. A., Gierasch, P. J., and Hunt, G. E.: 1981, *J. Geophys. Res.* **86**, 8679–8775.
Conrath, B. J. and Gierasch, P. J.: 1983, *Nature* **306**, 571–572.
Conrath, B. J. and Gierasch, P. J.: 1984, *Icarus* **57**, 184–204.
Conrath, B. J. and Pirraglia, J. A.: 1983, *Icarus* **53**, 286–291.
Conrath, B. J. and Gautier, D.: 2000, *Icarus* **144**, 124–134.
Conrath, B. J., Gautier, D., Hanel, R. A., and Hornstein, J. S.: 1984, *Astrophys. J.* **282**, 807–815.
Conrath, B. J., Gierasch, and Ustinov, E. A.: 1998, *Icarus* **135**, 501–517.
Cooke, Maren: 1991. *Saturn's Rings: Photometric Studies of the C Ring and Radial Variation in the Keeler Gap*. PhD Thesis, Cornell University, p. 65.
Courtin, R., Léna, P., De Muizon, M., Rouan, D., Nicollier, C., and Wijnbergen, J.: 1979, *Icarus* **38**, 411–419.
Courtin, R., Gautier, D., Marten, A., and Kunde, V.: 1983, *Icarus* **53**, 121–132.
Courtin, R., Gautier, D., Marten, A., Bézard, B., and Hanel, R.: 1984, *Astrophys. J.* **287**, 899–916.
Courtin, R., Gautier, D., and McKay, C. P.: 1995, *Icarus* **114**, 144–162.
Courtin, R., and Kim, S. J.: 2002, *Planet. Space Sci.* **50**, 309–321.
Coustenis, A. and Bézard, B.: 1995, *Icarus* **115**, 126–140.
Coustenis, A., Bézard, B., and Gautier, D.: 1989a, *Icarus* **113**, 267–276.
Coustenis, A., Bézard, B. and Gautier, D.: 1989b, *Icarus* **82**, 67–80.
Coustenis, A., Bézard, B., Gautier, D., Marten, A., and Samuelson, R.: 1991. *Icarus* **89**, 152–167.
Coustenis, A., Encrenaz, Th., Bézard, B., Bjoraker, G., Graner, G., Dang-Nhu, M., and Arié, E.: 1993, *Icarus* **102**, 240–260.
Coustenis, A., Gendron, E., Lai, O., Veran, J.-P. Woillez, J., Combes, M., *et al.*: 2001, *Icarus* **154**, 501–515.
Coustenis, A., Salama, A., Lellouch, E., Encrenaz, Th., Bjoraker, G. L., Samuelson, R. E., de Graauw, Th., Feuchtgruber, H., and Kessler, M. F.: 1998, *Astron. Astrophys.* **336**, L85–L89.
Coustenis, A., Salama, A., Schulz, B., Ott, S., Lellouch, E., Encrenaz, Th., Gautier, D., and Feuchtgruber, H.: 2003, *Icarus* **161**, 383–403.

Coustenis, A., Schmitt, B., Khanna, R. K., and Trotta, F.: 1999, *Planet. Space Sci.* **47**, 1305–1329.
Craig, I. J. D. and Brown, J. C.: 1986, *Inverse Problems in Astronomy*, Adam Hilger Ltd., Boston.
Cruikshank, D. P.: 1979, *Icarus* **37**, 307–309.
Cruikshank, D. P. and Brown, R. H.: 1982, *Icarus* **50**, 82–87.
Cruikshank, D. P., Brown, R. H., Calvin, W. M., Roush, T. L., and Bartholomew, M. J.: 1998. in Schmitt, B. de Bergh, C., and Festou, M. (eds.), *Solar System Ices*, Kluwer Academic Publishers, Kluwer, Dordrecht, pp. 579–606.
Cruikshank, D. P., Veverka, J., and Lebofsky, L. A.: 1984, Satellites of Saturn: Optical properties, in Gehrels, T., and Matthews, M. S. (eds.), *Saturn*, University of Arizona Press, Tucson, pp. 640–667.
Cunningham, C. T., Ade, P. A. R., Robson, E. I., Nolt, I. G., and Radostitz, J. V.: 1981, *Icarus* **48**, 127–139.
Cuzzi, J. N., Lissauer, J. J., Esposito, L. W., Holberg, J. B., Marouf, E. A., Tyler, G. L., and Boischot, A.: 1984, Saturn's rings: Properties and processes, in Greenberg, R. and Brahic, A. (eds.), *Planetary Rings*, University of Arizona Press, Tucson. pp. 72–198.
Cuzzi, J. N., Colwell, J. E., Esposito, L. W., Porco, C. C., Murray, C. D., Nicholson, P. D., Spilker, L. J., Marouf, E. A., French, R. C., Rappaport, N., and Muhleman, D.: 2002, *Space Sci. Rev.* **118**, 209–251.
Cuzzi, J. N. and Estrada, P. R.: 1998, *Icarus* **132**, 1–35.
Delitsky, M. L. and Lane, A. L.: 1998, *J. Geophys. Res.* **103**, 31,391–31,403.
Delitsky, M. L. and Lane, A. L.: 2002, *J. Geophys. Res.* **107**, 3.1–3.17.
Delitsky, M. L., Lane, A. L., Henry-Riyad, H., and Tidwell, T.T.: 2003, *Bull. Amer. Astron. Soc.* **35**, 914.
Delpech, C., Guillemin, J.-C., Paillous, P., Khlifi, M., Bruston, P., and Raulin, F.: 1994, *Spectrochimica Acta* **50A**, 1095–1100.
Desch, M. D. and Kaiser, M. L.: 1981, *Geophys. Res. Lett.* **8**, 253–256.
De Pater, I. and Dickel, J. R.: 1991, *Icarus* **94**, 474–492.
Dermott, S. F. and Sagan, C.: 1995, *Nature* **374**, 238–240.
Dones, L., Cuzzi, J. N., and Showalter, M.R.: 1993, *Icarus* **105**, 184–215.
Doyle, L. R., Dones, L., and Cuzzi, J. N.: 1989, *Icarus* **80**, 104–135.
Drossart, P.,Lellouch, E., Bézard, B., Maillard, J. P., and Tarrago, G.: 1990, *Icarus* **83**, 248–253.
Dubouloz, N., Raulin, F., Lellouch, E., and Gautier, D.: 1989, *Icarus* **82**, 81–96.
Dunkerton, T.: 1978, *J. Atmos. Sci.* **35**, 2325–2333.
Eliassen, A. and Palm, E.: 1961, *Geophys. Publ.* **22**(3), 1–23
Ellsworth, K. and Schubert, G.: 1983, *Icarus* **54**, 490–510.
Epstein, E. E., Janssen, M. A., and Cuzzi, J. N.: 1984, *Icarus* **58**, 403–411.
Esposito, L. W., Cuzzi, J. N., Holberg, J. H., Marouf, E. A., Tyler, G. L., and Porco, C. C.: 1984, 'Saturn's rings: Structure, dynamics, and particle properties', in Gehrels, T., and Matthews, M. S.(eds.), *Saturn*, University of Arizona Press, Tucson, pp. 463–545.
Esposito, L. W., Barth, C. A., Colwell, J. E., Lawrence, G. M., McClintock, W. E., Stewart, A. I. F., *et al.*: 2004, *Space Sci. Rev.*, this issue.
Estrada, P. R. and Cuzzi, J. N.: 1996, *Icarus* **122**, 251–272.
Ferrari, C., Galdemard, P., Lagage, P. O., Pantin, E., and Quoirin, C.: 2003, Imaging Saturn's rings with CAMIRAS: Thermal inertia of B and C rings. Preprint.
Feuchtgruber, H., Lellouch, E., De Graauw, T., Bézard, B., Encrenaz, Th., and Griffin, M.: 1997, *Nature* **389**, 159–162.
Flasar, F. M.: 1983, *Science* **221**, 55–57.
Flasar, F. M.: 1998a, *Planet. Space Sci.* **46**, 1109–1124.
Flasar, F. M.: 1998b, *Planet. Space Sci.* **46**, 1125–1147.
Flasar, F. M. and Conrath, B. J.: 1990, *Icarus* **85**, 346–354.

Flasar, F. M. and Conrath, B. J.: 1992, 'The meteorology of Titan', in *Proceedings Symposium on Titan*, European Space Agency SP-**338**, pp. 89–99.
Flasar, F. M., Conrath, B. J., Pirraglia, J. A., Clark, P. C., French, R. G., and Gierasch, P. J.: 1981b, *J. Geophys. Res.* **86**, 8759–8767.
Flasar, F. M., Kunde, V. G., Achterberg, R. K., Conrath, B. J., Simon-Miller, A. A., Nixon, C. A., *et al.*: 2004, *Nature* **427**, 132–135.
Flasar, F. M. Samuelson, R. E., and Conrath, B. J.: 1981a, *Nature* **292**, 693–698.
Fortney, J. I. and Hubbard, W. B.: 2003, *Icarus* **164**, 228–243.
Fouchet, T., Lellouch, E., and Feuchtgruber, H.: 2003, *Icarus* **161**, 127–143.
Fouchet, T., Orton, G. S., Irwin, P. G. J., and Calcutt, S. B.: 2004a, *Icarus* **170**, 237–241.
Fouchet, T., Irwin, P. G. J., Parrish, P., Calcutt, S. B., Taylor, F. W., Nixon, C., and Owen, T.: in press 2003b, *Icarus.* **172**, 50–58.
Fouchet, T., Prangé, R., Connerney, J.E.C., Courtin, R., Ben Jaffel, L., Noll, K., and McConnell, J. C.: 1996, *Bull. Amer. Astron. Soc.* **28**, 1129.
Friedson, A. J., West, R. A., Hronek, A. K., Larsen, N. A., and Dalal, N.: 1999, *Icarus* **138**, 141–156.
Froidevaux, L.: 1981, *Icarus* **46**, 4–17.
Froidevaux, L. and Ingersoll, A. P.: 1980, *J. Geophys. Res.* **85**, 5929–5936.
Froidevaux, L., Matthews, K., and Neugebauer, G.: 1981, *Icarus* **46**, 18–26.
Gautier, D., Conrath, B., Flasar, M., Hanel, R., Kunde, V., Chedin, A., and Scott, N.: 1981., *J. Geophys. Res.* **86**, 8713–8720.
Gautier, D. and Grossman, K.: 1972, *J. Atmos. Sci.* **29**, 788–792.
Gautier, D. and Owen, T.: 1983, *Nature* **304**, 691–694.
Gautier, D. and Owen, T.: 1989, The composition of the outer planets' atmospheres, in Atreya, S. K., Pollack, J. B., and Matthews, M. S. (eds.) *Origins and Evolution of Planetary and Satellite Atmospheres*, to The University of Arizona Press, Tucson, pp. 487–512.
Gendron, E., Coustenis, A., Drossart, P., Combes, M., Hirtzig, M., Lacombe, F., Rouan, D., Collin, C., Pau, S., Lagrange, A.-M.: in press, *Astron. Astroph.* **417**, L21–L24.
Gierasch, P. J. and Conrath, B. J.: 1987, *J. Geophys. Res.* **92**, 15019–15029.
Gierasch, P. J., Conrath, B. J., and Magalhães, J. A.: 1986, *Icarus* **67**, 456–483.
Gierasch, P. J., Conrath, B. J., and Read, P. L.: 2004, *J. Atmos. Sci.* **61**, 1953–1965.
Gierasch, P. J. and Goody, R. M.: 1969, *J. Atmos. Sci.* **26**, 979–980.
Gille, J. C. and House, F. B.: 1971, *J. Atmos. Sci.* **28**, 1427–1442.
Gillett, F. C., Forrest, W. J., and Merrill, K. M.: 1973, *Astrophys. J.* **184**, L93–L95.
Gillett, F. C.: 1975, *Astrophys. J.* **201**, L41–L43.
Gladman, B., Kavelaars, J. J., Holman, M., Nicholson, P. D., Burns, J. A., Hergenrother, C. W., *et al.*: 2001, *Nature* **412**, 163–166
Godfrey, D. A.: 1990, *Science* **247**, 1206–1208.
Godfrey, D. A.: 1988, *Icarus* **76**, 335–356.
Goody, R. M. and Yung, Y. L.: 1989, *Atmospheric Radiation: Theoretical Basis*, 2nd ed., Clarendon Press, Oxford.
de Graauw, T., Feuchtgruber, H., Bézard, B., Drossart, P., Encrenaz, T., Beintema, D. A., *et al.*: 1997, *Astron. Astrophys.* **321**, L13–16.
Greathouse, T., Moses, J., Bézard, B., Griffith, C., Lacy, J., Knez, C., and Richter, M.: 2003, *Bull. Amer. Astron. Soc.* **35**, 1019.
Griffin, M. J., Naylor, D. A., Davis, G. R., Ade, P. A. R., Oldman, P. G., Swinyard, B. M., *et al.*: 1996, *Astron. Astrophys.* **315**, L389–L392.
Griffith, C. A., Owen, T., Geballe, T. R., Rayner, J., Rannou, P.: 2003, *Science* **300**, 628–630.
Griffith, C. A., Owen, T., Miller, G. A., and Geballe, T.: 1998, *Nature* **395**, 575–578.
Griffith, C. A., Hall, J. L., and Geballe, T. R.: 2000, *Science* **290**, 509–513.
Grossman, A. W., Muhleman, D. O., and Berge, G. L.: 1989, *Science* **245**, 1211–1215.

Grundy, W. M., Buie, M. W., Stansberry, J. A., and Spencer, J. R.: 1999, *Icarus* **142**, 536–549.
Guillot, T.: 1999, *Planet. Space Sci.* **47**, 1183–1200.
Gurwell, M. A. and Muhleman, D. O.: 1995. *Icarus* **117**, 375–382.
Haas, M. R., Erickson, E. F., McKibbin, D. D., Goorvitch, D., and Caroff, L. M.: 1982, *Icarus* **51**, 476–490.
Haff, P. K., Siscoe, G. L., and Eviatar, A.: 1983, *Icarus* **56**, 426–438.
Hamilton, D. P. and Burns, J. A.: 1994, *Science* **264**, 550–553.
Hanel, R., Conrath, B., Flasar, M.,. Kunde, V., Lowman, P., Maguire, W., Pearl, J., Pirraglia, J., and Samuelson, R.: 1979, *Science* **204**, 972–976.
Hanel, R., Crosby, D., Herath, L., Vanous, D., Collins, D., Creswick, H., Harris, C., and Rhodes, M.: 1980, *Applied Optics* **19**, 1391–1400.
Hanel, R., Conrath, B., Flasar, F. M., Kunde, V., Maguire, W., Pearl, J. C., *et al.*: 1981, *Science* **212**, 192–200.
Hanel, R. A., Conrath, B. J., Flasar, F. M., Kunde, V. G., Maguire, W., Pearl, J. C., *et al.*: 1982, *Science* **215**, 544–548.
Hanel, R. A., Conrath, B. J., Jennings, D. E., and Samuelson, R. E.: 2003, *Exploration of the Solar System by Infrared Remote Sensing*, 2nd ed., Cambridge University Press.
Hanel, R. A., Conrath, B. J., Kunde, V. G., Pearl, J. C., and Pirraglia, J. A.: 1983, *Icarus* **53**, 262–285.
Hanel, R. A., Schlachman, B., Clark, F. D., Prokesh, C. H., Taylor, J. B., Wilson, W. M., and Chaney, L.: 1970, *Appl. Optics* **9**, 1767–1774.
Hapke, B.: 1996a, *J. Geophys. Res.* **101**, 16,833–16,840.
Hapke, B.: 1996b, *J. Geophys. Res.* **101**,16,817–16,832.
Held, I. M. and Hou, A. Y.: 1980, *J. Atmos. Sci.* **37**, 515–533.
Hidayat, T., Marten, A., Bézard, B., Gautier, D., Owen, T., Matthews, H. E., and Paubert, G.: 1997, *Icarus* **126**, 170–182.
Hidayat, T., Marten, A., Bézard, B., and Gautier, D.: 1998, *Icarus* **133**, 109–133.
Hinson, D. P. and Tyler, G. L.: 1983, *Icarus* **54**, 337–352.
Hoefen, T. M., Clark, R. N., Bandfield, J. L., Smith, J. C., and Christensen, P. R.: in press., *Science.*
Holton, J. R.: 1979, *An Introduction to Dynamic Meteorology*, 2nd ed., Academic Press, New York.
Horanyi, M., Burns, J. A., and Hamilton, D. P.: 1992, *Icarus* **97**, 248–259.
Hoskins, B. J., McIntyre, M. E., and Robertson, A. W.: 1985, *Quart. J. Royal Met. Soc.* **111**, 877–404.
Hourdin, F., Talagrand, O., Sadourny, R., Courtin, R., Gautier, D., and McKay, C. P.: 1995, *Icarus* **117**, 358–374.
Hubbard, W. B.: 1980, *Rev. Geophys. Space Phys.* **18**, 1–9.
Hubbard, W. B., Sicardy, B., Miles, R., Hollis, A. J., Forrest, R. W., Nicolson, I. K. M., *et al.*: 1993, *Astron. Astrophys.* **269**, 541–563.
Hubbard, W. B., Hunten, D. M., Reitsema, D. M., Brosch, N., Nevo, Y., Carreira, E., *et al.*: 1990, *Nature* **343**, 353–355.
Hudgins, D. M., Sandford, S. A., Allamandola, L. J., and Tielens, A. G.: 1993, *Astrophys J. Suppl.* **86**, 713–870.
Hudson, B. L. and Moore, M. H.: 1993, *Astrophys. J.* **404**, L29–L32.
Hunten, D. M., Tomasko, M. G., Flasar, F. M., Samuelson, R. E., Strobel, D. F., and Stevenson, D. J.: 1984, Titan, in Gehrels, T., and Matthews, M. (eds.), *Saturn*, University of Arizona Press, pp. 671–759.
Ingersoll, A. P., Beebe, R. F., Conrath, B. J., and Hunt, G. E.: 1984, 'Structure and dynamics of Saturn's atmosphere', in Gehrels, T., and Matthews, M. (eds.), *Saturn*, University of Arizona Press, pp. 195–238
Ingersoll, A., Orton, G. S., Münch, G., Neugebauer, G., and Chase, S. C.: 1980, *Science* **207**, 439–443.
Ingersoll, A. P. and Porco, C. C.: 1978, *Icarus* **35**, 27–43.

Irwin, P. G. J., Parrish, P., Fouchet, T., Calcutt, S. B., Taylor, F. W., Simon-Miller, A. A., *et al.*: 2004, *Icarus.* **172**, 37–49.
Kargel, J. S., Pozio, S.: 1996, *Icarus* **119**, 385–404.
Karkoschka, E. and Tomasko, M.G.: 1992, *Icarus* **97**, 161–181.
Kaye, J. A. and Strobel, D. F.: 1984. *Icarus* **59**, 314–335.
Kawata, Y.: 1983, *Icarus* **56**, 453–464.
Kawata, Y. and Irvine, W.M.: 1975, *Icarus* **24**, 472–482.
Khanna, R. K., Perera-Jarmer, M. A., and Ospina, M. J.: 1987, *Spectrochim. Acta* **43A**, 421–425.
Khare, B. N., Sagan, C., Thompson, W. R., Arakawa, E. T., Meissen, C., and Tuminello, P. S.: 1994, *Canad. J. Chem.* **72**, 678–694.
Khlifi, M., Nollet, M., Paillous, P., Bruston, P., Raulin, F., Benilan, Y., *et al*.: 1999, *J. Mol. Spectrosc*. **194**, 206–210.
Khlifi, M., Paillous, P., Bruston, P., Raulin, F., and Guillemin, J.-C.: 1996, *Icarus* **124**, 318–328.
Khlifi, M., Paillous, P., Bruston, P., Guillemin, J.-C., Bénilan, Y., Daoudi, A., *et al.*: 1997, *Spectrochimica Acta* **53A**, 707–712.
Khlifi, M. and Raulin, F.: 1991, *Spectrochim. Acta* **47A**, 171–176.
Khlifi, M., Raulin, F., and Dang-Nhu, M.: 1992, *v. Mol. Spectrosc.* **154**, 235–239.
Kliore, A. J., Anderson, J. D., Armstrong, J. W., Asmar, S. W., Hamilton, C. L., Rappaport, N. J., *et al.*: 2003, 'Cassini radio science', *Space Sci. Rev.*, this issue.
Kliore, A., Patel, I. R., Lindal, G. F., Sweetnam, D. N., Hotz, H. B., Waite, J. H., and McDonough, T. R.: 1980, *J. Geophys. Res.* **85**, 5857–5870.
Kuiper, G.: 1944, *Astrophys. J.* **100**, 378–383.
Kunde, V. G., Aikin, A. C., Hanel, R. A., Jennings, D. E., Maguire, W. C., and Samuelson, R. E.: 1981. *Nature* **292**, 686–688.
Kunde, V. G., Ade, P., Barney, R., Bergman, D., Borelli, R., Boyd, D., *et al*.: 1996, *SPIE* **2803**, 162–177.
Kunde, V. G., Flasar, F. M., Jennings, D. E., Bézard, B., Strobel, D. F., Conrath, B.J., *et al.*: 2004, 'Jupiter's atmosheric composition from thermal-infrared observations at high spectral and spatial resolution', *in preparation*.
Lammer, H. and Bauer, S. J.: 2003, *Space Sci. Rev.* **186**, 281–291.
Lammer, H., Stumptner, W., Molina-Cuberos, G. J., Bauer, S. J., and Owen, T.: 2000, *Planet. Space Sci.* **48**, 529–543.
Lane, A. L., Hord, C. W., West, R. A., Esposito, L. W., Coffeen, D. L., Sato, M., *et al.*: 1982, *Science* **215**, 537–543.
Lara, L., Lellouch, E., Lopez-Moreno, J. J., and Rodrigo, R.: 1996, *J. Geophys. Res.* **101**, 23261–23283.
Lara, L. M., Bézard, B., Griffith, C. A., Lacy, J. H., and Owen, T.: 1998, *Icarus* **131**, 317–333.
Lecluse, C., Robert, F., Gautier, D., and Guiraud, M.: 1996, *Planet. Space Sci.* **44**, 1579–1592.
Lellouch, E., Bézard, B., Fouchet, T., Feuchtgruber, H., Encrenaz, T., and de Graauw, T.: 2001, *Astron. Astrophys.* **370**, 610–622.
Lellouch, E., Bézard, B., Moses, J. I., Davis, G. R., Drossart, P., Feuchtgruber, H., *et al.*: 2002, *Icarus* **159**, 112–131.
Lellouch, E., Coustenis, A., Gautier, D., Raulin, F., Dubouloz, N., and Frère, C.: 1989, *Icarus* **79**, 328–349.
Lellouch, E., Coustenis, A., Sebag, B., Cuby, J.-G., López-Valverde, M., Schmitt, B., *et al.*: 2003, *Icarus* **162**, 125–142.
Lemmon, M., Karkoschka, E., and Tomasko, M.: 1993, *Icarus* **103**, 329–332.
Lemmon, M. T., Smith, P. H., Lorenz, R. D.: 2002, *Icarus* **160**, 365–375.
Leovy, C. B., Friedson, A. J., and Orton, G. S.: 1991, *Nature* **354**, 380–382.

Lewis, J. S.: 1972, *Icarus* **16**, 241–252.
Leyrat, C., Ferrari, C., Spilker, L., and Charnoz, S.: 2003, *Bull. Amer. Astron. Soc.* **35**, 951.
Lindal, G. F., Wood, G. E., Hotz, H. B., Sweetnam, D. N., Eshleman, V., and Tyler, G. L.: 1983, *Icarus* **53**, 348–363.
Lindal, G. F., Sweetnam, D. N., and Eshleman, V. R.: 1984, *Astron. J.* **90**, 1136–1146.
Linsky, J. L.: 1998, *Space Sci. Rev.* **84**, 285–296.
Lorenz, E. N.: 1967, *The Nature and Theory of the General Circulation of the Atmosphere*, World Meteorological Organization, 161 pp.
Lorenz, R. D., McKay, C. P., and Lunine, J. I.: 1997, *Science* **275**, 642–644.
Low, F. J. and Rieke, G. H.: 1974, *Astrophys. J.* **190**, L143–L145.
Lunine, J. I.: 1993, *Rev. Geophys*. **31**, 133–149.
Lunine, J. I., Stevenson, D. J., and Yung, Y. L.: 1983, *Science* **222**, 1229–1230.
Lunine, J. I., Yung, Y. L., and Lorenz, R. D.: 1999, *Planet. Space Sci.* **47**, 1291–1303.
Lutz, B. L., De Bergh, C., and Owen, T.: 1983, *Science* **220**, 1374–1375.
Lynch, D. K., Mazuk, A. L., Russell, R. W., and Hackwell, J. A.: 2000, *Icarus* **146**, 43–47.
Magni, G. and Coradini, A.: 2004, *Planet. Space Sci.* **52**, 343–360.
Maguire, W. C., Hanel, R. A., Jennings, D. E., Kunde, V. G., and Samuelson, R. E.: 1981, *Nature* **292**, 683–686.
Mahaffy, P. R., Donahue, T. M., Atreya, S. K., Owen, T. C., and Niemann, H. B.: 1998, *Space Science Rev.* **84**, 251–263.
Marouf, E. A., Tyler, G. L., Zebker, H. A., Simpson, R. A., and Eschelman, V. R., 1983, *Icarus* **54**, 189–211.
Marten, A., Gautier, D., Tanguy, L., Lecacheux, A., Rosolen, C., and Paubert, G.: 1988, *Icarus* **76**, 558–562.
Marten, A., Hidayat, T., Biraud, Y., and Moreno, R.: 2002, *Icarus* **158**, 532–540.
Marten, A., Hidayat, T. Moreno, R., Paubert, G., Bézard, B., Gautier, D. Matthews, H., and Owen, T.: 1997, *IAU Circular* **6702**, July 19.
Martin, D. H.: 1982, Polarizing (Martin-Puplett) interferometric spectrometers for the near- and submillimeter spectra, in Button, K.J. (ed.), *Infrared and Millimeter Waves, Vol. 6, Systems and Components*, Ch. 2, Academic Press, New York.
Martin, D. H. and Puplett, E.: 1969, *Infrared Phys.* **10**, 105–109.
Massie, S. T. and Hunten, D. M.: 1982, *Icarus* **49**, 213–226.
Matson, D. L. and Brown, R.H.,: 1989, *Icarus* **77**, 67–81.
Matson, D. L. and Nash, D.: 1983, *J. Geophys. Res.* **88**, 4,771–4,783.
Matson, D. L., Spilker, L. J., and Lebreton, J.-P.: 2002, *Space Sci. Rev.* **104**, 1–58.
Matzler, C.: 1998, 'Microwave properties of ice and snow', in Schmitt, B., De Bergh, C., and Festou, M. (eds.), *Solar System Ices*, Kluwer, Dordrecht, pp. 241–257
McCord, T., Carlson, R. W., Smythe, W. D., Hansen, G. B., Clark, R. N., Hibbitts, C. A., *et al.*: 1997, *Science* **278**, 271–275.
McKay, C. P., Coustenis, A., Samuelson, R. E., Lemmon, M. T., Lorenz, R. D., Cabane, M., Rannou, P., and Drossart, P.: 2001, *Planet. Space Sci.* **49**, 79–99.
Meier, R., Smith, B.-A., Owen, T.-C., Terrile, R.-J.: 2000, *Icarus* **145**, 462–473.
Meier, R. Owen, T., Matthews, H., and Marten, A.: 1997, JCMT observations of the HCN 4–3 transition, unpublished.
Mellon, M. T., Jakosky, B. M., Kieffer, H. H., and Christensen: 2000, *Icarus* **148**, 437–455.
Mennella, V., Brucato, J. R., Colangeli, L., Palumbo, P., Rotundi, A., and Bussolletti, E.: 1998, *Astroph. J.* **496**, 1058–1066.
Morrison, D.: 1974, *Icarus* **22**, 51–56.
Morrison, D., Jones, T. J., Cruikshank, D. P., and Murphy, R. E.: 1975, *Icarus* **24**, 157–171.

Moses, J. I., Bézard, B., Lellouch, E., Gladstone, G. R., Feuchtgruber, H., and Allen, M.: 2000a, *Icarus* **143**, 244–298.
Moses, J. I., Lellouch, E., Bézard, B., Gladstone, G. R., Feuchtgruber, H., and Allen, M.: 2000b, *Icarus* **145**, 166–202.
Mousis, O., Gautier, D., and Coustenis, A.: 2002, *Icarus* **159**, 156–165.
Muhleman, D.O., Grossman, A. W., Butler, B. J., and Slade, M. A.: 1990, *Science* **248**, 975–980.
Murphy, R. E., Cruikshank, D. P., and Morrison, D.: 1972, *Astrophys. J.* **177**, L93–L96.
Nicholson, P. D., Hamilton, D. P., Matthews, K., and Yoder, C.F.: 1992, *Icarus* **100**, 464–484.
Niemann, H. B., Atreya, S. K., Carignan, G. R., Donahue, Haberman, T. M., Harpold, D. N., *et al.*: 1996, *Science* **272**, 846–849.
Niemann, H. B., Atreya, S. K., Carignan, G. R., Donahue, T. M., Haberman, J. A., Harpold, D. N., *et al.*: 1998, *J. Geophys. Res.* **103**, 22831–22845.
Nishio, M., Paillous, P., Khlifi, M., Bruston, P., and Raulin, F.: 1995, *Spectrochim. Acta* **51A**, 617–622.
Nixon, C. A., Achterberg, R. K., Conrath, B. J., Irwin, P. G. J., Fouchet, T., Parrish, P. D., *et al.*, : 2004, 'Meridional variations of C_2H_2 and C_2H_6 in Jupiter's atmosphere from Cassini CIRS infrared spectra', preprint.
Noll, K., Knacke, R. F., Geballe, T. R., Tokunaga, A. T.: 1986, *Astrophys. J.* (*Lett.*) **309**, L91–L94.
Noll, K. S. and Larson, H. P.: 1990, *Icarus* **89**, 168–189.
Noll, K. S., Roush, T. L., Cruikshank, D. P., Pendleton, Y. J., and Johnson, R. E.: 1997, *Nature* **388**, 45–47.
Orsolini, Y. and Leovy, C. B.: 1989, *Geophys. Res. Lett.* **16**, 1245–1248.
Orsolini, Y. and Leovy, C. B.: 1993a, *Icarus* **106**, 392–405.
Orsolini, Y. and Leovy, C. B.: 1993b, *Icarus* **106**, 406–418.
Orton, G. S.: 1992, 'Ground-based observations of Titan's thermal spectrum', in *Proceedings Symposium on Titan*, European Space Agency SP-**338**, pp. 81–85.
Orton, G. S. and Ingersoll, A. P. : 1980, *J. Geophys. Res.* **85**, 5871–5881.
Orton, G., Fisher, B., Yanamandra-Fisher, P., Baines, K., Ressler, M., Beach-Kimball, B., *et al.*: 2003, *Bull. Amer. Astron. Soc.* **35**, 1018.
Orton, G., Fisher, B., Yanamandra-Fisher, P., Baines, K. H., Momary, T. W., and Fox, O. D.: 2002, *Bull. Amer. Astron. Soc.* **34**, 855–856.
Orton, G. S., Friedson, A. J., Caldwell, J., Hammel, H. B., Baines, K. H., Bergstralh, J. T., *et al.*: 1991, *Science* **252**, 537–542.
Orton, G. S., Friedson, A. J., Huie, M., Malcom, M., Anthony, D., Caldwell, J., Tokunaga, A., and Klavetter, J.: 1989, *Bull. Amer. Astron. Soc.* **21**, 953–954.
Orton, G.S., Serabyn, E., and Lee, Y.T.: 2001, *Icarus* **149**, 489–490.
Owen, T.: 1982. *Planet. Space Sci*. **30**, 833.
Owen, T., Biver, N., Marten, A., Matthews, H. E., and Meier, R.: 1999a, *IAU Circ.* 7306, Nov. 11.Please check a.
Owen, T. C., Cruikshank, D. P., Dalle Ore, C. M., Geballe, T. R., Roush, T. L., and de Bergh, C.: 1999b, *Icarus* **139**, 379–382.Please check b.
Owen, T. C., Cruikshank, D. P., Dalle Ore, C. M., Geballe, T. R., Roush, T. L., de Bergh, C., *et al.*: 2001. *Icarus* **149**, 160–172.
Pang, K. D., Voge, C. C., Rhoads, J. W., Ajello, J. M.: 1984, *J. Geophys. Res.* **89**, 9,459–9,470.
Pappalardo, R., Collins, G., Helfenstein, P., McCord, T., Prockter, L., Schenk, P., and Spencer, J.: 2004, Ganymede, in Bagenal, F., (eds.), *Jupiter*, Cambridge University Press, pp. 363–396.
Pearl, J., Hanel, R., Kunde, V., Maguire, W., Fox, K., Gupta, S., Ponnamperuma, C., and Raulin, F.: 1979 *Nature* **280**, 757–758.
Pilcher, C. B., Chapman, C., Lebofsky, L. A., and Kieffer, A. A.: 1970, *Science* **167**, 1372–1373.
Pirraglia, J. A.: 1989, *Icarus* **79**, 196–207.

Plescia, J. B.: 1983. *Icarus* **56**, 255–277.
Pollack, J. B., Hubickyi, O. Bodenheimer, P., Lissauer, J. J., Podolak, M., and Greenzweig, Y.: 1966, *Icarus* **124**, 62–85.
Pollack, J. B., Summers, A., and Baldwin, B.: 1973, *Icarus* **20**, 263–278.
Poulet, F. and. Cuzzi, J. N.: 2002, *Icarus* **160**, 350–358.
Poulet, F., Cuzzi, J. N., French, R. G., and Dones, L.: 2002, *Icarus* **158**, 224–248.
Porco, C. C., West, R. A., Squyres, S., McEwen, A., Thomas, P., Murray, C. D., *et al.*: 2004, *Space Sci. Rev.*, this issue.
Prangé, R., Fouchet, T., Connerney, J. E. P., and Courtin, R.: 1999, 'FUV diagnostic of Saturn's stratosphere with the HST: Search for water influx from the rings, in *Planetary Systems: The Long View*, Proc. IXème Conférence de Blois, J. Tran Than Van et L. Celnikier (ed.), Editions Frontières, Paris, pp. 309–312
Prinn, R. G., Larson, H. P., Caldwell, J. J., and Gautier, D.: 1984, Composition and Chemistry of Saturn's Atmosphere, in Gehrels, T., and Matthews, M. S. (eds.), *Saturn*, University of Arizona Press, Tucson, pp. 88–149.
Puetter, R. C. and Russell, R. W.: 1977, *Icarus* **32**, 37–40.
Rannou, P., Hourdin, F., and McKay, C. P.: 2002, *Nature* **418**, 853–856.
Raulin, F.: 1987, *Adv. Space Res.* **7**, 71–81.
Raulin, F., Accaoui, B., Razaghi, A., Dang-Nhu, M., Coustenis, A., and Gautier, D.: 1990, *Spectrochim. Acta* 46A, 671–683.
Raulin, F. and Owen, T. C.: 2003, *Space Sci. Rev.* **104**, 377–394.
Revercomb, H. E., Buijs, H., Howell, H. B., LaPorte, D. D., Smith, W. L., and Sromovsky, L. A.: 1988, *Applied Optics* **27**, 3210–3218.
Richardson, D.: 1994, *Mon. Not. R. Astron. Soc.* **269**, 493–511.
Rodgers, C. D.: 2000, *Inverse Methods for Atmospheric Sounding: Theory and Practive*, London, World Scientific Publishing.
Roe, H. G., de Pater, I., Macintosh, B. A., McKay, C. P.: 2002, *Icarus* **157**, 254–258.
Roellig, T. L., Werner, M. W., Becklin, E. E.: 1988, *Icarus* **73**, 574–583.
Romani, P. N.: 1989, *B.A.A.S.* **21**, 953.
Rosen, P. A.: 1989, Waves in Saturn's rings probed by radio occultation. Scientific Report No D845-1989-1, Jet Propulsion Laboratory.
Saari, J. M. and Shorthill, R. W.: 1963, *Icarus* **2**, 115–136.
Salo, H.: 1995, *Icarus* **117**, 287–312.
Samuelson, R. E. and Mayo, L. A.: 1991, *Icarus* **91**, 207–219.
Samuelson, R. E. and Mayo, L. A.: 1997, *Planet. Space Sci.* **45**, 949–958.
Samuelson, R. E., Hanel, R. A., Kunde, V. G., and Maguire, W. C.: 1981, *Nature* **292**, 688–693.
Samuelson, R. E., Maguire, W. C., Hanel, R. A., Kunde, V. G., Jennings, D. E., Yung, Y. L., and Aikin, A. C.: 1983, *J. Geophys. Res.* **88**, 8709–8715.
Samuelson, R. E., Mayo, L. A., Knuckles, M. A., and Khanna, R. J.: 1997a, *Planet. Space Sci.* **45**, 941–948.
Samuelson, R. E., Nath, N. R., and Borysow, A.: 1997b, *Planet. Space Sci.* **45**, 959–980.
Sánchez-Lavega, A., Lecacheux, J., Colas, F., and Laques, P.: 1993, *Science* **260**, 329–332.
Sánchez-Lavega, A., Pérez-Hoyos, S., Acarreta, J. R., and French, R. G.: 2002, *Icarus* **160**, 216–219.
Sánchez-Lavega, A., Pérez-Hoyos, S., Rojas, J. F., Hues, R., and French, R. G.: 2003, *Nature* **423**, 623–625.
Sandel, B.R., Shemansky, D. E., Broadfoot, A. L., Holberg, J. B., Smith, G. R., McConnell, J. C., *et al.*: 1982, *Science* **215**, 548–553.
Schoeberl, M. R. and Hartmann, D. L.: 1991, *Science* **251**, 46–52.

Schubert, G., Spohn, T., and Reynolds, R. T.: 1986, 'Thermal histories, compositions and internal structures of the moons of the solar system', in Burns, J. A. and Matthews, M. S. (eds.), *Satellites*, University of Arizona Press, Tucson, pp. 224–292.

Sears, W. D.: 1995, *Icarus* **113**, 39–56.

Shindo, F.: 2002, *Spectroscopie IR et UV expérimentale de composés intéressant l'atmosphère de Titan*, Thèse de Doctorat de l'Université Paris 7, Spécialité Astrophysique et Techniques Spatiales.

Shindo, F., Bénilan, Y., Guillemin, J.-C., Chaquin, P., Jolly, A., and Raulin, F.: 2001a, *BAAS*. **33**(3), 1109.

Shindo, F., Bénilan, Y., Chaquin, P., Guillemin, J.-C., Jolly, A., and Raulin, F.: 2001b, *J. Mol. Spectrosc.* **210**(2), 191–195.

Shindo, F., Bénilan, Y., Guillemin, J.-C., Chaquin, P., Jolly, A., and Raulin, F.: 2003, *Planet. Space Sci.* **51**, 9–17.

Showman, A. P.: 2001, *Icarus* **152**, 140–150.

Showalter, M. R.: 1996, *Icarus* **124**, 677–689.

Showalter, M. R. and Cuzzi, J. N.: 1993, *Icarus* **103**, 124–143.

Showalter, M. R., Cuzzi, J. N., and Larson, S. M.: 1991, *Icarus* **94**, 451–473.

Showalter, M. R., Pollack, J. B., Ockert, M. E., Doyle, L., and Dalton, J. B.: 1992, *Icarus* **100**, 394–411.

Shu, F. H., Cuzzi, J. N., and Lissauer, J. J.: 1982, *Icarus* **53**, 185–206.

Sicardy, B., Brahic, A., Ferrari, C., Gautier, D., Lecacheux, J., Lellouch, E., *et al.*: 1990, *Nature* **343**, 350–353.

Simonelli, D. P., Kay, J., Adinolfi, D., Veverka, J., Thomas, P. C., and Helfenstein, P.: 1999, *Icarus* **138**, 249–258.

Smith, B. A., Soderblom, L., Beebe, R., Boyce, J., Briggs, G., Bunker, A., *et al.*: 1981, *Science* **212**, 163–191.

Smith, B. A., Soderblom, L., Batson, R., Bridges, P., Inge, J., Masursky, H., *et al.*: 1982, *Science* **215**, 504–537.

Smith, M. D., Conrath, B. J., and Gautier, D.: 1996a, *Icarus* **124**, 598–607.Please check a.

Smith, M. D. and Gierasch, P. J.: 1995, *Icarus* **116**, 159–179.

Smith, P. H., Lemmon, M. T., Lorenz, R. D., Sromovsky, L. A., Caldwell, J. J., and Allison, M. D.: 1996b, *Icarus* **119**, 336–349.Please check b.

Smith, R.G., Robinson, G., Hyland, A. R., and Carpenter, G. L.: 1994, *Month. Not. Roy. Astron. Soc.* **271**, 481–489.

Smith, W. H. and Baines, K. H.: 1990, *Icarus* **85**, 109–119,

Snyder-Hale, A. and Hapke, B.: 2002, *Icarus* **156**, 318–334.

Socrates, G.: 1980. *Infrared Characteristic Group Frequencies*, Wiley-Interscience, New York.

Spencer, J.R.: 1987, 'The surfaces of Europa, Ganymede, and Callisto: An investigation using Voyager IRIS thermal infrared spectra. Ph.D. Thesis, University of Arizona, Tucson.

Spencer, J.: 1990, *Icarus* **83**, 27–38.

Spencer, J. R., Carlson, R. W., Becker, T. L., and Blue, J. S.: 2004, Maps and spectra of Jupiter and the Galilean satellites, In *Jupiter: Planet, Satellites, and magnetosphere*, Bagenal, F., Mckinnon, W. B., and Dowling, T. (eds.), Cambridge University Press, pp. 689–698.

Spencer, J. R., Tamppari, L. K., Martin, T. Z., and Travis, L. D.: 1999, *Science* **284**, 1514–1516.

Spilker, L., Pilorz, S., Ferrari, C., Pearl, J., and Wallis, B.: 2003, *Bull. Amer. Aston. Soc.* **35**, 929.

Sprague, A. L.: 2000, 'Thermal emission spectroscopy and data analysis of solar system regoliths', in Sitko, M. L., Sprague, A. L., and Lynch, D. K. (eds.), *Thermal Emission Spectroscopy and Analysis of Dust, Disks and Regoliths*; Lunar and Planetary Institute, Houston, 167–186 pp.

Sromovsky, L. A., Revercomb, H. E., Krauss, R. J., and Suomi, V. E.: 1983, *J. Geophys. Res.* **88**, 8650–8666.
Strobel, D.: 1982, *Planet. Space Sci.* **30**, 839–848.
Tholen, D. J. and Zellner, B.: 1983, *Icarus* **53**, 341–347.
Thomas, P. C., Black, G. J., and Nicholson, P. D.: 1995, *Icarus* **117**, 128–148.
Thompson, W. R., Todd, H., Schwartz, J., Khare, B. N., and Sagan, C.: 1991, *Icarus* **90**, 57–73.
Tokunaga, A. T.: 1980, *Bull. Amer. Astron. Soc.* **12**, 669.
Tokunaga, A.T., Caldwell, J., and Nolt, I. G.: 1980, *Nature* **287**, 212–214.
Tomasko, M. G., West, R. A., Orton, G. S., and Tieffel, V. G.: 1984, Clouds and aerosols in Saturn's atmosphere, in *Saturn* (T. Gehrels and M. S. Matthews, Eds.) pp. 150–194. Univ. of Arizona Press, Tucson.
Tomasko, M. G., *et al.*: 2002, *Space Sci. Rev.* **104**, 469–551.
Toon, O. B., McKay, C., Courtin, R., and Ackerman, T.: 1988, *Icarus* **75**, 255–284.
Tyler, G. L., Eshleman, V. R., Anderson, J. D., Levy, G. S., Lindal, G. F., Wood, G. E., *et al.*: 1981, *Science* **212**, 201–206.
Van Allen, J. A.: 1983, *J. Geophys. Res.* **88**, 6911–6918.
de Vanssay, E., Gazeau, M. C., Guillemin, J. C., and Raulin, F.: 1995, *Planet. Space Sci*. **43**, 25–31.
Warren, S. G.: 1984, *App. Opt.* **23**, 1206–1225.
Weisstein, E. W. and Serabyn, E.: 1996, *Icarus* **123**, 23–36.
West, R. A., Strobel, D. F., and Tomasko, M. G.: 1986, *Icarus* **65**, 161–217.
Whitcomb, S. E., Hildebrand, R. H., and Keene, J.: 1980, *Science* **210**, 788–789.
Wilson, P. D. and Sagan, C.: 1995, *J. Geophys. Res.* **100**, 7,531–7,537.
Wilson, P. D. and Sagan, C.: 1996, *Icarus* **122**, 92–106.
Wolf, A. A.: 2002, *Space Sci. Rev.* **104**, 101–128.
Wong, A.-S., Morgan, C. G., Yang, Y. L., and Owen, T.: 2002, *Icarus* **155**, 382–397.
Wong, M. H., Bjoraker, G. L., Smith, M. D., Flasar, F. M., and Nixon, C. A.: 2004, *Planet. Space Sci.* **52**, 385–395.
Yanamandra-Fisher, P. A., Orton, G. S., Fisher, B. M., and Sánchez-Lavega, A.: 2001, *Icarus* **150**, 189–193.
Yelle, R. V.: 1991. *Astrophys. J.* **383**, 380–400.
Yelle, R. V. and McGrath, M. A.: 1996, *Icarus* **119**, 90–111.
Yoder, C. F., Synnott, S. P., and Salo, H.: 1989. *Astron. J.* **98**, 1875–1889.
von Zahn, U. and Hunten, D.: 1996, *Science* **272**, 849–851.